UNIVERSITÀ DEGLI STUDI DI PADOVA

DIPARTIMENTO DI INGEGNERIA INDUSTRIALE

DEPARTMENT OF INDUSTRIAL ENGINEERING

MASTER DEGREE IN AEROSPACE ENGINEERING

Experimental investigation of the fluid dynamic behavior over a sphere and an icosahedron under extremely low Reynolds number conditions

Supervisor
Prof. Francesco Picano

Student
Davide Visentin 2027437

Co-Supervisor
Prof. Raúl Manzanares Bercial
Prof. Ángel Rodríguez Sevillano

ANNO ACCADEMICO 2023-2024

Data di laurea 19/04/2024

''Neque existimes quod tibi difficile visum est,

homini inpossibile esse;

sed existima posse et te

quod homini possibile est''

Marco Aurelio

Abstract:

In recent investigations a new kind of instability has been discovered. This instability takes place on spherical beacons placed on the guard cables of the electrical power lines, consisting in instability intermittency states on the aerodynamic lateral force. The before mentioned investigation showed that both the sphere with and without cable exhibit intermittency states. Its behavior is determined by the asymmetry on the boundary layer separation line on the body and is completely random since the sphere is a revolution body with no favored direction. The aim of this work is to investigate the fluid dynamics of a sphere and an icosahedron at low Reynolds numbers using a water tunnel, to establish a comparison between the wake vortexes of a revolution bluff body and a bluff body with sharp edges. Specifically, photos were taken to observe the flow evolution using ink. This technique was employed to assess the system instability, and to measure the dimension and shape of the wake behind this bluff body. The initial part of the work focused on designing and 3D printing the two geometries. Once completed, the test campaign commenced in the water tunnel, examining the effect of varying the Reynolds numbers. The results obtained from these experiments contribute to understanding flow dynamics in the presence of different geometries and comparing curve bodies with sharp edges bodies behavior. Some conclusions and future jobs will be defined.

Contents

List of Figures

Chapter 1

Introduction

1.1 Motivation

A sphere is a three-dimensional geometric object, all the points in space are equidistant from a fixed point known as the center. While theoretically straightforward, crafting a perfect sphere presents significant challenges. Despite this, spheres find extensive application in engineering and natural phenomena. For instance, they serve as markers for high-voltage power lines.

In recent years it has been studied aeroelastic instability, named Transversal Instabilities due to Longitudinal Winds (TILoW), in high-voltage overhead power lines equipped with spherical warning beacons. This phenomenon involves the oscillatory behavior of the beacons when subjected to longitudinally flowing wind, confined to a plane perpendicular to both the wind vector and the cable axis. Such oscillations pose risks to the structural integrity of the supporting system, potentially leading to fatigue-induced structural damage and subsequent failures within the electrical power distribution network.

Raul Manzanares 2023 [1] conducted wind tunnel tests on isolated spheres, revealing intermittent lateral forces associated with Transversal Instabilities due to Longitudinal Winds on overhead power lines. These forces, which vary with Reynolds number, exhibit chaotic behavior without consistent periodicity, affecting boundary layer separation and force direction. High-resolution pressure data helps identify these intermittencies, crucial for understanding and mitigating aerodynamic risks associated with spheres.

Initial investigations by Gómez-Ortega (2019) [2] employed an elastic mathematical model to describe various oscillation modes of a complete catenary system based on the number of beacons, which accurately matched field observations. Furthermore, Ogueta-Gutiérrez (2019) [2]

developed a mathematical model specifically for individual beacons, applying Newton's equations to the sphere. This model considered sideslip angle induced by oscillations and static cable angle, resulting in an instability criterion relating aerodynamic forces to cable angle. Subsequent dynamic testing of a single sphere in a swing configuration, detailed by Gómez-Ortega (2019)[2], furthered the investigation. Recent research by Gómez-Ortega (2021) [3] has elucidated the intermittent lateral force component in unsteady aerodynamic forces acting on spheres, both with and without a cable, through meticulous measurements with high time resolution. This study marks a departure from previous investigations, which primarily focused on broader unsteadiness phenomena without delving into the specifics of intermittency.

Another method employed in studying unsteady aerodynamic forces acting on spheres involved analyzing wake properties. Achenbach (1974) [4] conducted visualizations and hot-wire measurements, confirming periodic fluctuations in the wake of the sphere. Additionally, Taneda (1978) [5] observed through visualizations that the wake of the sphere exhibits random rotation about the streamwise axis. Researchers have utilized wake analysis techniques to investigate unsteady aerodynamics on spheres, revealing periodic fluctuations and random rotational behavior in the wake. The behavior of the sphere is determined by the asymmetry on the boundary layer separation line on the body and is entirely random, as the sphere is a rotational body with no favored direction.

The study in a water tunnel provides an opportunity to visualize the aerodynamic behavior over a sphere, enhancing our understanding of this phenomenon by observing wake shape and vortex behavior.

1.2 Objective

This project is the result of collaboration between the Universidad Politécnica de Madrid ETSIAE and the University of Padova through the Erasmus program. The supervisor of this work in Madrid are Ángel Rodríguez Sevillano and Raúl Manzanares Bercial. Raúl, the project supervisor, observed randomly lateral forces acting on a sphere at $Re = 5 \times 10^3$. This observation prompted the idea to study the fluid dynamics visualization of a sphere for a deeper understanding of the phenomenon. The ETSIAE Aerodynamics Laboratory houses a water tunnel for investigating behavior at very low Reynolds numbers, while the Graphic Expression Laboratory offers 3D printing capabilities. The objective of this master's thesis is to design a prototype for integration with the water tunnel and investigate the behavior and instabilities of a sphere and an icosahedron using three different camera views to visualize the 3D vortex. To achieve this, several questions need addressing:

- What is the flow behavior over a sphere at low Re?
- Are there instabilities present in the sphere?
- What is the flow behavior over an icosahedron at low Re?
- Do the edges of each face on the icosahedron induce streamline separation?
- What are the differences between spheres and icosahedron?

The report addresses these questions by first explaining the operation of the water tunnel. Then, it discusses the design of the two prototypes and the challenges related to 3D printing. It covers the integration with the water tunnel, optimization choices for visualization, and issues related to 3D printing. Lastly, it presents the visualization of results from sphere to icosahedron at different Reynolds numbers, types of visualization, and repetitions of tests.

1.3 Revision of the literature

The provided documents serve as the foundation for this master work and include:

- Introduction to 3D Printing: This introduction provides an overview of the utilization of 3D printing technology.
- Operation of the Water Tunnel at the Laboratory of Aerodynamics of the ETSIAE: This document outlines the operational procedures and methodologies used in the water tunnel facility at the Laboratory of Aerodynamics of the ETSIAE.
- Study on Instabilities over a Sphere: This work investigates instabilities observed over a sphere through wind tunnel experiments conducted at various Reynolds numbers.
- General Summary of the Behavior of Flux over a Sphere: This document offers a comprehensive summary of the behavior of flux over a sphere, likely encompassing findings related to fluid dynamics and flow characteristics.

Now, let's refine the citations for the research articles mentioned:

◇ "Rodriguez-Sevillano, Casati-Calzada et al. 2023, Exploring the Effectiveness of Visualization Techniques for NACA Symmetric Airfoils at Extremely Low Reynolds Numbers" [6]. Published in the Fluids journal by the Multidisciplinary Digital Publishing Institute, this research validates findings from ETSIAE's water tunnel channel by comparing them with results derived from applying the PIV technique in a traditional low-speed wind tun-

nel on a NACA profile. Notably, it emphasizes the significance of Reynolds number similarity between tests and real flight conditions, along with detailing the characteristics and prerequisites of the inkjet visualization technique utilized.

◇ “Raul Manzanares-Bercial, Omar Gómez-Ortega, Fernando Meseguer-Garrido, Mikel Ogueta-Gutiérrez, Sebastián Franchini “Unsteady aerodynamic lateral force on a sphere under a uniform incoming flow “ [1]. Their study presents wind tunnel test results on isolated sphere aerodynamics at various Reynolds numbers. Intermittency was observed in the aerodynamic lateral force across critical and supercritical regimes. Two main intermittency states were identified, their durations varying with Reynolds number. The nature of intermittency appears chaotic, lacking periodicity or consistent durations between appearances. High-resolution pressure coefficient distribution plots aided in identifying states and determining non-uniform boundary layer separation, influencing the lateral force direction.

◇ H. Sakamoto, “A Study on Wortex Shedding From Spheres in a Uniform Flow” [7]. This paper presents experimental investigation of vortex shedding from spheres conducted in a uniform flow with Reynolds numbers ranging from 3×10^2 to 4×10^4 . Key findings include the classification of the Strouhal number (St) variation with Reynolds number into four regions, the transition of hairpin-shaped vortices from laminar to turbulent around Re of 800, obscuring the wake structure, and the coexistence of higher and lower frequency modes of St within Re range of 8×10^2 to 1.5×10^4.

◇ “Muammer Ozgoren, Engin Pinar, Besir Sahin, Huseyin Akilli “Comparison of flow structures in the downstream region of a cylinder and sphere “ [8] . Their paper presents experimental investigation comparing flow structures downstream of a circular cylinder and sphere at Reynolds numbers of 5000 and 10,000. Results showed variations in wake size, turbulence quantities, and vorticity distribution based on model geometry and Reynolds numbers. Dominance of small-scale vortices was noted in the sphere’s wake compared to the cylinder. Turbulent kinetic energy distribution differed between the two geometries, with the cylinder exhibiting a single peak near the saddle point, while the sphere showed two peaks along shear layers due to 3-D flow behavior.

1.4 Structure

This master’s thesis is structured into five chapters, each addressing specific aspects of the research:

- Chapter 2: introduces the theory of the water tunnel, detailing its operation, parameters, setup chosen for optimized visualization, precautions taken to enhance measurements, and validation tests conducted.
- Chapter 3: presents the design process, covering requirements definition, solution development, encountered issues with Ultimaker 3D printing and CURA software, and final outcomes.
- Chapter 4: showcases results ranging from spheres at varying Reynolds numbers to the Icosahedral structure. It includes explanations of data acquisition methods, 3D vortex visualization, measurements of vortex dimensions and frequency, calculation of Strouhal numbers, and comparison with existing literature.
- Chapter 5: offers conclusions, a comparison between sphere and Icosahedral findings, and suggestions for future research endeavors.

Chapter 2

Water Tunnel and Aerodynamics Investigation

2.1 Water Tunnel theory

One of the techniques for studying fluid motion is experimentation. Scale models of the objects to be analyzed are created and tested in channels or wind tunnels that meet the appropriate conditions for conducting the experiment. While in other fields it is easy to observe the motion of bodies and study their behavior, in the case of fluid mechanics and aerodynamics, the aim is to study the movement of gases and liquids, which presents an additional difficulty.

There are various ways to visualize fluid motion. Material can be added to the fluid flow, such as smoke for gases or ink for liquids. The density of this material must be like that of the fluid, in order to follow the airlines and visualize their movement. Another way to visualize is by adding heat or energy through an electric discharge or in the form of heat, causing the particles to illuminate and visualize their flow. Also optical methods, that use the refractive index of light, can also be used to study changes in fluid density.

In this work, aerodynamic prototype moving in a hydrodynamic channel will be studied using ink jet visualization to analyze flow lines. Ink is injected through elongated tubes inside the model and exits through small holes placed on the profile's leading edge.

It is important that the flow is steady, that the ink has the same density as the liquid (in this case water), and that the profile moves uniformly and without unwanted vibrations. Water channel visualization is a truly useful method in aerodynamic analysis, providing a simpler and more cost-effective initial study than a wind tunnel. It gives the opportunity to have a visualization

of the flow and analytics data. At NASA's Dryden Flight Research Center, they use a water tunnel, also known as the Flow Visualization Facility (FVF), to understand the effects of air on aircraft as in figure 2.1.

Water tunnels serve as an alternative to low-speed wind tunnels, though their practicality varies case by case. Generally, employing them for testing real aircraft proves inconvenient due to the discrepancy in Reynolds numbers between tests and reality. Starting from studies on the boundary layer, it is important to consider that the boundary layer on a profile in a water tunnel is usually laminar, while in the flight of real aircraft, it is turbulent. This results in significant differences in the normal velocity profile in one situation and the other, and consequently, in the value of the shear stresses ($\tau = \mu\delta u$) measured on the profile, to which δy, the variation of the dynamic viscosity of the fluid, is added. Faced with this, some researchers have considered adding elements of roughness to the model to artificially create the turbulent boundary layer. However, it has been demonstrated in that this generally leads to the separation of the laminar boundary layer before transitioning to the turbulent regime, demonstrating the inconvenience of water tunnels for this type of study.

Bodies with low aspect ratio and sharp leading edge, like a flat plate, reduce the influence of the Reynolds number, and it has been shown that the measured lift coefficient in the test largely coincides with those deduced from theory for inviscid flows . The study may be interesting for combat aircraft and missiles at certain angles of attack, or other types of profiles. Although the validity of the results obtained for extremely low Reynolds numbers has been demonstrated in, the extrapolation of these results to the flight conditions of a real aircraft is not possible due to the differences in the nature of the flow of a test and the real one, as already discussed. The use of water tunnels in this sense is relegated to verifying anomalies observed in computational tests or for conducting fundamental investigations before initiating research in aerospace applications. The flow over a delta wing figure 2.1 constitutes another exception where the values of pressure coefficients or normal force measured in a water tunnel test share the characteristics of the values obtained in other types of tests, due to the characteristics of the flow over this type of wing, characterized by two vortical streams over it. However, there are usually differences between tests in the position where these vortices appear, although it does not seem to be correlated so much with the Reynolds number as with other parameters of the test, more related to the type of tunnel or model used.

Another type of tests conducted with these tunnels are dynamic tests, which involve the movement of the complete model or parts of it relative to the laboratory or test frame of reference. The advantage of conducting dynamic tests in water is that the pace of movement is much slower than in air, making data acquisition and flow visualization easier. Additionally, the inertia forces

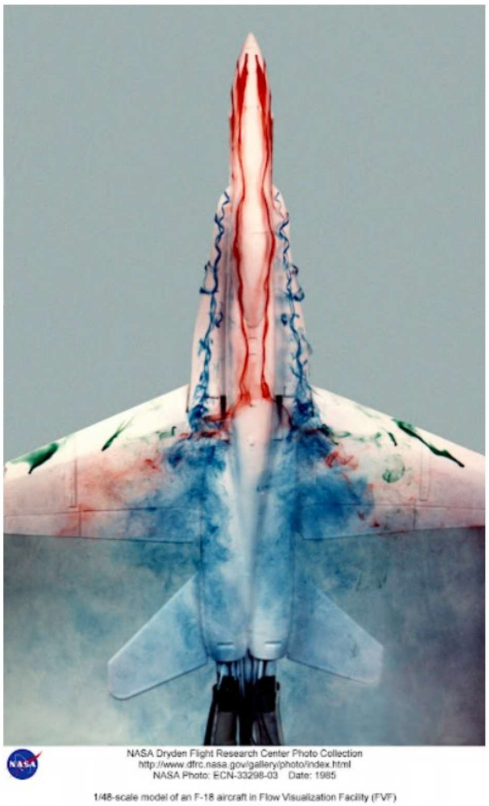

Figure 2.1: F-16 Flow Visualization Facility (FVF).

on the model are lower, facilitating its design and construction, which in turn will have fewer weight constraints compared to a wind tunnel test. Some tests are impossible or very difficult to carry out, such as those requiring recreating compressibility effects. Some special tunnels, such as long towing channels, allow studying the mean and far field of the wingtip vortex wake, which is impossible in other smaller tunnel types due to their size and the influence of wall proximity on wake development and result acquisition. Beyond the study of conventional aircraft, undoubtedly, what has most increased the popularity of water tunnels in recent years are tests conducted on MAVs and their growing popularity within aerospace engineering. The reduced size of the vehicle means that the conditions (Reynolds number) simulated in the test and those in real operation are quite similar, see chapter. For this application, there are few differences between initial research and advanced engineering tests. The only difficulty arises when studying flexible structures, as aerodynamic scalability can be problematic. To this end, there is also a growing interest in the aerodynamic study of aircraft and various types of bodies in the Martian atmosphere. It is demonstrated in that the Reynolds numbers reached, due to the difference in densities of this atmosphere compared to the Earth's, are much lower and, therefore, reproducible in such installations. Another aspect to consider in conducting tests in water tunnels is the fabrication of the model. Common materials used for models in wind tunnels, such as wood

or aluminum, present issues related to water absorption, oxidation, or surface deterioration. This is not a problem if tests do not extend over time (<1 day), and an alternative would be the use of stainless steel, but its tools are expensive and complex. The best alternative is undoubtedly the use of plastic models made through additive manufacturing. The use of 3D printers has spread significantly in the last decade. With this type of printers, finishes with a layer height of up to 0.04 mm can be achieved giving a good smoothness.

2.1.1 Theoretical base

To understand the difference between a water tunnel and a conventional wind tunnel is important to observe the properties of the fluid used in the test. In the next table it is resume the main characteristics of both fluids.

Table 2.1: Properties of water and air at 20°C and standard atmospheric pressure, 101325 Pa.

	Water	Air	Unit	Water/Air
Density	998.2	1.204	kg/m^3	829.1
Dynamic Viscosity	$1.002\ 10^{-3}$	$1.813\ 10^{-5}$	kg/m/s	55.27
Kinematic Viscosity	$1.003\ 10^{-6}$	$1.506\ 10^{-5}$	m^2/s^{-1}	0.066
Speed of sound	1482	343.2 9	m/s	4.318

The density of water is approximately 800 times greater than that of air. Consequently, the turbulent Reynolds stresses, which are directly proportional to density, are also significantly higher in water. This characteristic makes easier to conduct boundary layer studies in water. Additionally, the kinematic viscosity of water is considerably different, being roughly 15 times lower than that of air. This variance presents the opportunity to study phenomena at the same Reynolds number by utilizing smaller prototypes and lower velocities compared to those required in air tunnels.

This capability allows scaling size and velocity while maintaining the same Reynolds number, it does not directly translate to loads and moments. Therefore, there are limitations on the tests that can be performed in water tunnels. It is crucial to exercise caution with the results and carefully consider whether a water tunnel is suitable for the intended investigation.

2.1.2 Condition of similarities

Once the fluid characteristics are established, extrapolating results from tunnel tests to real-world scenarios necessitates criteria for: geometric, kinematic, and dynamic similarity.

- Geometric similarity entails modeling the test object with the same shape as the real-world counterpart.

- Kinematic similarity dictates that fluid velocities at corresponding positions maintain a consistent relationship.
- Dynamic similarity requires that forces at corresponding positions also maintain a constant relationship. Dynamic similarity hinges on certain non-dimensional groups, derived from fluid properties, remaining equal between reality and the test environment, particularly when the forces they represent are pertinent to the study at hand.

It is possible to see the difference between the water tunnel, MAVS, MARS environmental and Aircraft. It is possible obtain a similar Reynolds number using different configurations of parameters. Another important parameter is The Strouhal number, which is relevant for tests where vortices are shed from bluff bodies. In this work it is a parameter used to validate the test, according to the literature.

Table 2.2: Estimated Reynolds numbers.

Environmental	Velocity (m/s)	Charact. length (m)	Dynamic Viscosity (kg/m/s)	Density (kg/m^3)	Reynolds
Water tunnel	$2.7\ 10^{-2}$	0.12	$1.002\ 10^{-3}$	998.2	3200
MAVs	1	0.05	$1.813\ 10^{-5}$	1.204	3300
Mars atmosphere	10	0.20	$9.820\ 10^{-6}$	$1.9\ 10^{-2}$	3800
Real aircraft	235	5.00	$1.300\ 10^{-5}$	0.412	$37\ 10^{6}$

2.2 Water tunnel

In this chapter it is explain the water tunnel, starting from its structure moving through all components, and the chosen setup for flow visualization.

The flow visualization is conducted in the laboratory of Aerodynamics at the Escuela Técnica Superior de Ingeniería Aeronáutica y del Espacio ETSIAE. This laboratory is equipped with a water tunnel and all necessary cameras for conducting measurements.

The water tunnel has been built for students to conduct studies of flow visualization at low Reynolds numbers. The operation is simple: the tunnel is filled with water, and there is a cart that can move along the top of the tunnel at different velocities. On top of the cart, there is a tank filled with ink. The cart has an arm where the prototype can be placed, and with the help of some tubes, it is possible to inject the ink into the flow while the cart is moving.

Description of the figure 2.2:

1. This is the water tunnel, whose lentgh is 3000 mm in length, 720 mm in height, and 420

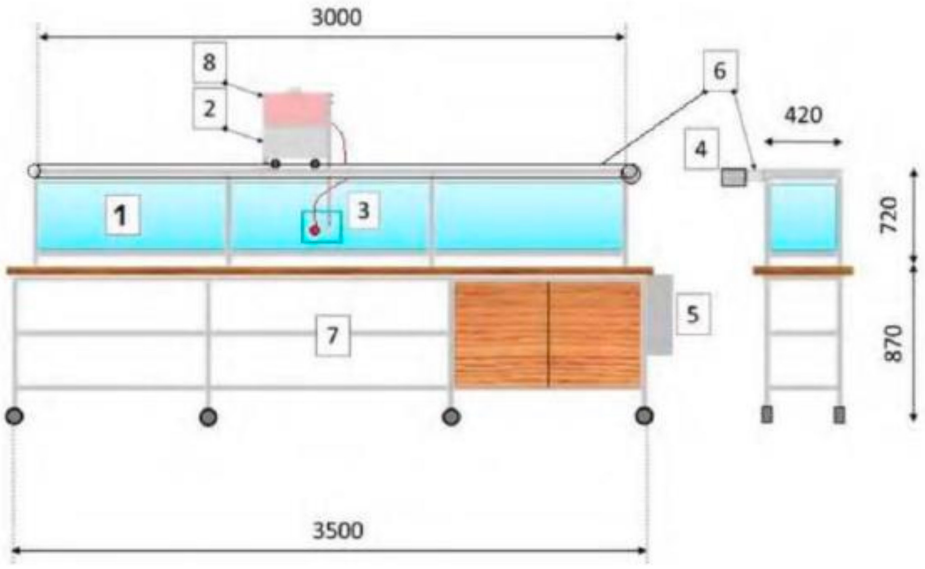

Figure 2.2: Sketch water tunnel.

mm in width.

2. This is the cart that moves along guides.
3. This is the arm where the support can be placed.
4. This is the motor that enables movement of the cart.
5. This is the velocity control.
6. These are the guides where the wheels of the cart move.
7. There are some drawers for storing necessary tools.
8. This is the ink tank.

The cart, figure 2.3, can move because it is connected to the motor with two plastic tapes figure 2.6 that ensure movement. It has four wheels that move along two guides. Each time the cart moves, the tank with all the ink moves as well. There is also the option to attach a camera to the cart to record top view videos.

2.2.1 Motor

The motor 2.5 is an alternating power electric motor that converts rotational movement into horizontal movement using two plastic tapes. To change the velocity, it is necessary to adjust the frequency of the motor. The frequency of the motor is uniform for all movements. There

Figure 2.3: Cart on the top of the tunnel.

Figure 2.4: Cart Cabins.

is a sensor at the end of the tunnel that signals when the end is reached. To return to the initial position, the velocity is kept uniform.

Figure 2.5: Electric motor.

In the velocity controller there is three button one green to go, one red to stop and the last yellow to go back. It is possible to change the velocity using a potentiometer with a wheel used to adjust the motor frequency, ranging from 0 to 155 Hz.

2.2.2 Water Tunnel System for Filling and Draining:

A tube connected to the hydraulic system can fill the water tunnel in 10-15 minutes. It is secured to the water tunnel with plastic fasteners. At the end of the tube, there is a faucet that must be closed to fill the tunnel. The drainage is located at one end of the channel, sloped to facilitate water evacuation. The faucet at the end of the tunnel empties slowly, so a small pump assists in draining. The electric pump is connected to the velocity controller, and it is important not to leave the tunnel during operation to avoid damaging the pump.

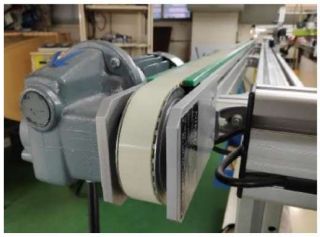

Figure 2.6: Plastic tape.

Table 2.3: Speeds and Reynolds numbers of selected tests.

Motor frequency (Hz)	Cart Velocity (m/s)	Reynolds
50	0.019	2000
75	0.026	3000
155	0.058	6000

2.2.3 Ink Tank System:

The ink tank has a capacity of 10L and must maintain a constant flow rate for accurate results. Therefore, it is designed as a Mariotte flask, open to the atmosphere at the top and sealed with a cork stopper containing three holes. One hole is for filling the tank, another for air evacuation during filling, and the third connects the tank interior to the outside. These holes are closed with throttle valves to prevent leaks. A screw valve modulates the ink flow precisely. A security valve allows opening and closing of the ink flow for repeated tests with the same ink amount.

2.2.4 Branching System for Ink Injection:

After the ink tank, there are tubes and branches for ink injection into the flow 2.13. Each branch can accommodate ten tubes, with the option to use multiple branches simultaneously.

2.2.5 Ink and Clamping System:

The ink, figure 2.14, used is a non-toxic, water-soluble cosmetic red colorant with a similar density to water. It is applied the proportion of one part of water and 0.1 part of ink for better visualization. The ink brand is Gran Velada.

The clamping system consists of three pieces: the arm, tripod, and metal clamping plate. The arm connects the wagon to the tripod, allowing height adjustment. The tripod 2.15 provides three degrees of freedom, enabling adjustments to roll, pitch, and yaw angles for changing the angle of attack. Careful checks are necessary for prototype trim before testing.

The metal clamping 2.16 plate secures the support with two screws and can detach from the

Figure 2.7: Velocity controller.

Figure 2.8: Tube connected to the hydraulic system.

tripod for easier prototype preparation.

2.2.6 Video Setup:

The objective is 3D visualization, achieved through tests to optimize camera configurations. The laboratory utilizes three types of cameras: GoPro, Reflex, and Sony. Each has unique characteristics and positioning.

The waterproof GoPro 2.17 is placed inside the tunnel on the back of the sphere, with a specially designed support for dynamic views.

The Reflex 2.18 captures side views using a tripod and black box, and its position remains fixed.

The Sony camera 2.21 is mounted on top of the prototype 2.20, capturing top views. Imaging software like Quik and Imagine Edge is used for real-time viewing and adjustments.

A parameter table details video recording settings for each camera.

Figure 2.9: Water tap.

Figure 2.10: Pump.

2.3 Sphere literature

2.3.1 Bluff bodies

The sphere is a bluff body. In fluid dynamics, bluff bodies hold strong relevance in terms of theoretical and practical phenomena, primarily due to their non-aerodynamic nature. The study of bluff bodies aids in understanding the complex integration between a solid object and the surrounding fluid. One of the most significant phenomena associated with bluff bodies is flow separation.

It is interesting that when bluff bodies move through a flow, the flow can separate from the body's surface in certain regions, creating recirculation zones and altering fluid dynamics parameters. Therefore, understanding this phenomenon is crucial for improving knowledge. The stability of the system can be influenced by vortex formation and the complex interaction between fluid flow and the body's geometry.

2.3.2 Methodology

In experimental fluid mechanics research, there are two fundamental methodologies for analyzing and understanding fluid flows: flow visualization and hot wire anemometry. Flow vi-

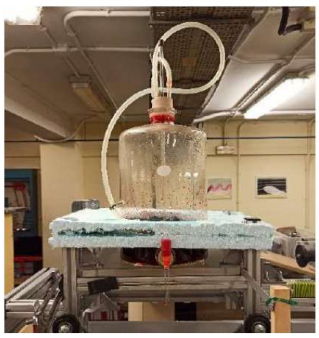

Figure 2.11: Ink Tank.

Figure 2.12: Mariotte flask.

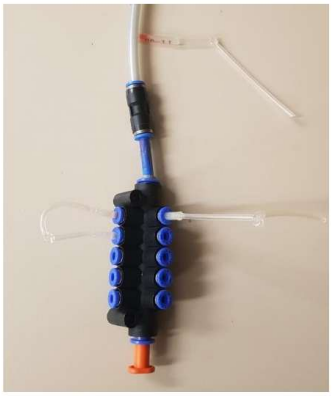

Figure 2.13: Flow distribution fittings and manifolds.

sualization represents a qualitative approach, focusing on visualizing the flow patterns through techniques such as dye injection or particle tracing. This method is particularly interesting in the initial stages of experimental analysis. It allows direct observations of separation zones, vortex formation, and recirculation zones, without the need for computer-based or complex mathematical processing. It provides a real understanding of the phenomena but does not yield quantitative results.

The other method is hot wire anemometry 2.22, representing a quantitative approach. It can

Figure 2.14: Ink

Figure 2.15: Tripod.

directly measure fluid velocity at specific points in the flow field. This method determines the fluid velocity by measuring the temperature change of the wire, which involves the use of a thin heated wire located in the fluid. Hot wire anemometry provides detailed numerical data on the velocity of the flow and turbulent fluctuations within the flow. Overall, however, it does not provide a general overview of all phenomena.

Particle Image Velocimetry (PIV) 2.23 is a technique in fluid dynamics for obtaining velocity maps of fluid flow. The method involves illuminating a plane of interest within the fluid flow with a pulsed laser beam. Particles suspended in the fluid are illuminated and their trajectories are recorded by a high-speed camera. The particles within the fluid can be tracked using various techniques, such as fluorescent suspension particles or seeding particles of known size. The camera captures images of the moving particles at very short time intervals, allowing for the acquisition of velocity field information. After image acquisition, PIV analysis software processes the data to determine the position of particles in each image and calculate their velocities. Using cross-correlation techniques, the software compares the positions of particles in two consecutive images and computes the displacement between them, which is proportional to

Figure 2.16: Tripod support.

Figure 2.17: Support for camera GoPro.

the flow velocity. The ultimate result of PIV is a two-dimensional or three-dimensional map of the flow velocity, providing detailed insights into the structure and characteristics of the fluid flow in a given region.

2.3.3 Sphere results

In the case of a sphere, 3D vortices are present, and the behavior of the flow around a sphere change significantly depending on the Reynolds number. A comprehensive study of flow visualization was conducted by Taneda (1956) [9]. In the provided figure 2.24, a vortex region is consistently observed behind the sphere, but its behavior varies with Reynolds number.

For Reynolds numbers in the range of $130 < Re < 300$, a very long periodic movement is visible after the vortex ring behind the sphere. This phenomenon persists until $Re = 300$. Between $300 < Re < 420$, a regular vortex shedding pattern is observed, with a shorter period compared to the previous range. However, for $420 < Re < 800$, the regularity begins to decrease. The waveform and amplitude become irregular, and the shedding direction starts to intermittently oscillate from left to right. Although regular vortex shedding is still present, its

Figure 2.18: Nikon D7200.

Figure 2.19: Dark room.

periodicity becomes irregular in this range. In the region of $Re > 800$, there is a mixing of vortex tubes. Some are formed by vortex sheets separating from the sphere surface flow, while others are shed in small vortex loops. Some small vortices move downstream, meeting the large-scale vortex and forming a significant vortex region after the sphere's shape. The shape of the large-scale vortex is not yet fully understood, but it moves randomly along an axis parallel to the flow through the center of the sphere. As the Reynolds number exceeds 800, the pulsations of the vortex sheet separated from the sphere's surface led to periodic shedding of the vortex tubes, covering the vortex formation region. After $Re = 800$, the hairpin-shaped vortices begin to transition from laminar to turbulent vortices with alternating fluctuations. This pattern of vortex shedding continues until the upper critical Reynolds number region. For $Re > 4000$, the periodicity of vortex shedding ceases. The orientation of the wake rotates about the streamwise axis, and the wake adopts a configuration of a theta-shaped vortex.

In the range the of $10^3 < Re < 10^4$ the behavior is different. It is possible to see a strong vortex region.

In the work of Muammer Ozgoren 2011 [1] it is possible to see the flow visualization using the PIV at $Re = 5 \times 10^3$.

In the figure 2.27, it is possible to observe most of the characteristics of the flow around a sphere at low Reynolds numbers. Initially, it is evident that the flow separates at $80°$, but it becomes clearer at $90°$. There is a strong vortex region behind the sphere with the presence of vortices of

Figure 2.20: Position camera Sony.

Figure 2.21: Camera Sony.

different sizes. In the region around the sphere they are smaller than further, since they grow a they move through the flow. The laminar boundary layer becomes unstable approximately one diameter downstream from the sphere due to Kelvin-Helmholtz (KH) instability, which arises from significant velocity disparities between the mainstream flow and the wake regions induced by the sphere.

As noted by Jang and Lee (2008) [10], numerous vortex-ring-shaped protrusions emerge along the borders between the wake and free-stream regions, serving as indicators of instability. The vortices generated by the flow separation around the sphere's perimeter tend to move pressure discrepancies between the main flow and wake regions. It is evident that there is a strong symmetry in the visualization of the sphere, as depicted in the figure. For a deep study of the fluid dynamics of the sphere, it is important to analyze the Strouhal number.

Sakamoto (1990) [7] conducted a comprehensive review of all previous works concerning wakes behind a sphere 2.28. Like Moller in 1938 [11], who measured the frequency of vortex shedding using flow visualization in the range of $10^3 < Re < 10^4$, he has demonstrated that there are two different frequencies, one higher and one lower. Additionally, he collected all previous analyses using hot wire and flow visualization. Sakamoto also confirmed the two different frequencies of the Strouhal number.

It has been discovered that in the sphere there are lateral forces, as exposed by Taneda (1978) [12]. A deep study has shown that the nature of this phenomenon is chaotic, with no found

Table 2.4: Camera parameters

Brand	Model	fps	Focal length (mm)	Resolution (Pixel)
Nikon	D7200	60	6.3	Full HD
Sony	DSCQX100	24	1.8	Full HD
GoPro	Hero Session 5	30	3.5	2.7K

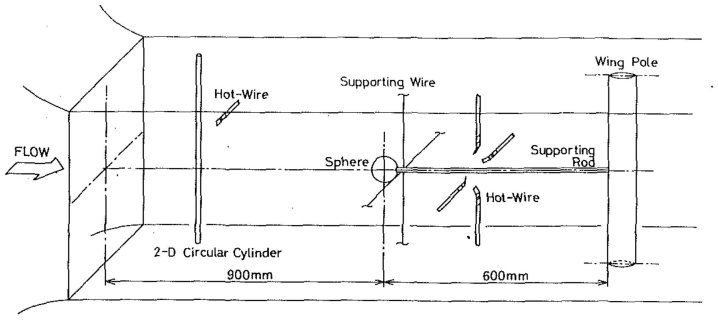

Figure 2.22: Sketch used for Hot wire (H. Sakamoto 1990).

periodicity. The boundary layer separation is irregular and unstable; its shape determines the direction of the lateral force. The subcritical regime is more irregular because there are larger regions of separation and overexpression. In the supercritical regime, this behavior is absent; there are no early separation zones, and all the regions are well defined.

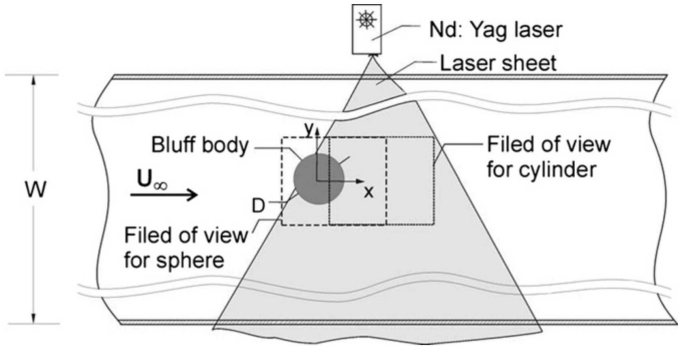

Figure 2.23: Sketch used for PIV (M. Ozgoren 2011).

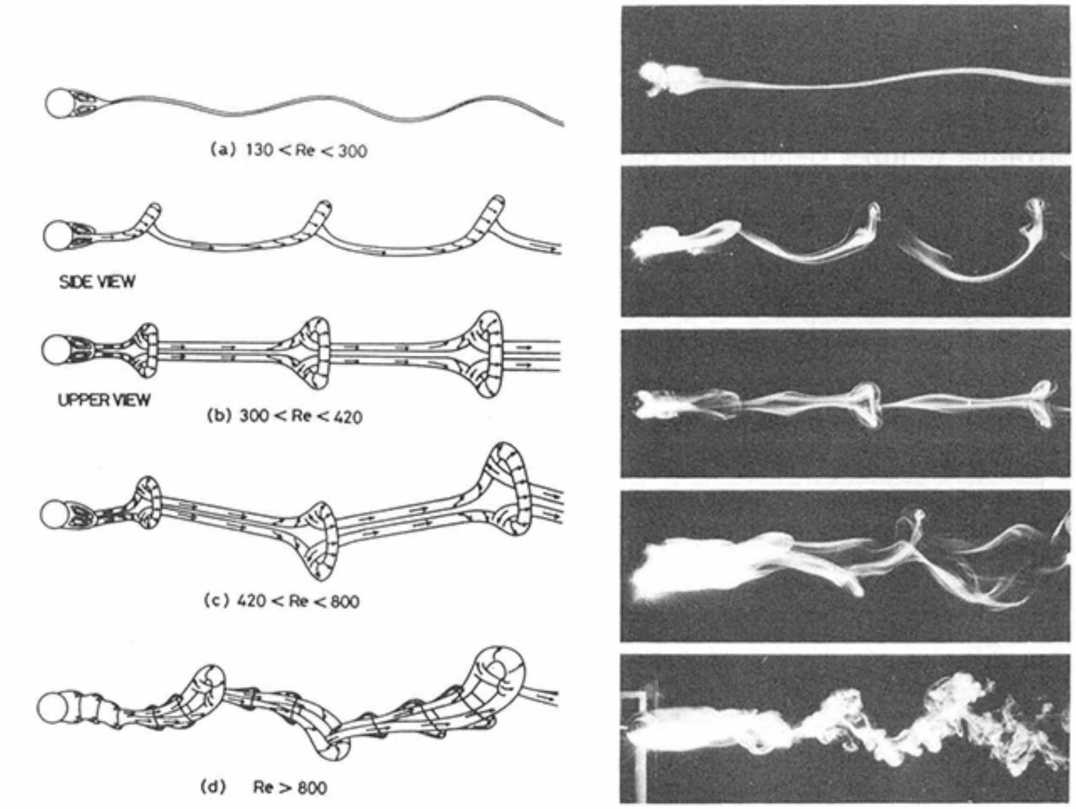

Figure 2.24: Patterns of vortex shedding in wake at each region (H. Sakamoto 1990).

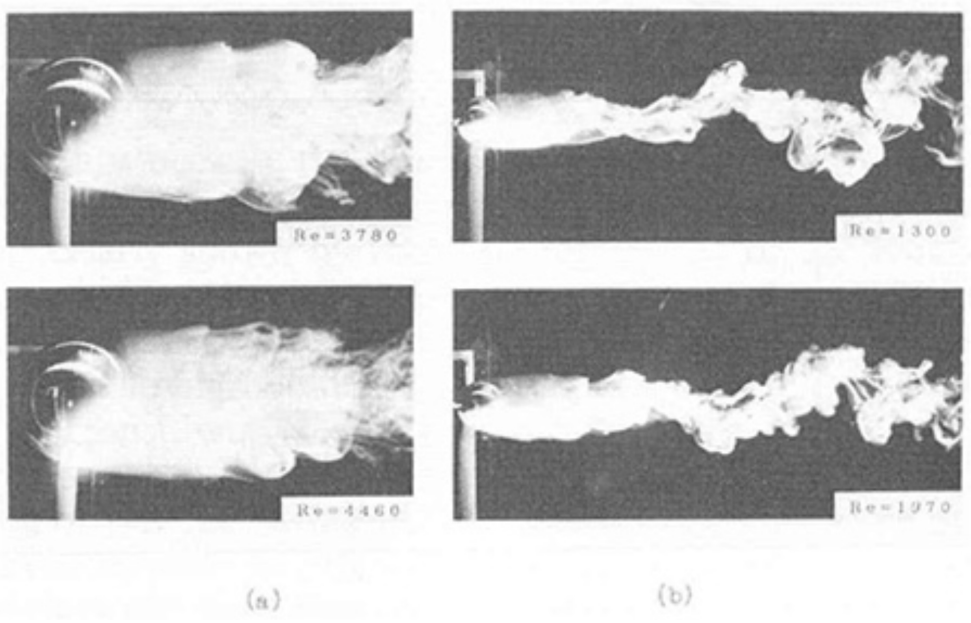

Figure 2.25: Visualized observation for wake behind sphere (H. Sakamoto 1990).

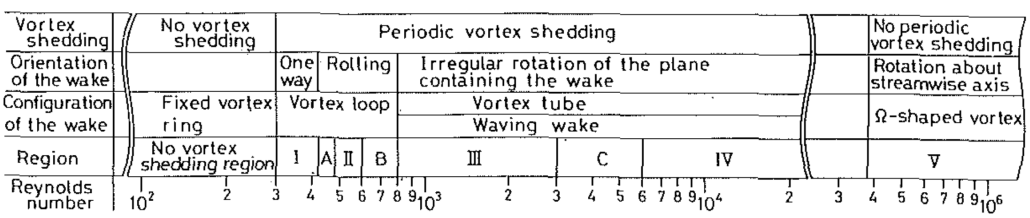

Figure 2.26: Classification of Vortex shedding pattern with respect to change of Reynolds number (H. Sakamoto 1990).

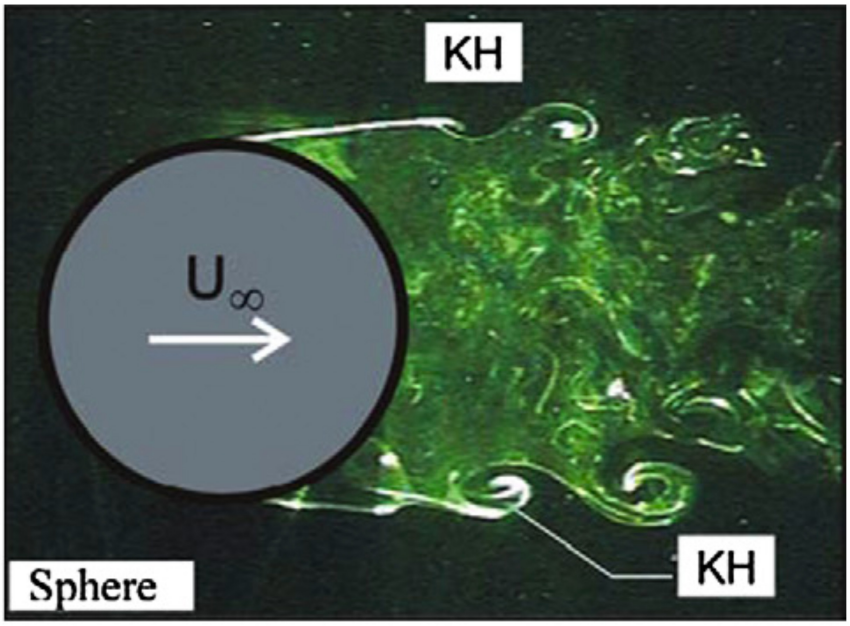

Figure 2.27: Sphere PIV visualization at $Re = 5000$ (M. Ozgoren 2011) .

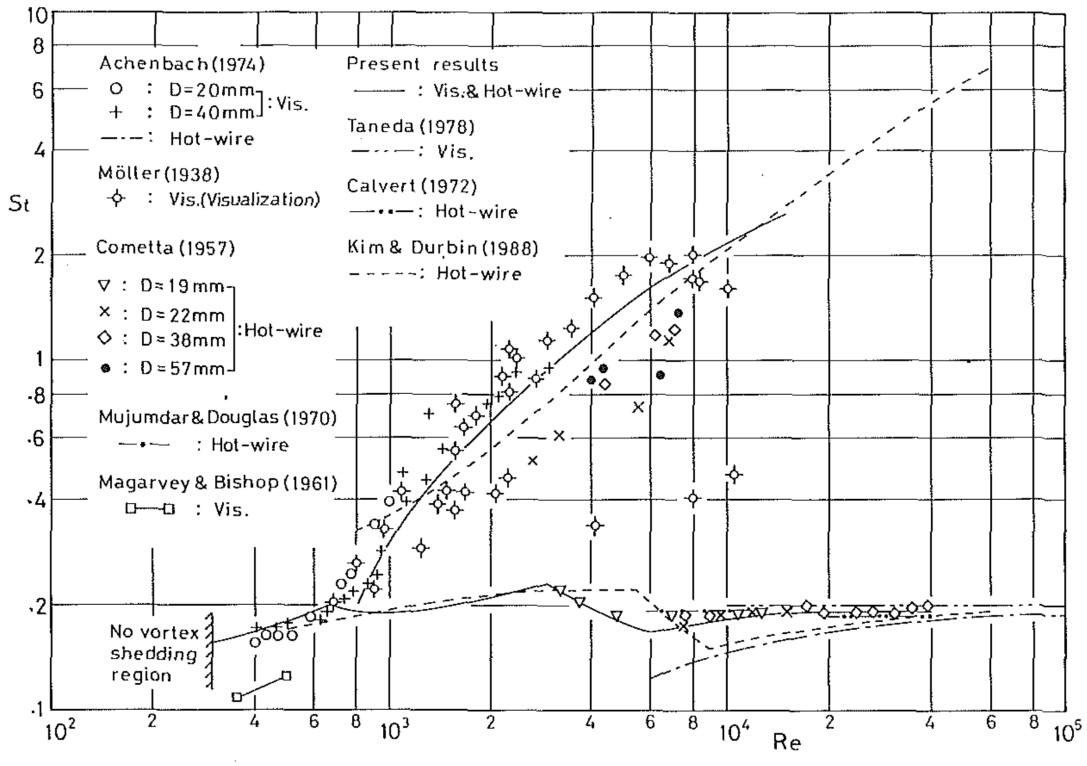

Figure 2.28: Various data for Strouhal number of sphere (Sakamoto 1990).

Chapter 3

Model design

The design it has been made using CATIA, FUSION360 and CURA. The first two are two CAD software, while the other is a slicer to print. The 3D printing that it has been used are Ultimeaker 2+ and Ultimaker 5, the material that has been employee is PLA.

Figure 3.1: CATIA.

Figure 3.2: FUSION 360.

Figure 3.3: CURA.

3.1 Sphere design

It was decided to define requirements in the design to address the problem. The following needs were identified:

Figure 3.4: Ulrimaker 2+.

1. Define a tolerable size for handling the sphere and positioning the tubes, allowing for work-ability.
2. Divide the sphere into two portions to locate the holes inside where the tubes will be glued.
3. Consider a way to connect the two hemispheres to enable prototype modification and positioning in the water tunnel.
   (a) It must be robust.
   (b) It must be simple to connect and disconnect.
4. Determine hole placement, initially considering holes with one at the North Pole and then one in the direction of motion.
5. The sphere should be as smooth as possible.
6. The sphere should be as uniform as possible.
7. Once these requirements were defined, the design process began.

Measurements of the support were taken, to integrate the prototype with the water tunnel arm.

Figure 3.5: Support CAD.

3.1.1 Sphere dimensions

It has been decided to make some preliminary calculation to decide the size of the sphere. It has been calculated the diameter of the sphere in function of the blockage ratio. Following the rules for wind tunnels the blockage ratio should be less thank the 5%.

$$Blockage\ ratio = \frac{Sphere\ cross\ section}{Water\ tunnel\ cross\ section}$$

Table 3.1: Blockage ratio.

Blockage ratio (%)	Diameter (mm)
7.5	100.00
5	81.78
4	73.15
3	63.35

From the beginning it was evident that using an 80mm prototype should be the best option. But it was too small for tests involving multiple tubes. Therefore, it was opted for a 100mm sphere to enhance maneuverability during construction. It was decided to initially print a sphere for conducting various tests and then print a simpler one for conducting only the most interesting tests. This was to minimize all imperfections, because superficial holes could disrupt the boundary layer. It was decided that all joints would have the following characteristics: a 100 mm sphere diameter and a wall thickness of 5mm.

3.1.2 Type of joint

It has been done research on the best joint type. It has been designing four different types of joints and then choose the best one:

1. Simple with magnets.
2. Snap fit first box.
3. Simple with 6 holes.
4. Snap fit circular.

Before starting to consider the type of joint, it was necessary to test the functionality of the 3D printer. Tests were conducted to verify tolerances for fittings and to test the flexibility of the materials. The following tests were carried out:

Hole tolerance test

The cylinders have a diameter of 2 mm and the high is about 10 mm. The holes have the diameter of 2 mm and there is a progression of the offset start into to 0.1 mm increasing 0.1 mm until arriving at 0.6 mm of offset. It has been seen that the tolerance is good for making joint with 0.2 mm but using very small size it makes all the cylinder very fragile. So it has been decided to repeat the test using bigger size of cylinder.

Figure 3.6: Tolerance holes test.

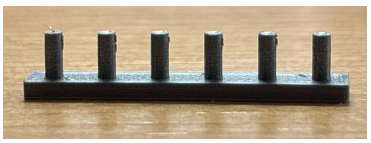

Figure 3.7: Tolerance holes test.

Cylinder-rectangle tolerance test

It has been decided to test different shape to choose the better one. The circular holes have a diameter of 5 mm, if has been applied an offset of 0.2 mm, 0.3 mm and 0.4 mm. The same scheme has been used for the square that has 5 mm of side. It has been seen that for the tolerance of 0.2 mm is good to make Joint. The other options are suggested if there is the possibility to glue the pieces, in my case not because it is mandatory that the sphere can be opened.

Figure 3.8: Cylinder holes test.

Figure 3.9: Square holes test.

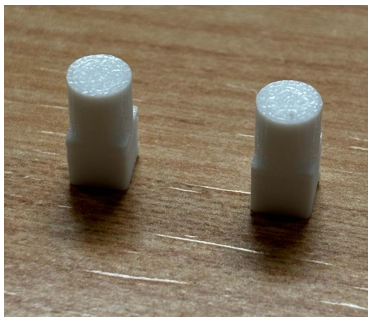

Figure 3.10: Cylinder-rectangle prototype.

From the very first tests, it was evident that the printing direction is a parameter that determines flexibility, as two identical pieces printed in different directions exhibit completely different properties. Also, from the initial approaches, it was apparent that printing the sphere from the larger diameter towards the top is necessary, as it is better to avoid supports touching the external surface, which could damage it. This parameter will then constrain all choices regarding the type of Joint, as with this configuration, we are in the worst-case scenario to ensure flexibility in the Joint. It was immediately clear that designing a semi-mobile joint is not easy because it requires using an appropriate tolerance. A range of 0.2 mm 0.3 mm was identified as the best parameter, but this varies depending on the printing direction and the material used. To use less material, it was decided to only print the connection part between the two spheres. It was decided to use a thickness of 5mm for the sphere, to make it sufficiently solid but not overly flexible.

Simple Joint with magnets

It was decided to design a simple connection between the two hemispheres. In this case, the first problems began to emerge as the sphere, in its ideal simplicity, proved to be a prototype not easy to print. Furthermore, flexibility varies greatly depending on the thickness of the section being printed. Subsequently, when it was observed that a tolerance of 0.2 mm was excellent for a 100 mm diameter sphere with a thickness of 5 mm, it was decided to incorporate eight magnets to make the joint more solid.

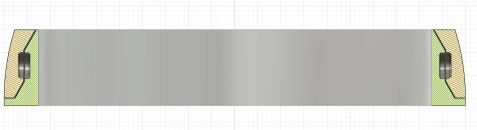

Figure 3.11: Simple magnets Joint CAD section.

Already from the first prototypes, a problem was encountered where one section had a sharp edge. This proved to be a significant issue for the 3D printer as it required support. To circumvent this type of problem, it was decided to no longer use a 90° edge but to soften it with a 60°

ramp. This way, support is no longer needed, and perfect adhesion between the two pieces is achieved.

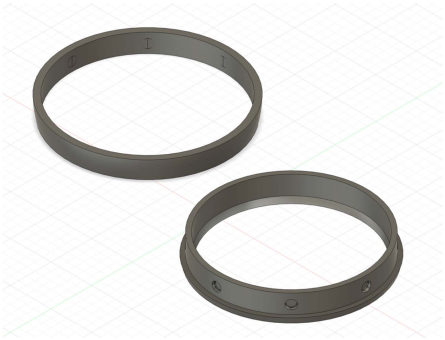

Figure 3.12: Simple magnets Joint CAD.

In the end, this type of joint was not used because in the tests. Many tubes would be employed, and therefore, it was uncertain whether the joint would withstand the weight of the tubes and whether it would remain well-fitted or would have misalignment.

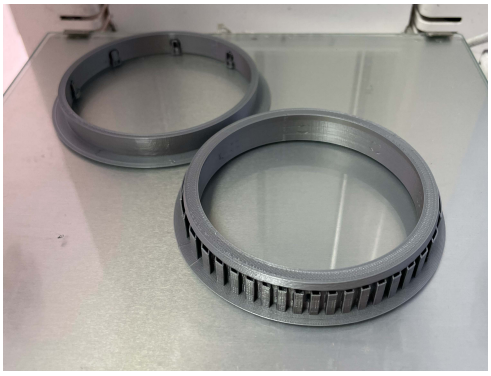

Figure 3.13: Simple magnets joint.

Snap fit joint

The second type of joint was more challenging to create as preliminary tests were required to understand the tolerances of the printer, which vary significantly depending on the material, printing orientation, and printing speed. Another crucial parameter is flexibility, which is why some preliminary tests were conducted. The initial snap fit tests were performed on very small models to determine the optimal angle. From the outset, it was observed that this type of joint is very fragile due to the printing orientation. Many test pieces fit well together, but they broke upon separation. It was decided to relax the system by reducing the contact surface between the two to facilitate extraction after fitting. From there, circular snap fits were attempted to allow for easy use of the sphere. From the initial tests, it was evident that it was not easy to have a snap fit that could endure, as the printing orientation would undoubtedly make the piece fragile.

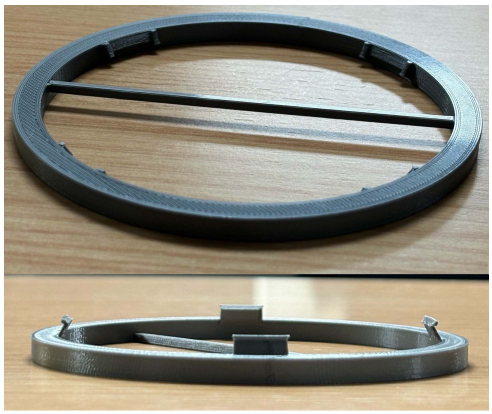

Figure 3.14: Snap fit joint.

The right combination between offset thickness and friction surface was found. However, it still proved to be quite fragile, and robustness of the joint is a key requirement in the design, hence it was discarded for this reason, despite its high practicality. One of the requirements was that the support must be robust, this is not the case.

Six holes joint

An attempt was made to create a simple joint with six holes and six cylinders. The sphere's thickness was set at 5mm, which meant the hole had to be at least 3 mm or less due to obvious printing constraints. This critical parameter significantly influenced all other aspects of the work, making all cylinders extremely fragile. Additionally, it was observed that when the holes were placed in a circle, they all had different tolerances from one another. Subsequently, to facilitate the connection, a slit was created in the middle of the cylinders to ease the attachment and detachment of the joint. Tests were conducted to determine the best compromise between internal thickness and thickness of the semi-cylinders. It has been done a preliminary test with just three cylinder and three holes.

Figure 3.15: Three holes male joint.

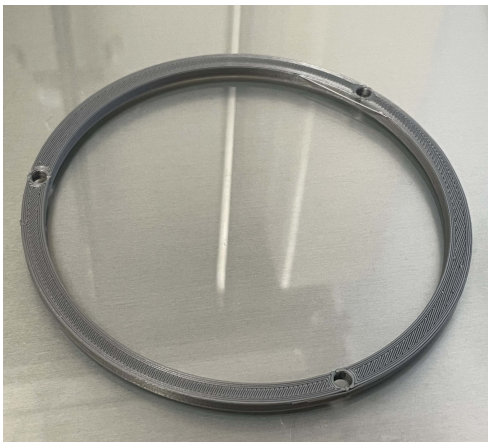

Figure 3.16: Three holes female joint.

However, due to the small size and the binding thickness, this type of connection proved ineffective as there was a high likelihood of breakage, compromising the entire prototype. The teeth broke at the beginning making this type of joint not good for the purpose of this work. Using bigger teeth were not an option because of the size of thickness of the sphere. This type of joins was difficult to extract and replace.

Insert and twist joint

This type of joint is the result of an iterative evolution process. It was decided to start with a very simple connection and then make the joint more solid and effective for the prototype. We began with simple circular snap fits. From the initial stages, it seemed to be an optimal solution, but it allowed rotation of the two hemispheres, which was a failure parameter as it was important for the holes to always be aligned and positioned in the same place. It was noticed that a circular snap fit was difficult to open and close, so it was decided to divide one of the two parts into segments to make the system easier to open and close.

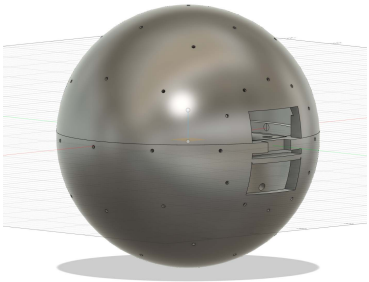

Figure 3.17: Sphere CAD.

After that, the problem of relative movement between the two hemispheres persisted. Therefore,

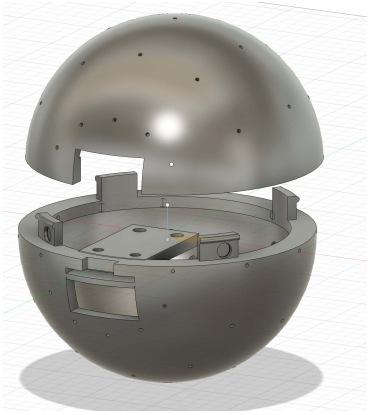

Figure 3.18: Sphere CAD.

it was decided to introduce specific sections where the joint could be stopped and prevent any further relative movement between the two sections. This type of solution proved to be very solid and easy to open and close, hence it was the final choice.

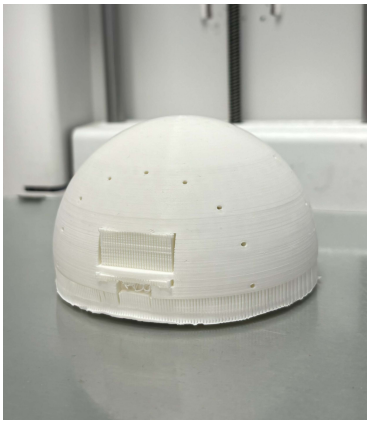

Figure 3.19: Upper part sphere.

3.1.3 Holes position

It is necessary to make holes in the surface of the prototype to have the possibility to inject the ink in the water flux. The holes are made by the 3D printer, their tubes have a diameter of 2.5 mm, so it has been decided to make the holes bigger to have the possibility of glue them. Once the type of connection was finalized, the positioning of the holes from which the ink would be ejected was decided. An initial hole called the 'pole' was defined, and then a series of circular arrays were projected along the sphere. It is necessary to decide the following parameters:

- Pole
- Number of holes per section, angular distance for each hole

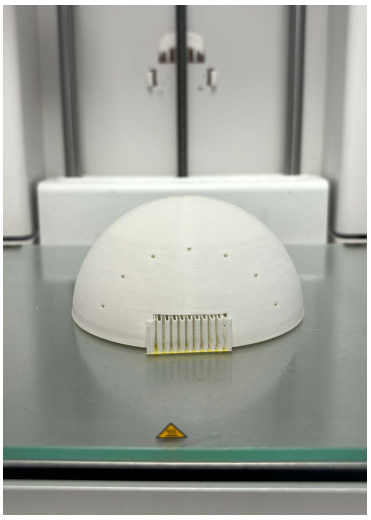

Figure 3.20: Lower part sphere.

- Distance between sections

Pole position

Two poles were decided:

- Pole aligned with -X axis.
- Pole aligned with +Z axis.

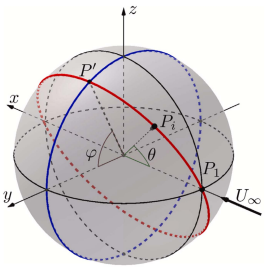

Figure 3.21: Scheme sphere orientation Pole.

For better flow visualization, it was thought to be better to place the holes on the pole parallel to the flow, creating sections to observe the flow evolution. Additionally, this configuration resembled that used in Raul's work [1].

Numbers of holes

It was decided to try sixteen and twelve holes for each section, and it was found that sixteen holes (figure 3.23) was the best solution as it provided excellent flow visualization.

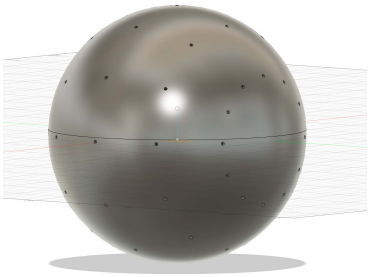

Figure 3.22: Sphere CAD.

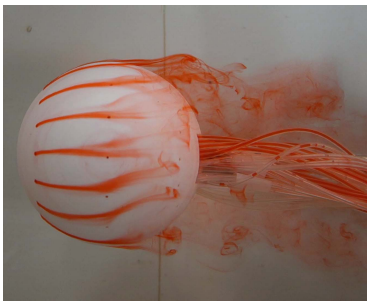

Figure 3.23: Test in the water tunnel using sixteen holes.

Holes Configuration

Another parameter was how many sections to create. Therefore, it was decided to create a sphere rich in holes, conduct preliminary tests, and then use another sphere for only the most important tests. Initially, it was decided to create six sections starting zero to every $30°$.

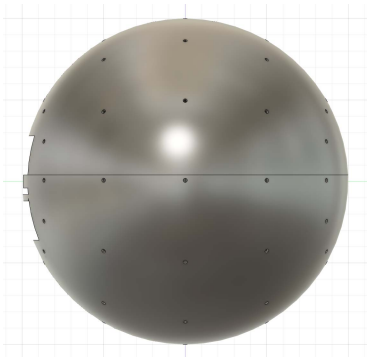

Figure 3.24: Side view of the sphere.

This was because it was known that there were points of interest like 80° where theoretically the flow should start to detach. The other holes were used to determine the best angle. It was observed from the initial tests that the flow followed the line of the holes, which helped us understand where the flow began to separate to confirm our hypotheses. From there, a significant constructive problem arose, as there were about 96 holes, which meant using 96 tubes. From

the outset, it was known that working with so many tubes would be difficult, but it was part of the work's feasibility, as the orientation could be changed if necessary.

It was observed from the outset that the flow followed the trend of the holes, so it was decided to remove the 30°, 60°, 90° and 120° and leave only 45°, 90° and 135° as figure 3.22 to make the sphere as symmetrical as possible. It was noted that the resemblance between the two spheres was very similar, except that the second prototype was much more manageable, and it was noticeable that the flow was less disturbed as there were far fewer tubes.

3.1.4 Sphere smoothness

Another very important parameter is the surface roughness of the sphere. We were interested in making it as smooth as possible to avoid disturbances that could lead to undesirable results. This became a limiting parameter in the design because to make the sphere smoother, it was essential to use very fine layers, which significantly increased the prototype's printing time. This then became a project-limiting parameter because to achieve the smoothest possible sphere, the printing times were around 1.5 days to 2 days. We decided to carry out small tests to optimize the printing process. The parameters that were changed were:

- Printing speed
- Layer thickness

It was experimenting that printing speed did not significantly affect the surface quality of the sphere, whereas the layer thickness had a significant impact. Include photos of the tests.

Another limiting parameter that it has been noticed was the CURA software making the support for the sphere. It generated extensive support that was difficult to remove, also leaving a lot superficial defects. For the first prototypes, it was decided to use that generated by CURA. In figure 3.25,3.26 and 3.27 it is possible to see the surface of the sphere using the support generator. The result was not good enough, it has been decided to design a manual support for the 3D printing.

In the end, it was decided to make manual support to reduce the time. The final result was better than that generated by CURA in terms of surface quality and less processing time, like in the figure 3.20 and 3.19.

Figure 3.25: Holes makes with the support.

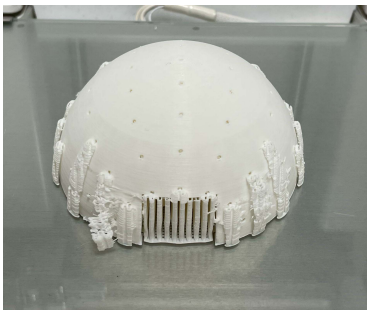

Figure 3.26: Half sphere with CURA's support.

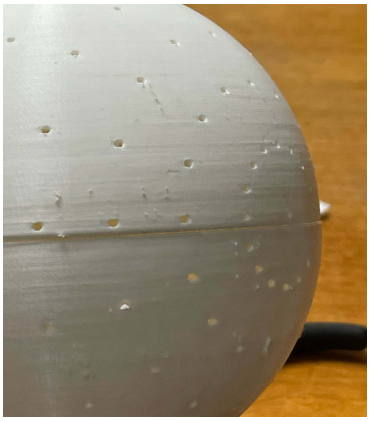

Figure 3.27: Sphere surface with CURA's support.

3.2 Icosahedron design

At the contrary of the sphere the icosahedron it was very simple to design. The size is the same of the sphere, it is actually the size of the icosahedron is of 50 mm. For the design of the joint the simplicity of the geometry allowed to use a simple joint with magnets, as it possible to see in the figure 3.28. It has been decided to put a hole for every face, in the center. So there are twenty holes one for each face.

In this case as well, the geometry has facilitated the possibility of printing uniformly and with

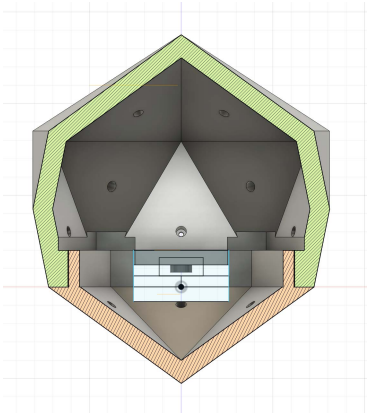

Figure 3.28: Icosahedron section.

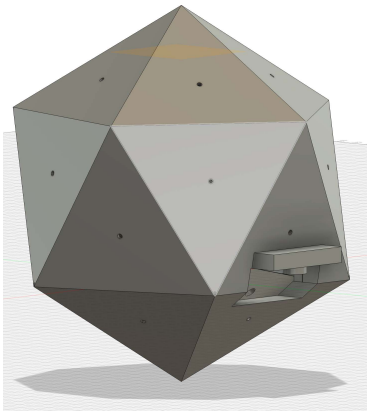

Figure 3.29: Icosahedron CAD.

minimal roughness as it possible to see in figure 3.30 and 3.31. All the icosahedron was printed in less than two days, it has been using the same printing parameters of the sphere.

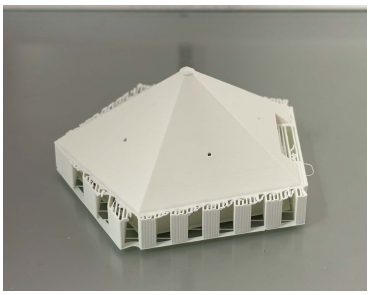

Figure 3.30: Upper part icosahedron.

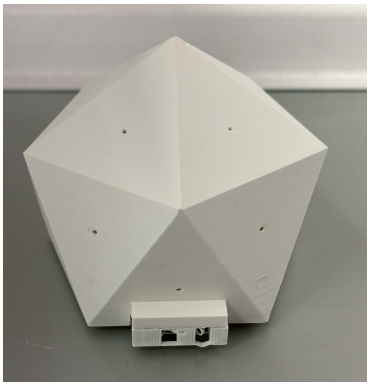

Figure 3.31: Lower part icosahedron.

Chapter 4

Results

4.1 Sphere results

In this chapter there are the flow visualization and the measurement from the video. The first step after the recording of all the videos was to decide what measure and how. Thanks to VCL it is possible to extract the frame from the video, then we will see: the evolution of the wake shape from the three different views: Back view (BV) with the GoPro, Side view (SV) with the Nikon and the top view (TV) with the Sony. Using 'VCL' it has been calculated the frequency of the vortex and so also the Strouhal number. Using the following formula:

$$St = fL/U$$

It has been decided to measure with the software 'ImageJ': the distance between two vortices, the size of the first vortex and the size of the vortex after the shape of the prototype for the Top view and the Side view. ImageJ allows to define a correspondence between the pixel-distance. All the measurements in the graph are adimensional, they are all scaled with the diameter of the sphere.

There will be analyze the behavior of the prototype in the water using the three different sections in the sphere: $\theta = 45°$, $= 90°$ and $= 135°$ and with different Reynolds numbers: $Re = 2000$ and $Re = 6000$. For the case of section at $= 45°$ it has been tested also with just four holes just to have best visualization for the top view and the side view, to exclude the interaction with over vortices.

In each test this will be the scheme:

1. Wave direction and evolution over time (BV, TV and SV): There will be four images for each view that show the flow at the start end at the end.
2. Shape vortex: There will be an image that show the vortex region.
3. Instability: There will be two images to show the instabilities of the streamline.
4. Distance between two vortices (TV and SV): There will be a table and the mean value on the side.
5. Size vortices (TV and SV): There will be a table and the mean value on the side.
6. Vortex frequency: There will be a table and the mean value on the side.
7. Strouhal number: There will be a table and the mean value on the side.

in the figure 4.1 and 4.2 there is an example of the results that has been taken.

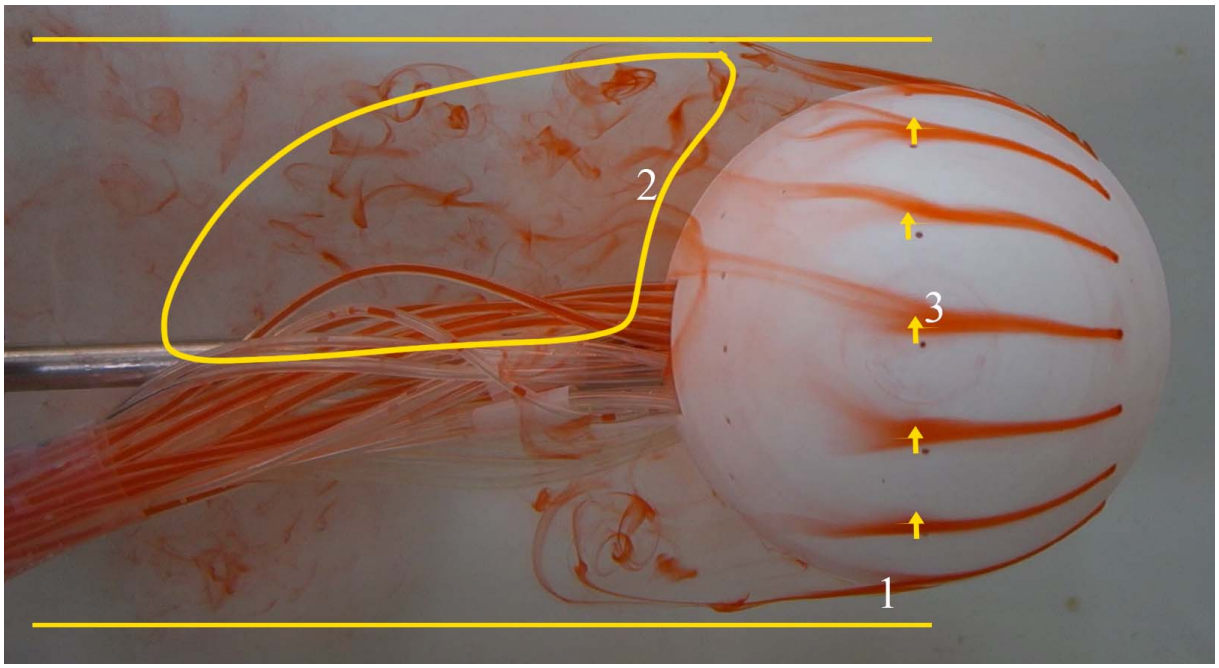

Figure 4.1: 1) Wake evolution, 2) Shape vortex, 3) Instability.

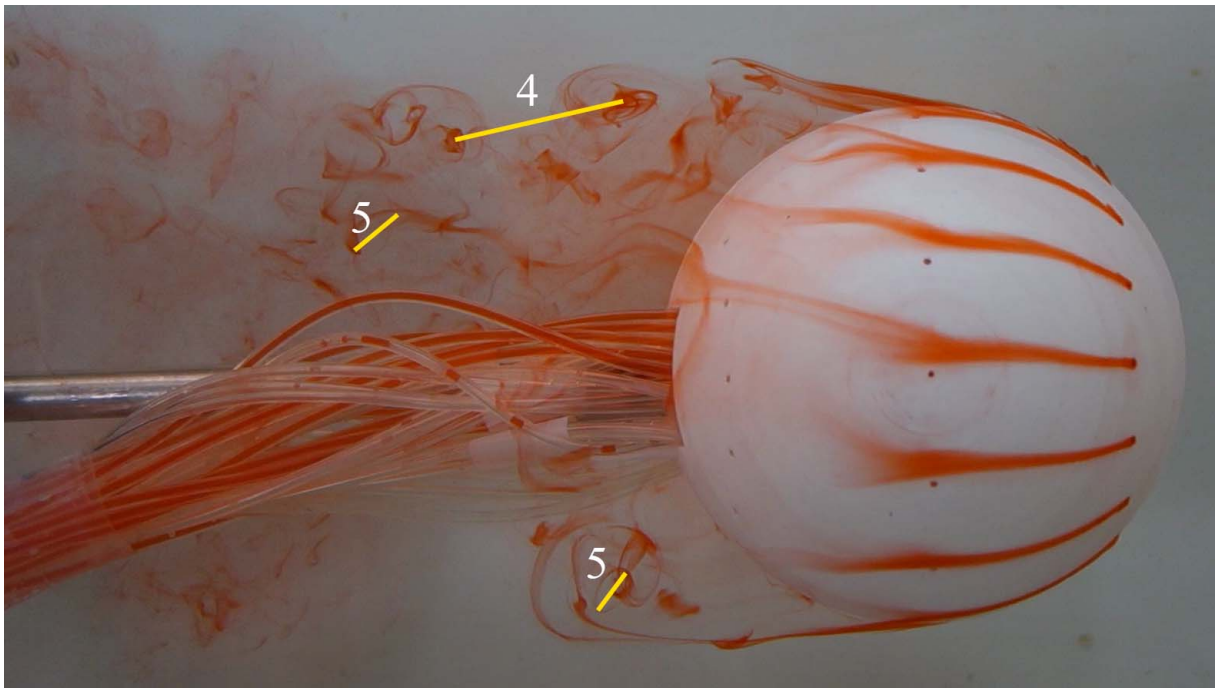

Figure 4.2: 4) Distance between two vortices 5) Size vortices.

It has been tested also the different section of the sphere; the behavior of the vortex shedding is the same. So, repeating the measurement of the distances between two vortex is redundant, meanwhile it is interesting seeing the behavior of the flux in that area without the ink before to have a deep focus in that area.

4.1.1 Sphere test $\theta = 45°$ $Re = 6000$

The aim of this work is the 3D visualization. First there is the top view, it is possible to see a regular vortex shedding and a strong vortex region close to the sphere. There is the clear formation of vortexes. Then there is the side view, it is possible to see that there is a symmetrical behavior with these two view. In both views there is a regular vortex shedding. At the end there is the back view in this case the visualisation of the vortex is not clear but it gives a complete understanding of the phenomena, seeing the movement of the flow. It is possible to see that there is instability of the streamline, also in the side view there is the same behavior. With lower Reynolds number this phenomena increase a lot. At the end of the water tunnel it starts to stabilize. It is possible to see that the creation of the vortex is not uniform. There is different size of vortex, and there is a big difference between the vortex close and far from the sphere, about 50%. Also in this case the frequency is not regular in the dimensions. It has been recognizing that all the vortexes born in the same area, as it possible to see in the figure 4.3b. This has been seen in all the tests. The vortex shedding after the sphere is regular at this Reynolds. The wake

of the sphere is symmetrical and close to the shape of the prototype. The vortex size is always less than the 15% of the sphere, while the distance between of two different is less than the 46% of the diameter of the sphere. The frequency range is about 1 Hz and 2 Hz, and the Strouhal number is in the correct range according to the literature, as it is possible to see in the figure 4.60. It has been repeated three time this test. The general behavior in the other test is almost the same, so will be repetitive to pull all the images. At the end, there will be a section with all the average results that has been measured. The average values of the various measurements taken are collected in table 4.1.

(a) Top view 1.

(b) Top view 2.

Figure 4.3: Sphere wake evolution at $Re = 6000$, Top view.

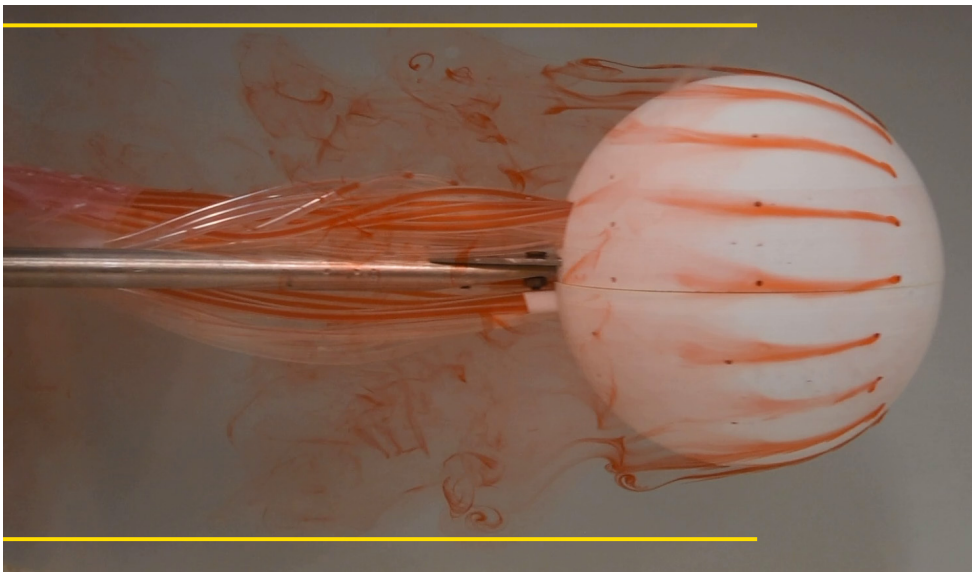

(a) Side view 1.

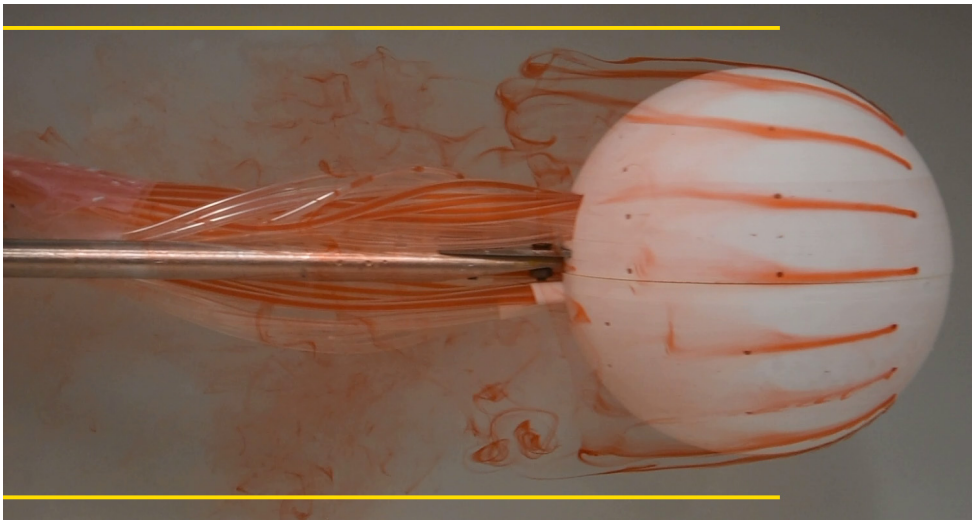

(b) Side view 2.

Figure 4.4: Sphere wake evolution at $Re = 6000$, Side view.

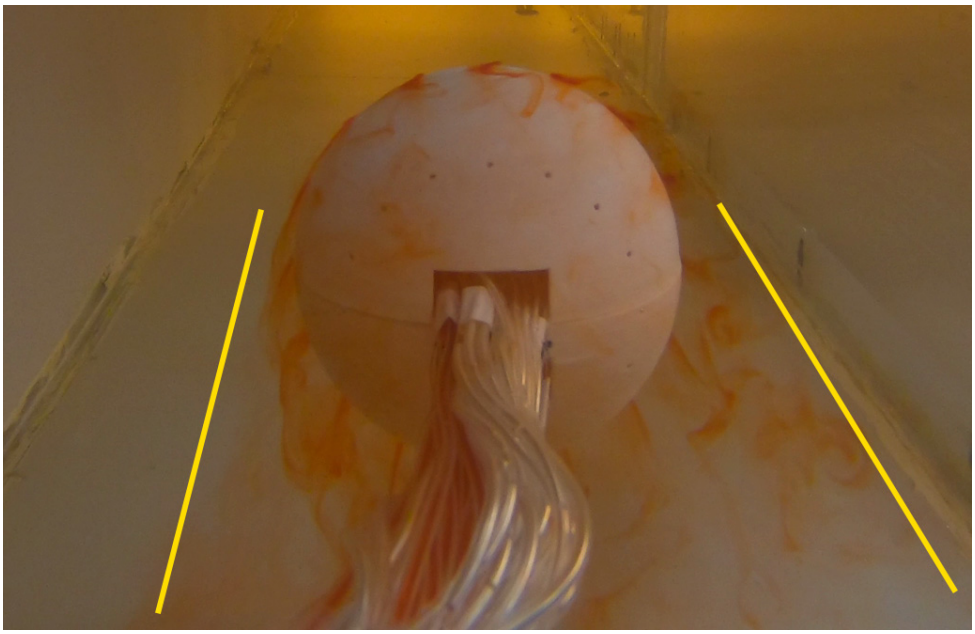

(a) Back view 1.

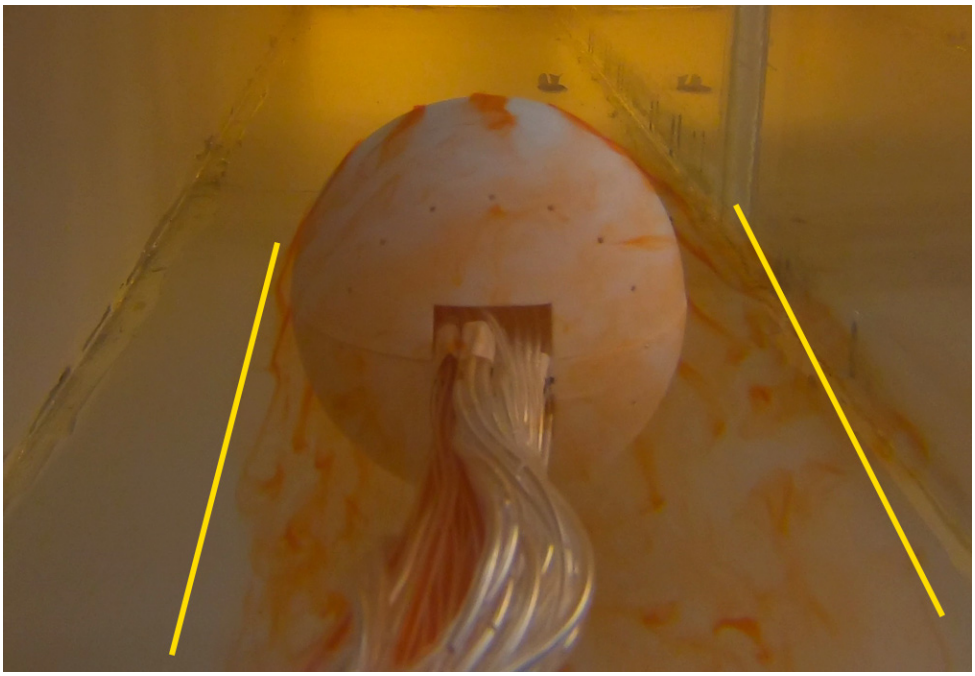

(b) Back view 2.

Figure 4.5: Sphere wake evolution at $Re = 6000$, Back view.

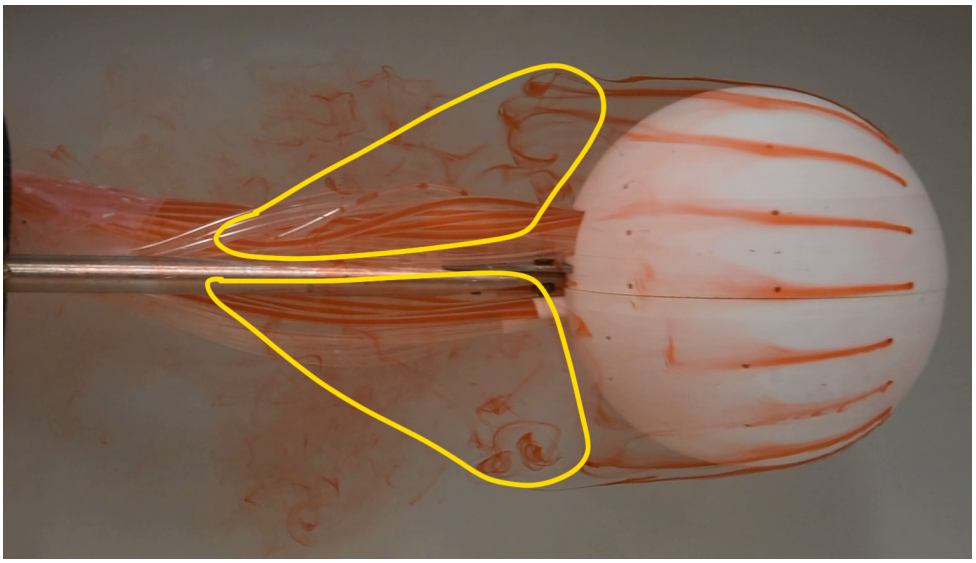

(a) Side View.

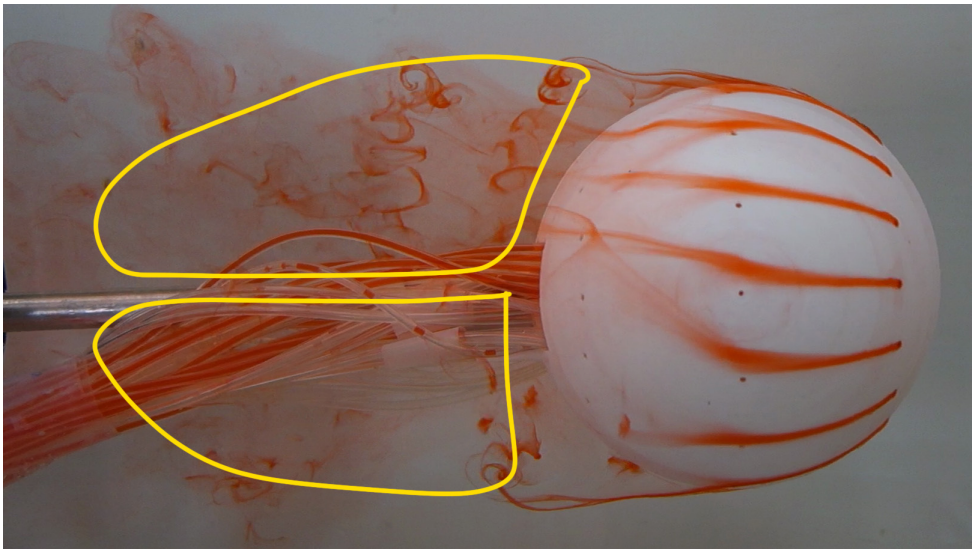

(b) Top view.

Figure 4.6: Sphere wake shape, at $Re = 6000$.

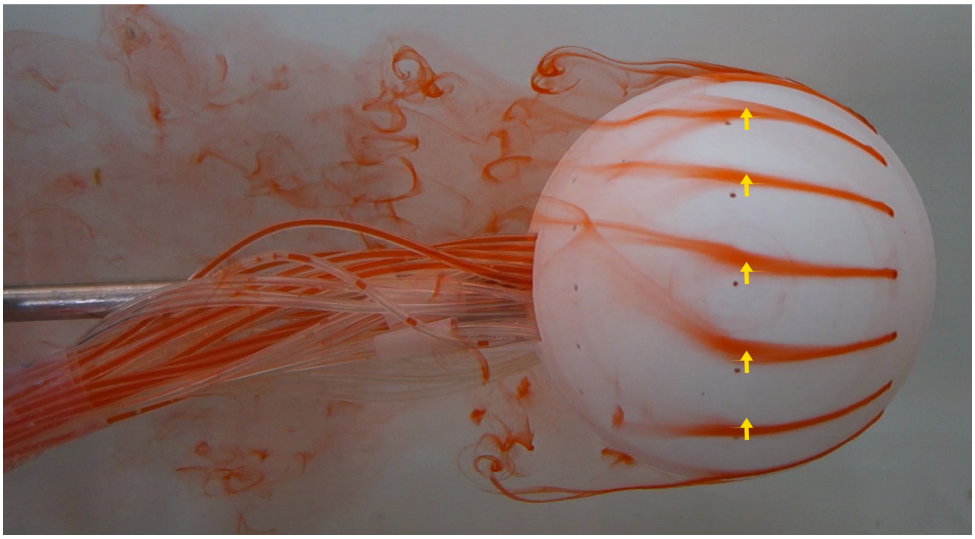

(a) t=22 s ,Top View.

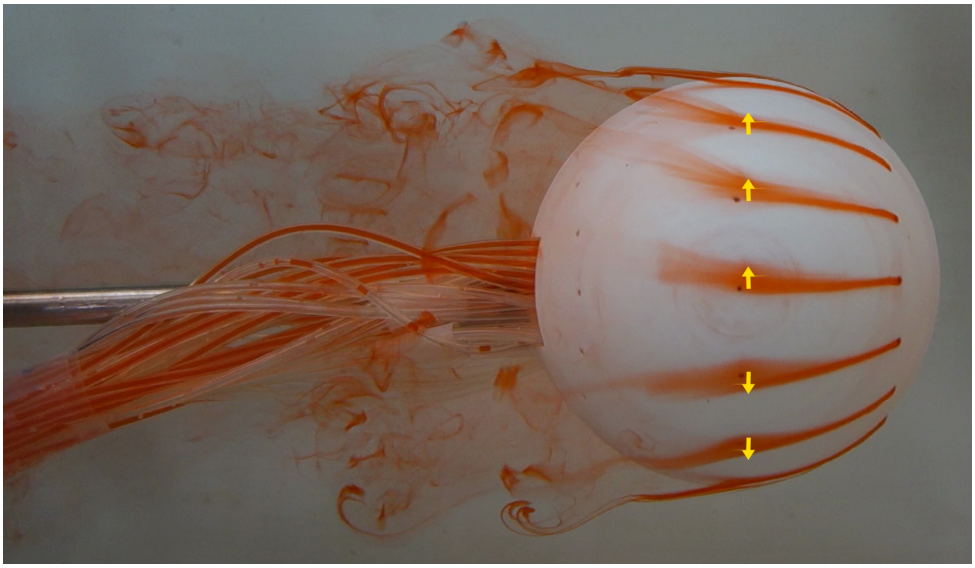

(b) t=31 s ,Top View.

Figure 4.7: Streamlines instability visualization at $Re = 6000$.

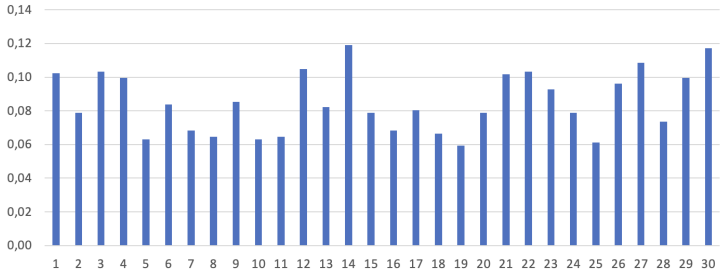

(a) Vortex size for side view.

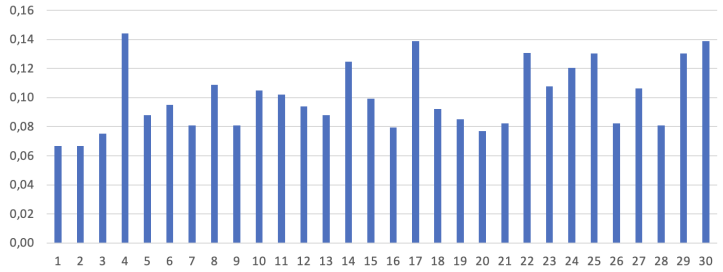

(b) Vortex size for side view.

Figure 4.8: Size of the vortices close to the shape of the sphere, scaled to the diameter of the sphere, at $Re = 6000$.

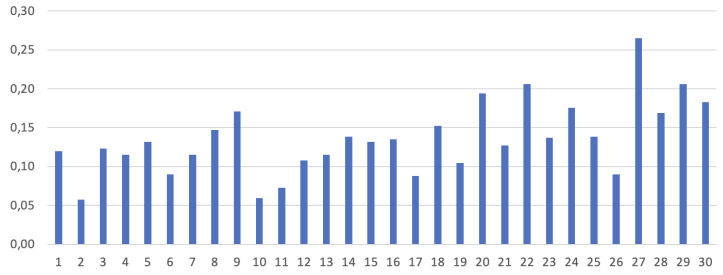

(a) Vortex size for side view.

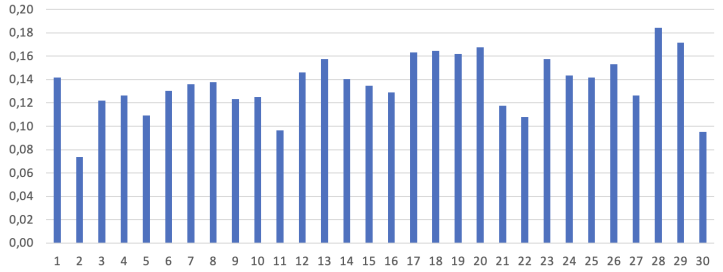

(b) Vortex size for top view.

Figure 4.9: Size of the vortices far to the shape of the sphere, scaled to the diameter of the sphere, at $Re = 6000$.

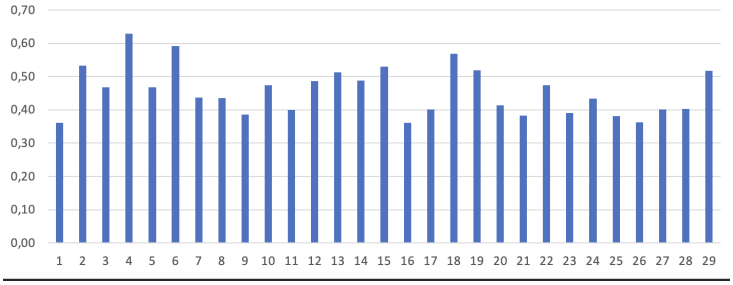

(a) Measurement from side view.

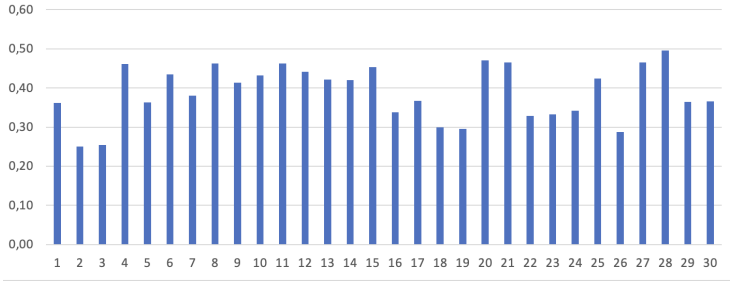

(b) Measurement from top view.

Figure 4.10: Size of the distance between two vortices, scaled to the diameter of the sphere, at $Re = 6000$.

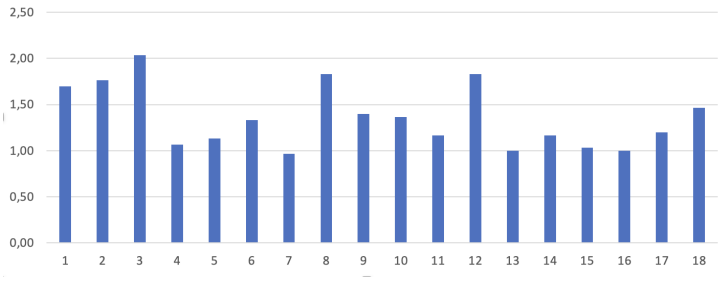

Figure 4.11: Sphere vortex frequency, at $Re = 6000$.

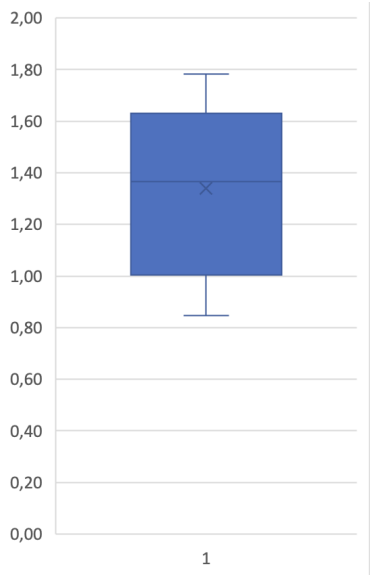

Figure 4.12: Strouhal number of a sphere, at $Re = 6000$.

Measurement	Average value
Vortex size close to the sphere (SV)	0.08
Vortex size close to the sphere (TV)	0.11
Vortex size far to the sphere (SV)	0.14
Vortex size far to the sphere (TV)	0.13
Distance between two vortices (SV)	0.46
Distance between two vortices (TV)	0.39
Frequency	1.3
Strouhal number	1.34

Table 4.1: Average value of the analysis, at $Re = 6000$.

Allen Flow

It has been seen an unpredictable phenomenon during the test with $Re = 6000$, it is called the Allen flow. It is a toroidal vortex that it can be seen at the beginning of the movement of the prototype. It has been observing the formation of a first big toroidal vortex in an unseal area of the sphere (image 4.57a) that makes three four twist and then there is the formation of another vortex in the conform area at about $80°$ degree (image 4.57b), then they mix together (image 4.14a), and they are stating the vortex region (image 4.14b).

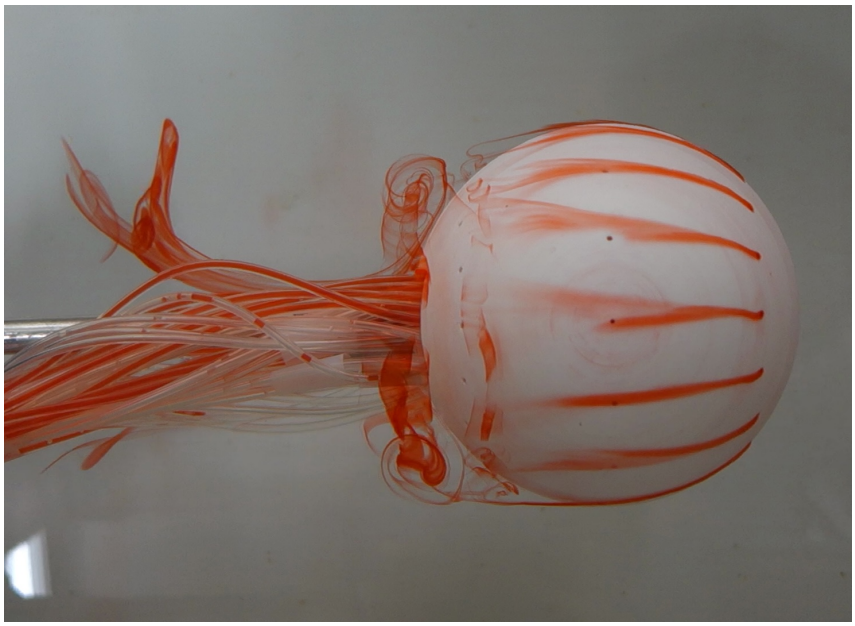

(a) Top view 1.

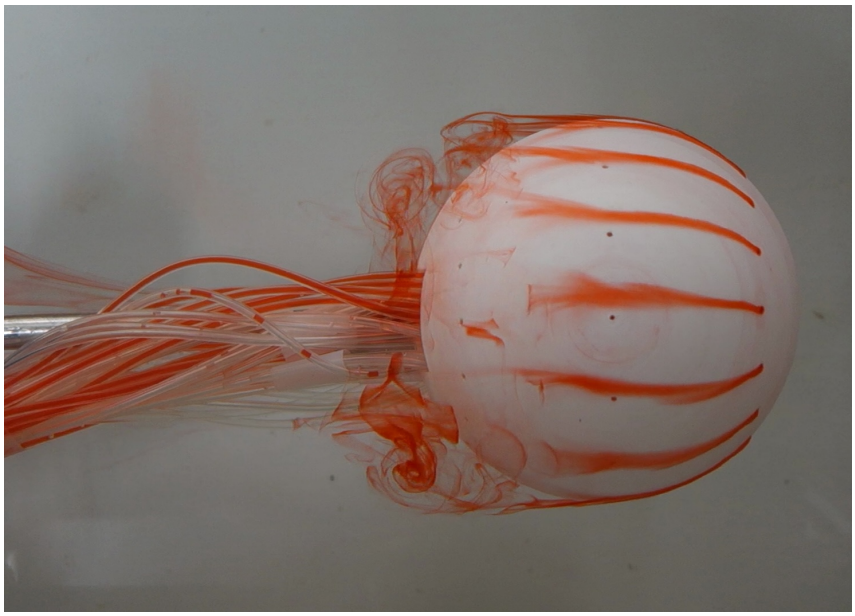

(b) Top view 2.

Figure 4.13: Evolution of Allen vortex, at $Re = 6000$.

(a) Top view 3.

(b) Top view 4.

Figure 4.14: Evolution of Allen vortex, at $Re = 6000$.

4.1.2 Sphere test $Re = 6000$ with four holes visualization

After the general visualization with sixteen holes to have a better view of the vortex there is a visualization with just four holes. The ink from all the sixteen holes is making a lot of vortexes. There are sixteen vortices every time and sometimes they mix tougher, so for having a better knowledge of all the phenomena it has been decided to test with less ink tubes. The behavior is

the same of the previous test, in this case it is possible to see better the vortexes. Using just two holes makes more difficult the calculation of the size because it has been seen less vortex. The general visualization is the same using sixteen ink tubes, but in this case it is possible to see and to measure better the vortexes size and the calculation of the Strouhal number is easier. There is a table with all the average value calculated from the previous graphs. The average values of the various measurements taken are collected in table 4.2 .

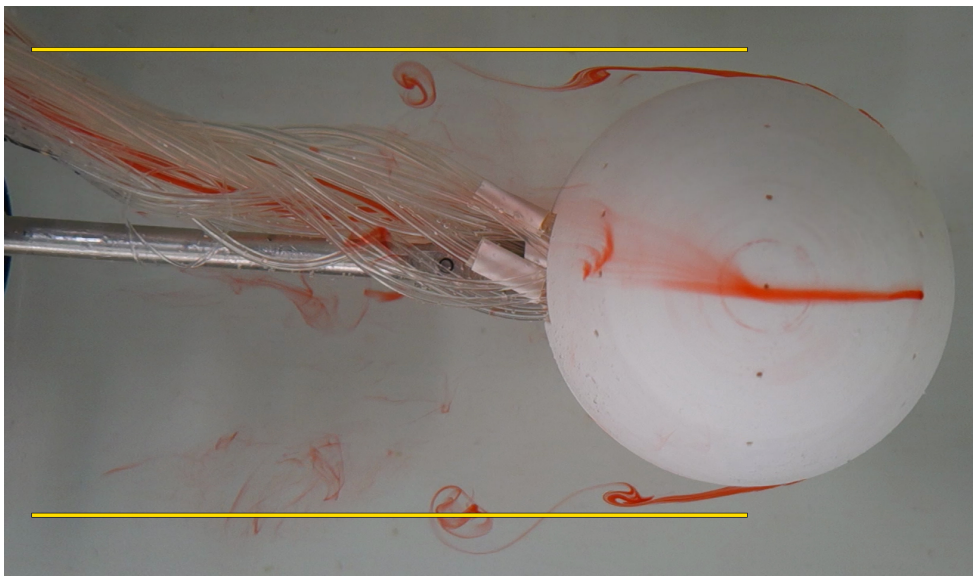

(a) Top view 1.

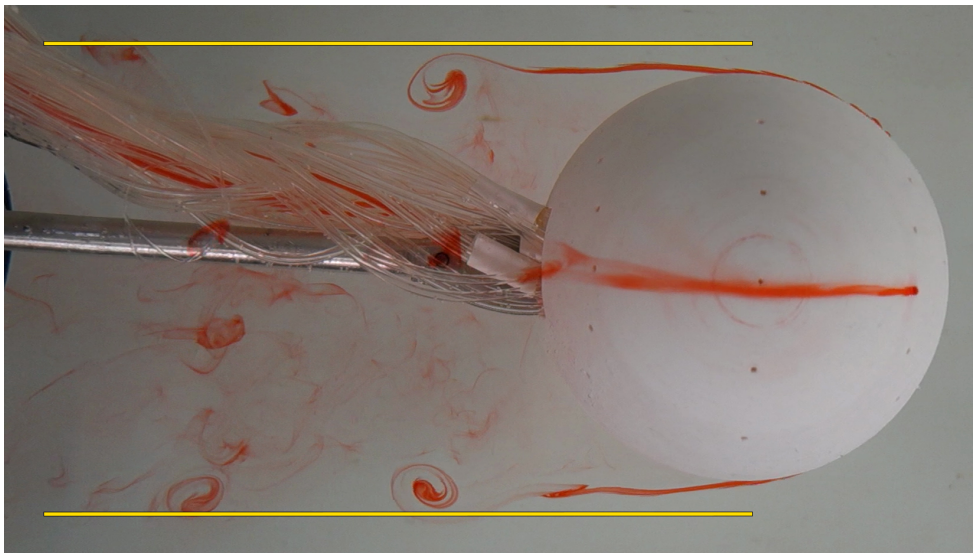

(b) Top view 2.

Figure 4.15: Sphere wake evolution at $Re = 6000$ with four ink tubes, Top view.

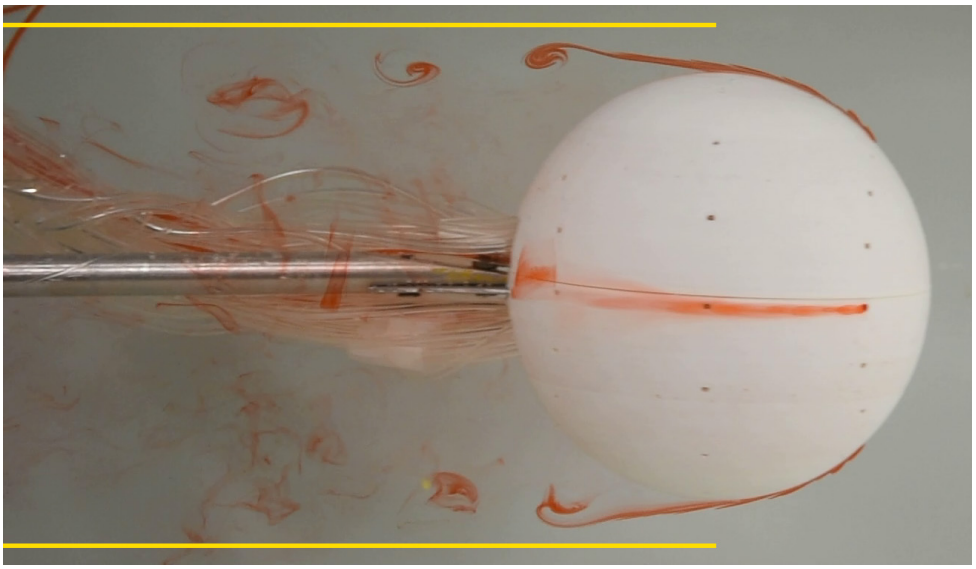

(a) Side view 1.

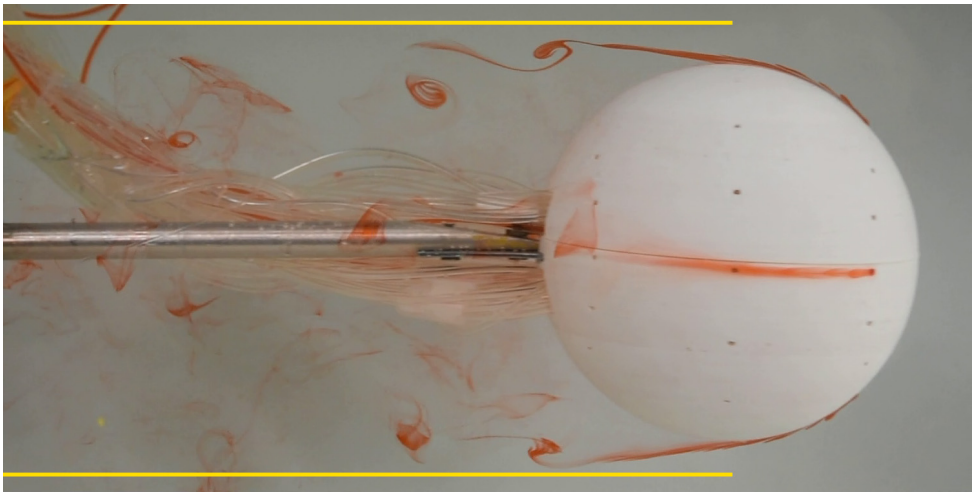

(b) Side view 2.

Figure 4.16: Sphere wake evolution at $Re = 6000$ with four ink tubes, Side view.

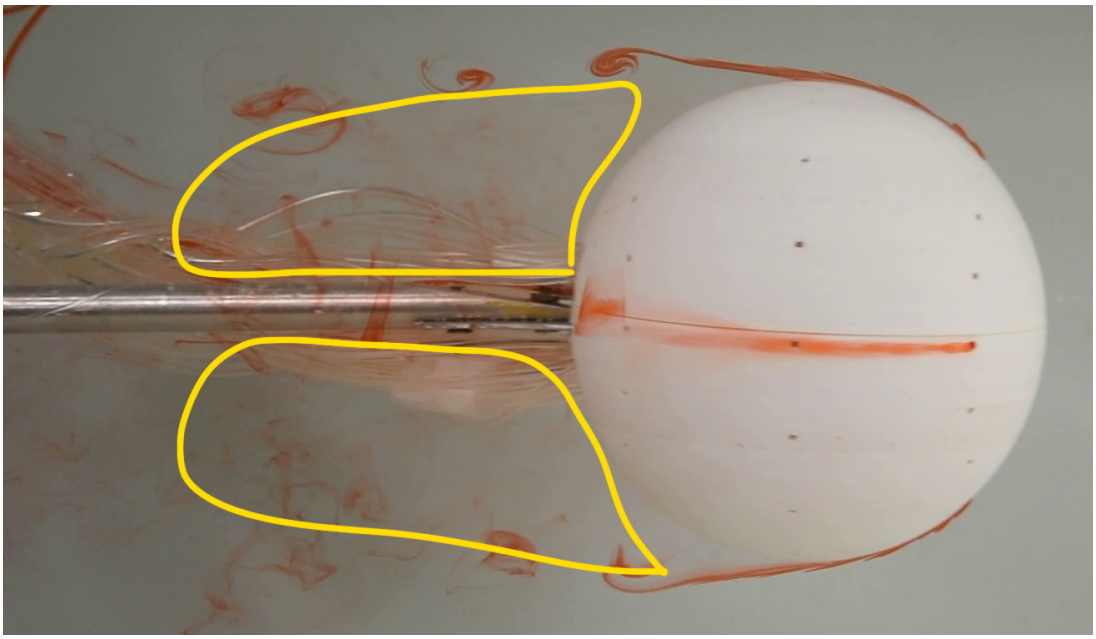

(a) Side View.

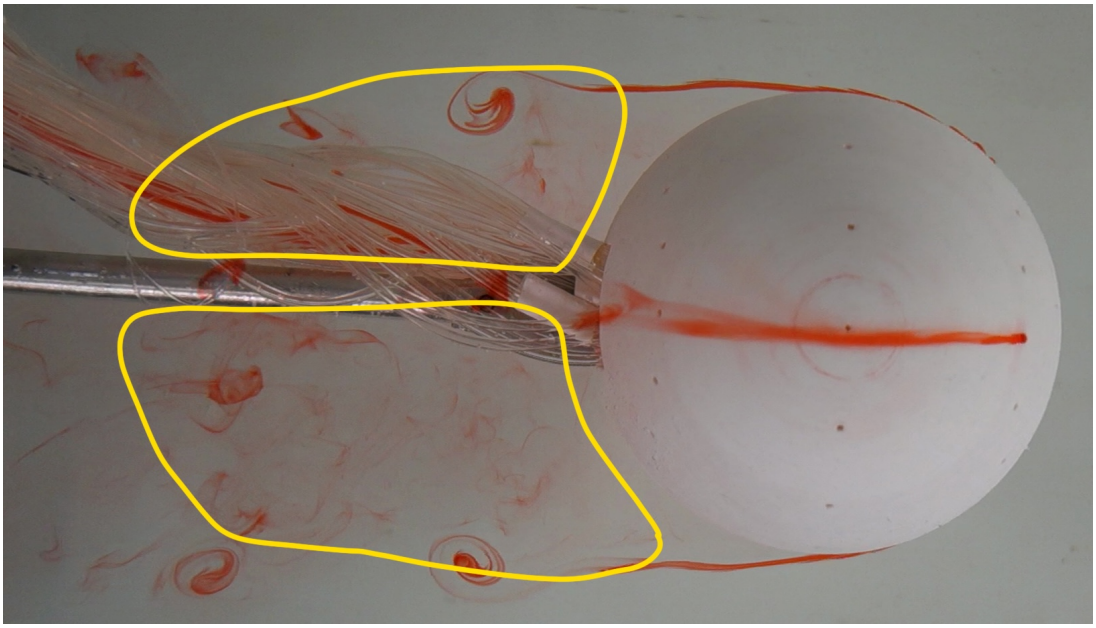

(b) Top view.

Figure 4.17: Sphere wake shape with four ink tubes, at $Re = 6000$.

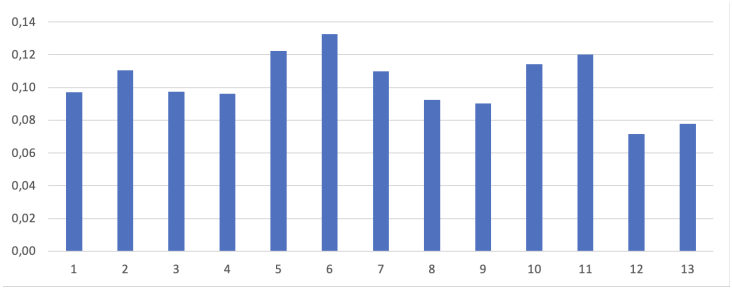

(a) Vortex size for side view.

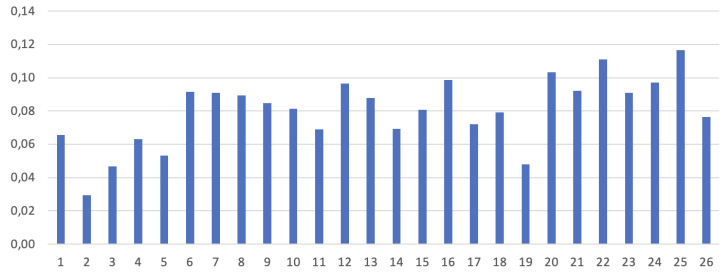

(b) Vortex size for top view.

Figure 4.18: Size of the vortices close to the shape of the sphere, scaled to the diameter of the sphere.

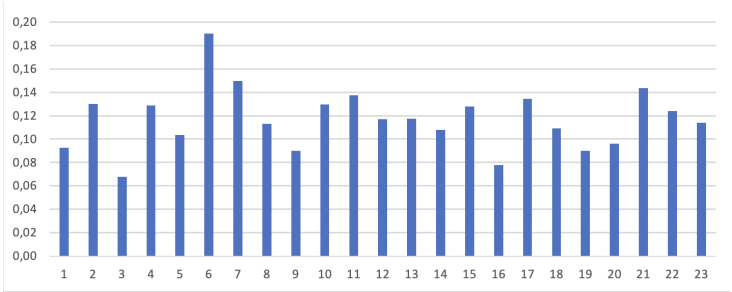

(a) Vortex size for side view.

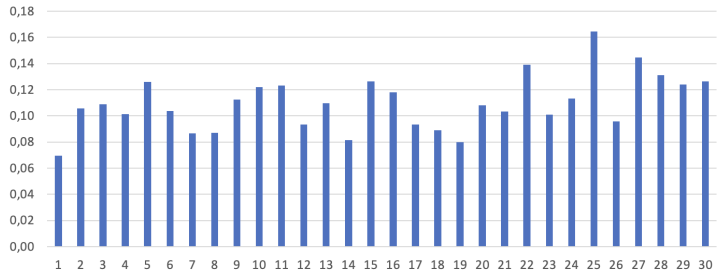

(b) Vortex size for top view.

Figure 4.19: Size of the vortices far to the shape of the sphere, scaled to the diameter of the sphere.

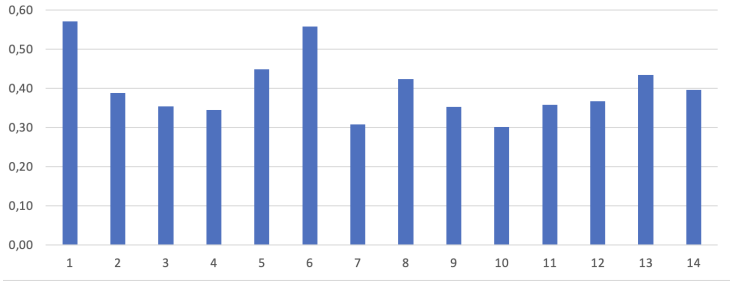

(a) Measurement from side view.

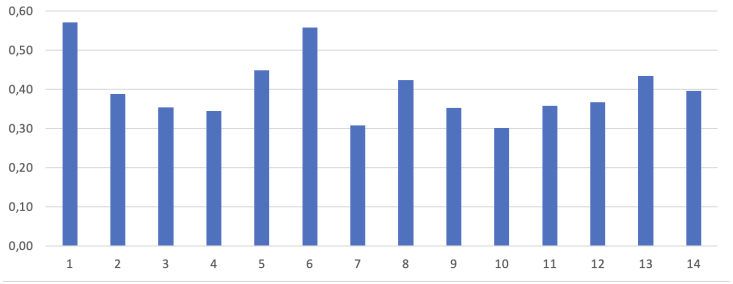

(b) Measurement from top view.

Figure 4.20: Size of the distance between two vortices, scaled to the diameter of the sphere.

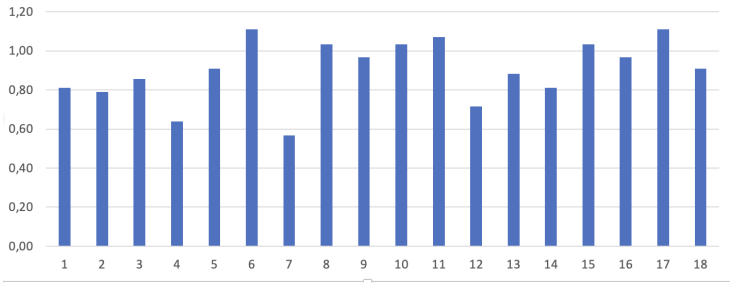

Figure 4.21: Sphere vortex frequency with four ink tubes, at $Re = 6000$.

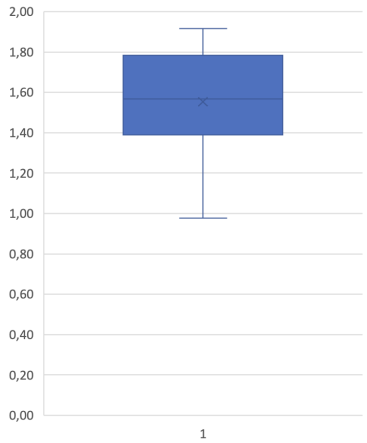

Figure 4.22: Strouhal number of a sphere with four ink tubes, at $Re = 6000$.

Measurement	Average value
Vortex size close to the sphere (SV)	0.10
Vortex size close to the sphere (TV)	0.08
Vortex size far to the sphere (SV)	0.12
Vortex size far to the sphere (TV)	0.11
Distance between two vortices (SV)	0.40
Distance between two vortices (TV)	0.46
Frequency	0.78
Strouhal number	1.34

Table 4.2: Average value of the analysis at $Re = 6000$, using four ink tubes.

4.1.3 Summary Sphere $Re = 6000$

In this section there is the collection of all measurements from the three tests with $Re = 6000$ and the last using just four holes. Measuring 3D vortex is very difficult because the orientation of the vortex is not always the same.

To have a better understanding of the phenomena it has been calculated the error between the average value of using sixteen holes and four holes. The differences between the top view and the side view are caused by the misalignment of the top view camera because it was very difficult to move in a proper way and because of the 3D nature of the system.

The biggest error is of 28%, that confirm the difficulties of taking the measurement of a 3D Vortex. Using also all the holes make it worst to calculate. The average diameter of the vortex is less than the 11% of the size of diameter of the sphere and the distance between two vortexes around the 40% of the diameter of the sphere. The error in the Strouhal number is about the 12% and it is in the same range according to the paper of Sakamoto, as we can see in the following figure 4.60

Measurement	Test 1	Test 2	Test 3	Average value
Vortex size close to the sphere (SV)	0.08	0.07	0.09	0.08
Vortex size close to the sphere (TV)	0.11	0.08	0.11	0.10
Vortex size far to the sphere (SV)	0.14	0.08	0.11	0.11
Vortex size far to the sphere (TV)	0.13	0.08	0.13	0.11
Distance between two vortices (SV)	0.46	0.34	0.40	0.40
Distance between two vortices (TV)	0.39	0.33	0.36	0.36
Frequency (Hz)	0.78	0.78	0.84	0.36
Strouhal number	1.34	1.35	1.46	1.38

Table 4.3: Table with average value the three tests with $Re = 6000$ and θ=45°.

Measurement	Average Value	Test "Four holes"	Error
Vortex size close to the sphere (SV)	0.11	0.08	28%
Vortex size close to the sphere (TV)	0.10	0.07	33%
Vortex size far to the sphere(SV)	0.14	0.17	19%
Vortex size far to the sphere (TV)	0.12	0.14	13%
Distance between two vortices (SV)	0.58	0.51	12%
Distance between two vortices (TV)	0.52	0.63	22%
Frequency	0.89	0.88	1%
Strouhal number	0.89	0.88	1%

Table 4.4: Comparison between Average value and "Four holes" Test $Re = 6000$.

4.1.4 Sphere test $Re = 2000$

In this case the Reynolds number is three times less, in this range the behavior is really different. There is not the same Regular vortex shedding, in this case there is less vortex frequency. Also in this case the wake shape is not divergent as it is possible to see in the side view and top view images. In this configuration it is possible to see that there is instability of the streamline, in this case it is bigger and it is clear to see also in the side view as figure. The vortices' size is less of 15% of the size of the diameter and the distance between two vortices is less than 50% of the sphere. The frequency is in the range of 0,1 Hz to 0,23 Hz, and the Strouhal number is comparatively smaller. 4.24a It is possible to see that in this case the distance between two vortex is bigger. This is probably relegated with the velocity of the cart. The average values of the various measurements taken are collected in table 4.5 .

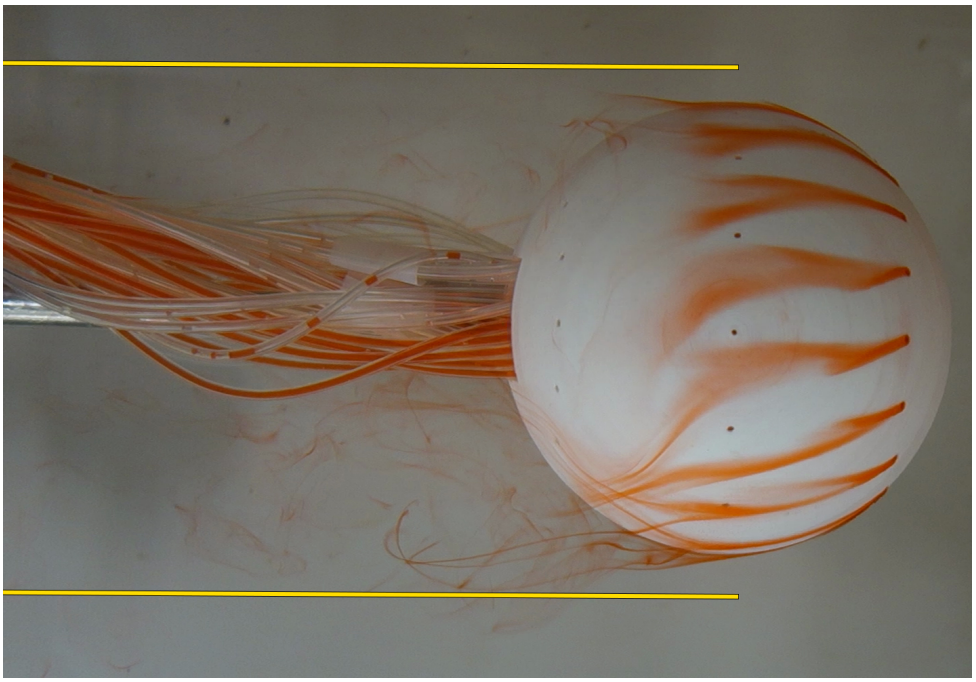

(a) Top view 1.

(b) Top view 2.

Figure 4.23: Sphere wake evolution at $Re = 2000$, Top view.

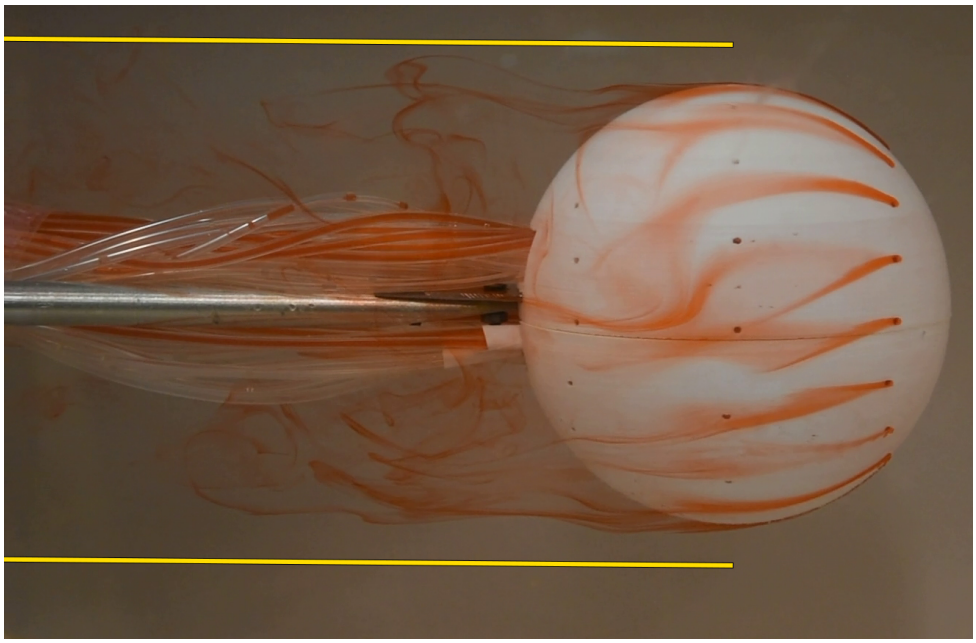

(a) Side view 1.

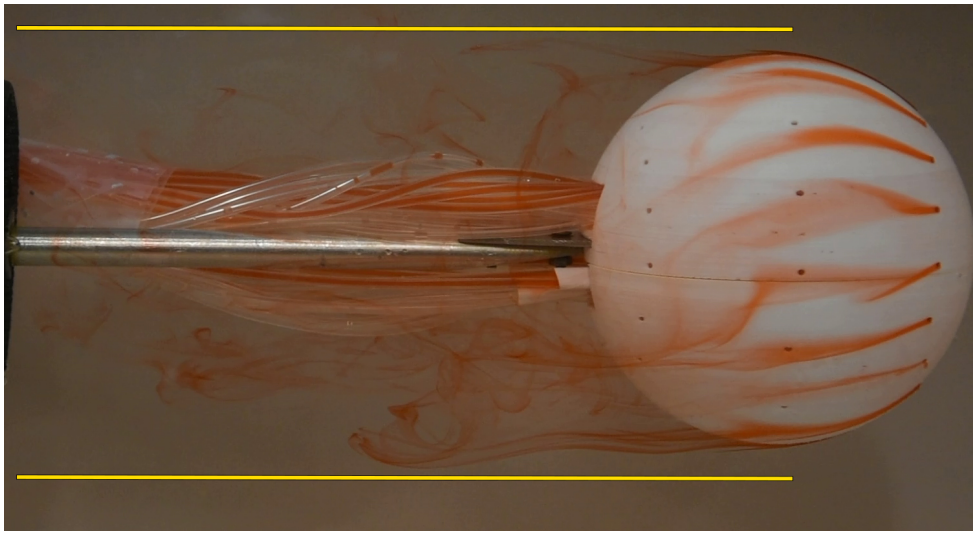

(b) Side view 2.

Figure 4.24: Sphere wake evolution at $Re = 2000$, Side view.

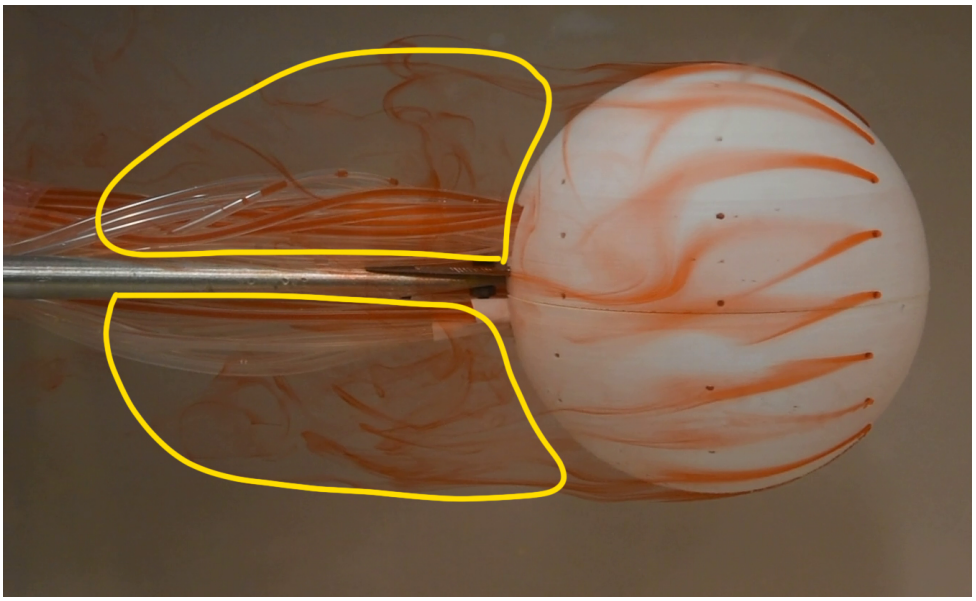

(a) Side View.

(b) Top view.

Figure 4.25: Sphere wake shape at $Re = 2000$ with four ink tubes.

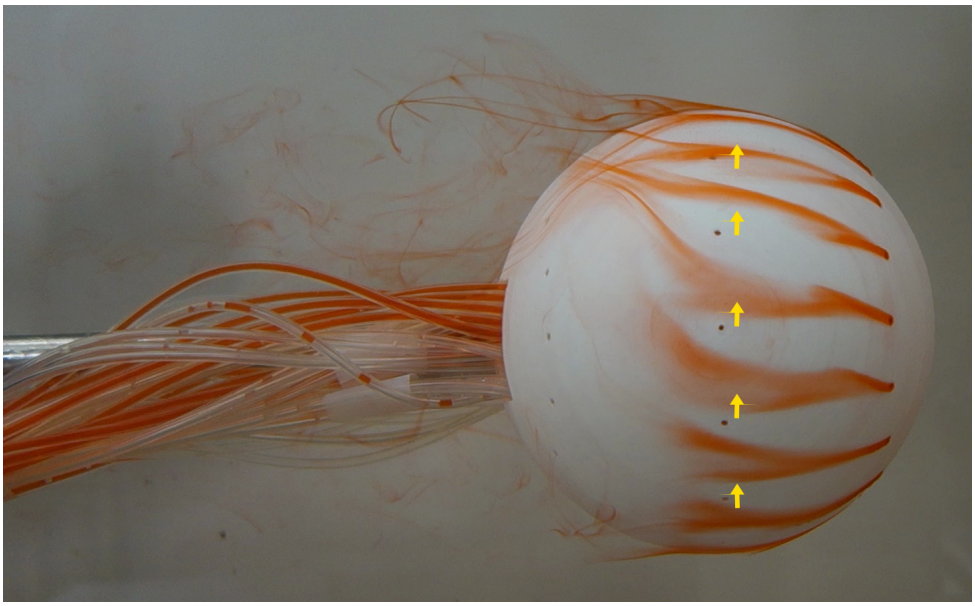

(a) $t = 30$, Top View.

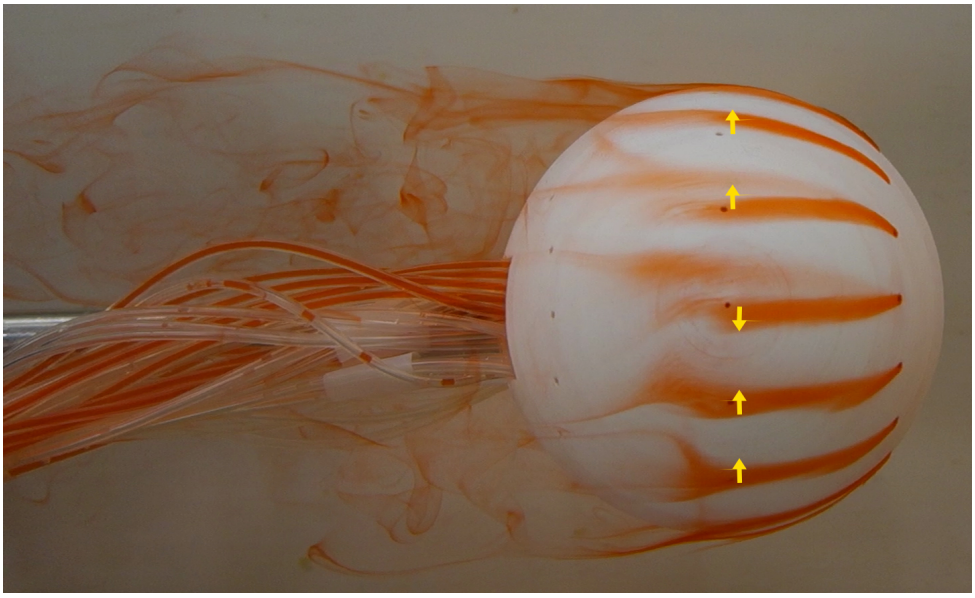

(b) $t = 71s$, Top View.

Figure 4.26: Sphere streamlines instability visualization, at $Re = 2000$.

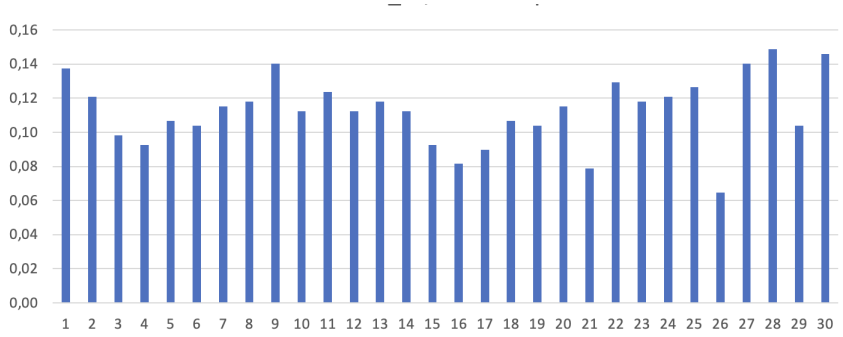

(a) Vortex size for side view.

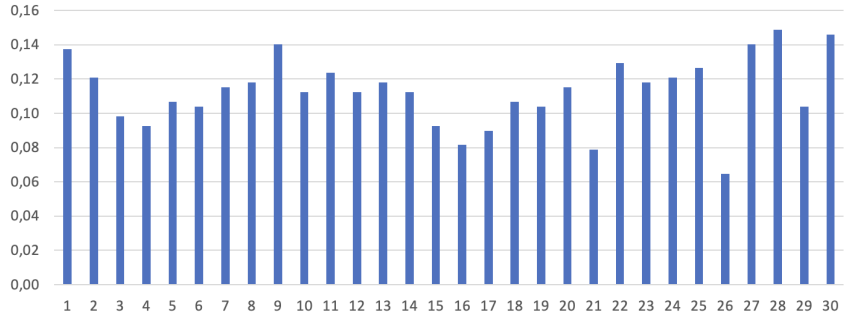

(b) Vortex size for side view.

Figure 4.27: Size of the vortices close to the shape of the sphere, scaled to the diameter of the sphere, at $Re = 2000$.

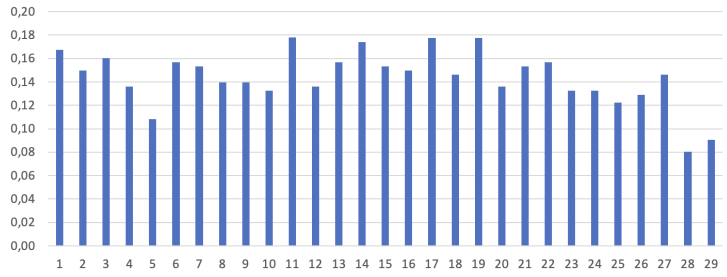

(a) Vortex size for side view.

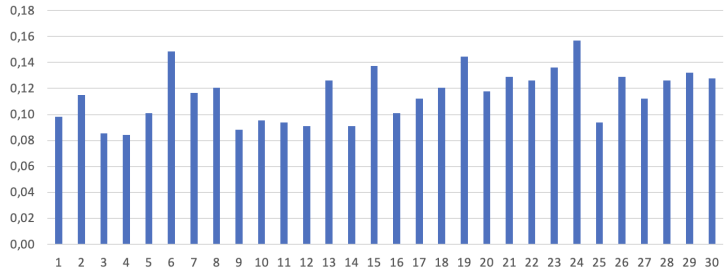

(b) Vortex size for top view.

Figure 4.28: Size of the vortices far to the shape of the sphere, scaled to the diameter of the sphere, at $Re = 2000$.

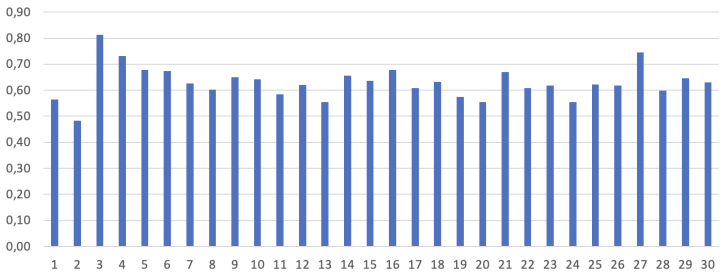

(a) Measurement from side view.

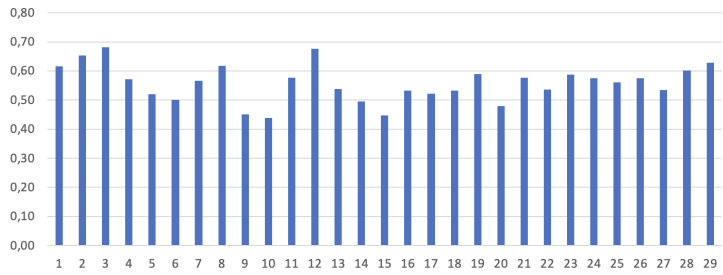

(b) Measurement from top view.

Figure 4.29: Size of the distance between two vortices, scaled to the diameter of the sphere, at $Re = 2000$.

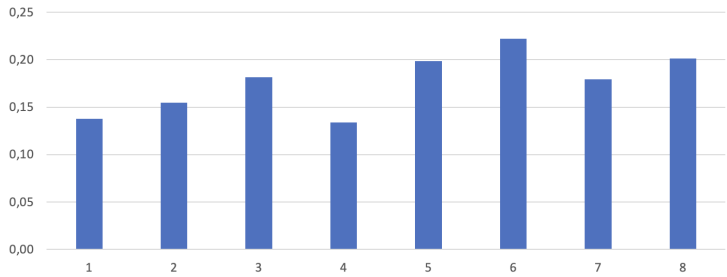

Figure 4.30: Sphere vortex frequency, at $Re = 2000$.

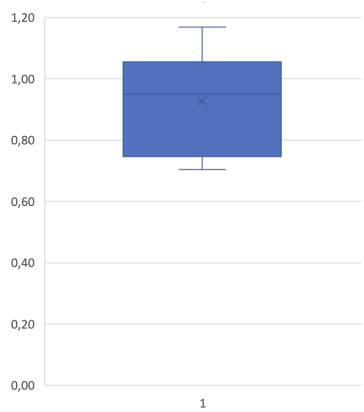

Figure 4.31: Strouhal number of a sphere, at $Re = 2000$.

Measurement	Average value
Vortex size close to the sphere (SV)	0.12
Vortex size close to the sphere (TV)	0.10
Vortex size far to the sphere (SV)	0.16
Vortex size far to the sphere (TV)	0.12
Distance between two vortices (SV)	0.48
Distance between two vortices (TV)	0.45
Frequency (Hz)	0.15
Strouhal number	0.78

Table 4.5: Average value of the analysis of a Sphere, at $Re = 2000$.

4.1.5 Sphere test $Re = 2000$ with four holes visualization

In this case it is possible to see better the vortexes as in the other test with $Re = 6000$ and, as in the other test $Re = 2000$, there is not variation in the behavior. There is a big fluctuation of the measurement about 100%.

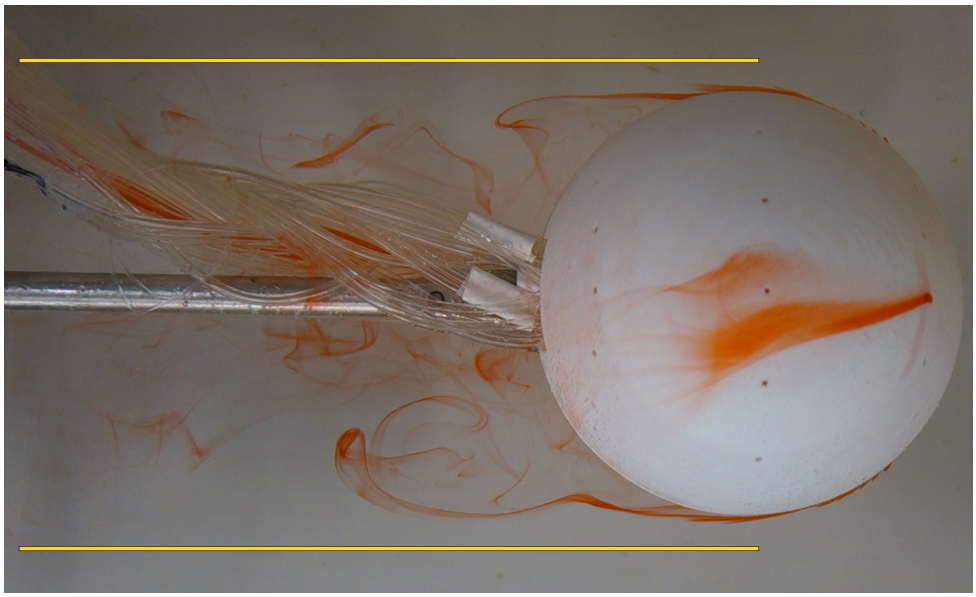

(a) Top view 1.

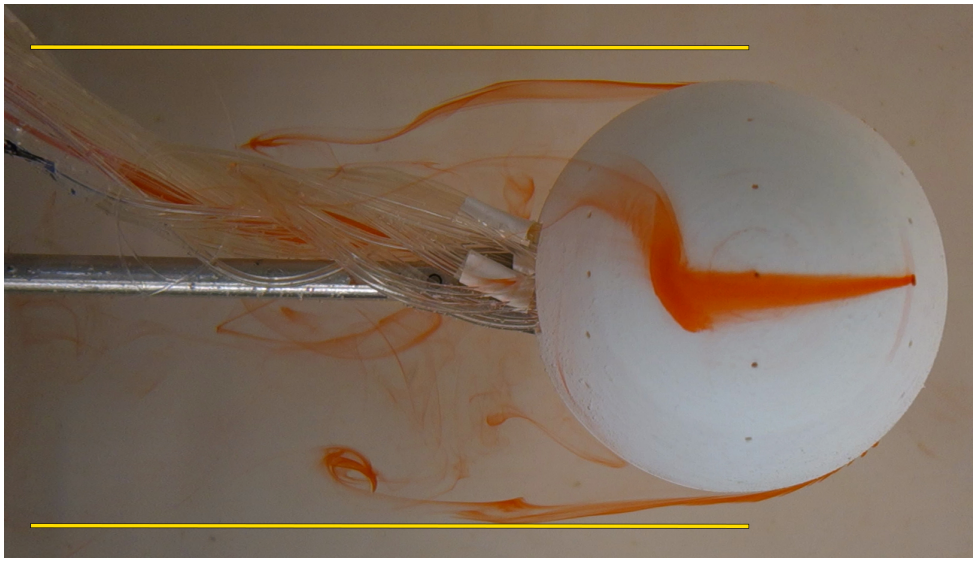

(b) Top view 2.

Figure 4.32: Sphere wake evolution at $Re = 6000$ with four ink tubes, Top view.

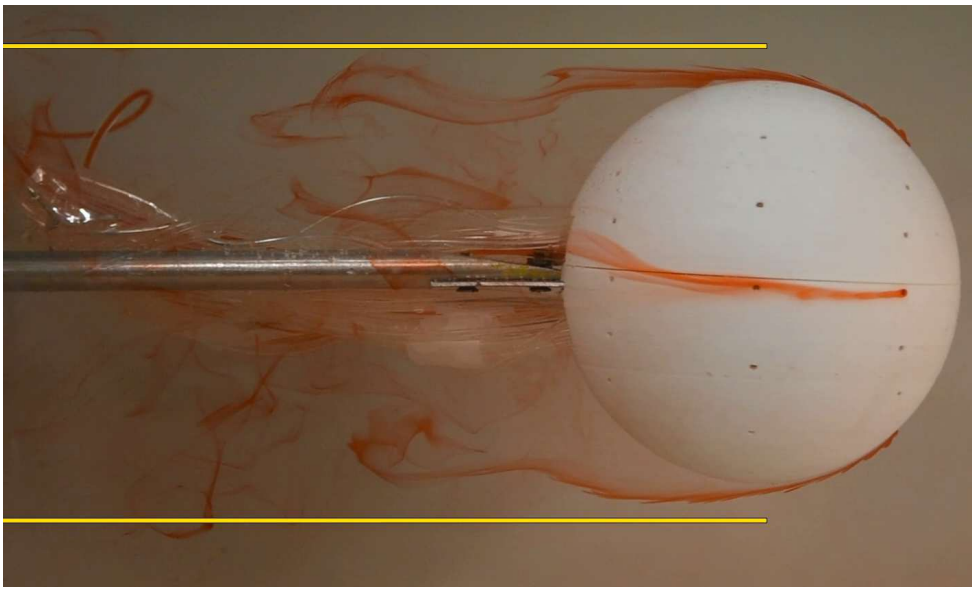

(a) Side view 1.

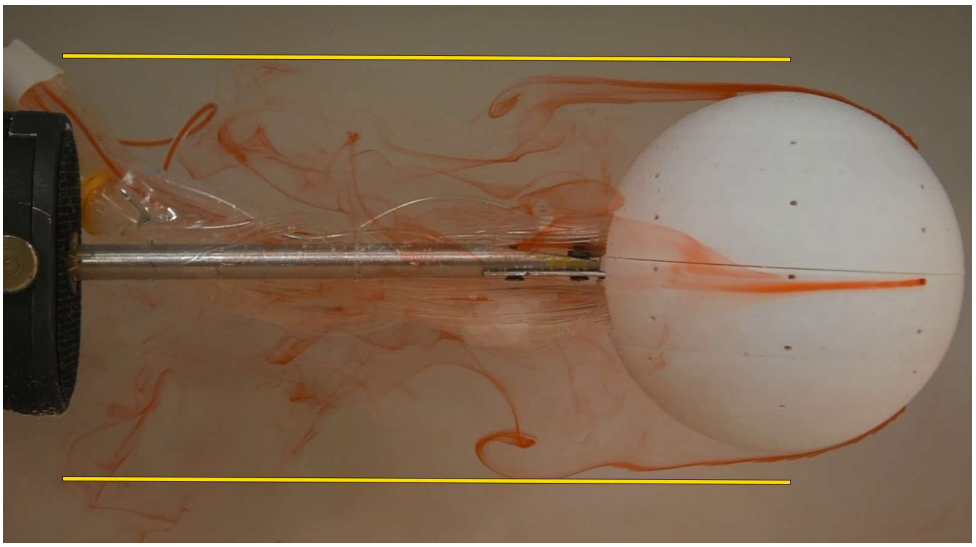

(b) Side view 2.

Figure 4.33: Sphere wake evolution at $Re = 2000$ with four ink tubes, Side view.

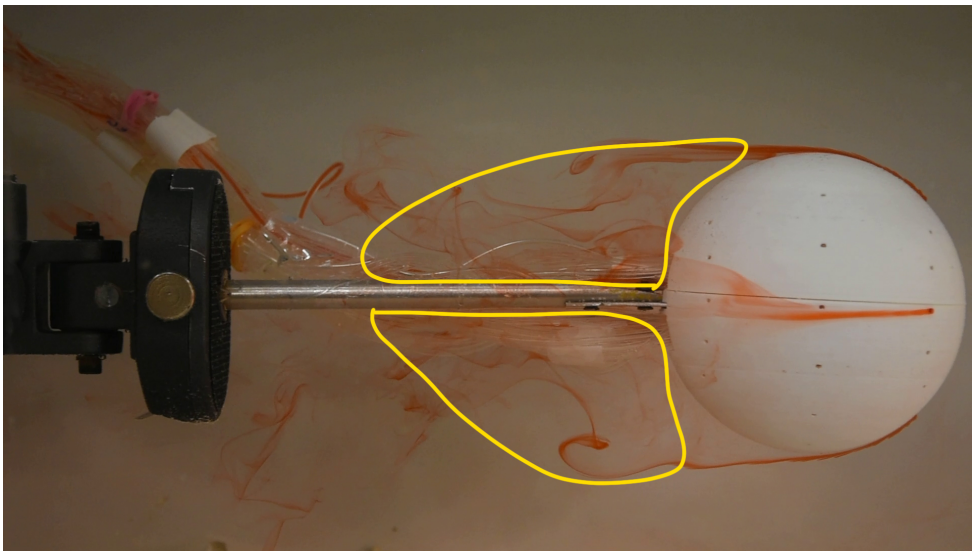

(a) Side View.

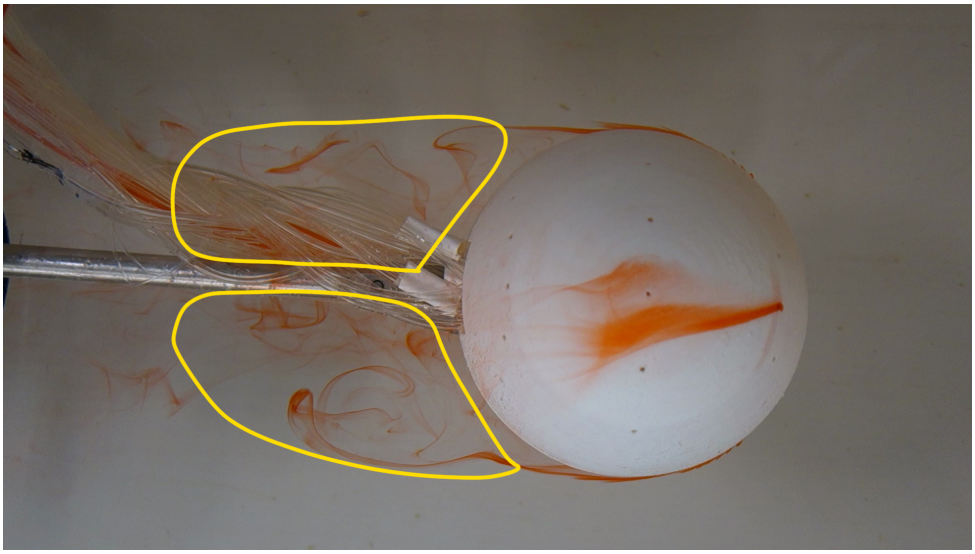

(b) Top view.

Figure 4.34: Sphere wake shape at $Re = 2000$ with four ink tubes.

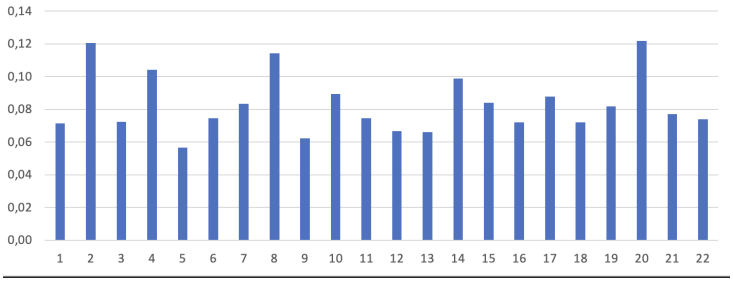

(a) Vortex size for side view.

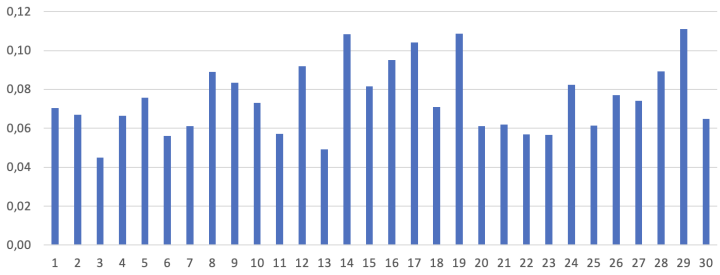

(b) Vortex size for side view.

Figure 4.35: Size of the vortices close to the shape of the sphere, scaled to the diameter of the sphere, at $Re = 2000$.

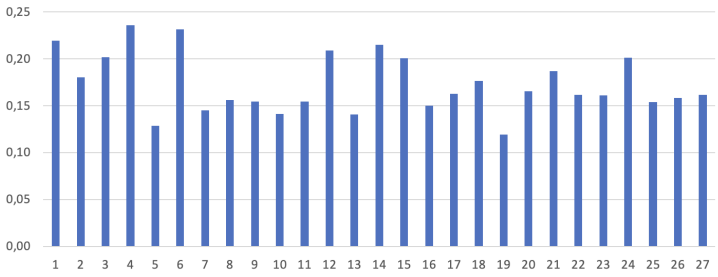

(a) Vortex size for side view.

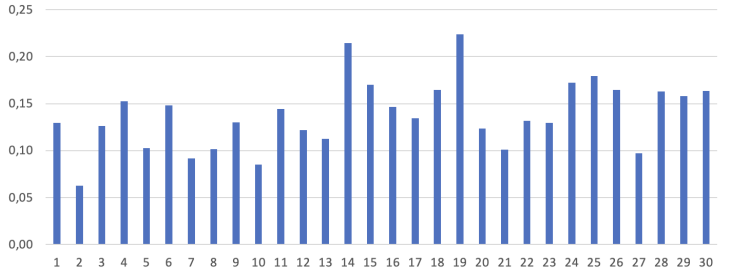

(b) Vortex size for top view.

Figure 4.36: Size of the vortices far to the shape of the sphere, scaled to the diameter of the sphere, at $Re = 2000$.

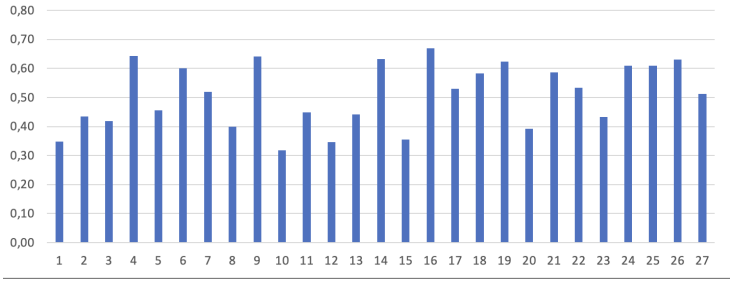

(a) Measurement from side view.

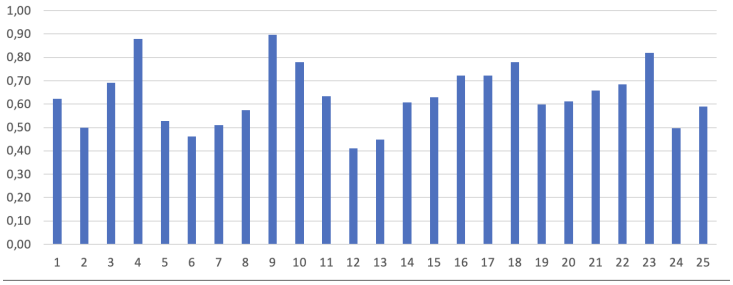

(b) Measurement from top view.

Figure 4.37: Size of the distance between two vortices, scaled to the diameter of the sphere, at $Re = 2000$.

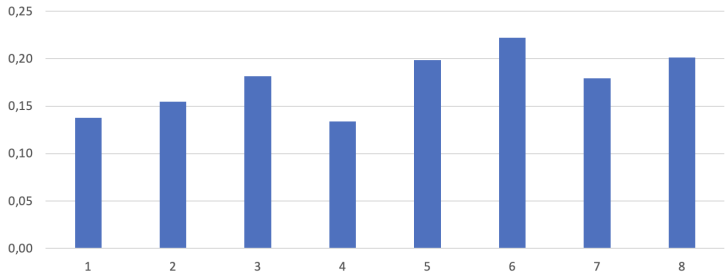

Figure 4.38: Sphere vortex frequency with four ink tubes, at $Re = 2000$.

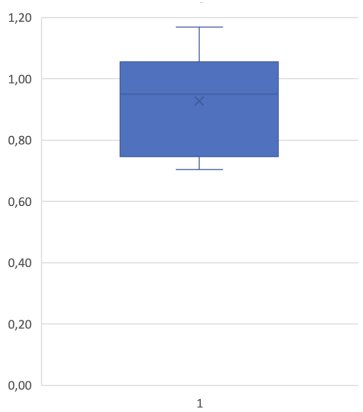

Figure 4.39: Strouhal number of a sphere with four ink tubes, at $Re = 2000$.

Measurement	Average value
Vortex size close to the sphere (SV)	0.11
Vortex size close to the sphere (TV)	0.10
Vortex size far to the sphere (SV)	0.14
Vortex size far to the sphere (TV)	0.12
Distance between two vortices (SV)	0.58
Distance between two vortices (TV)	0.52
Frequency (Hz)	0.17
Strouhal number	0,89

Table 4.6: Average value of the analysis at $Re = 2000$, using four ink tubes.

4.1.6 Summary sphere visualization at $Re = 2000$

In this section there is the collection of all the measurement from the three differ test and the last using just four holes. Measuring 3D vortex is already very difficult and in this test is even worse because there are less vortexes. Also in this case the differences between the top view and the side view are caused by the misalignment of the top view camera because it was very difficult to move in a proper way and because of the 3D nature of the system. The biggest error is of 33%, that confirm the difficulties of taking the measurement of a 3D Vortex. Even using all the holes make it worst to calculate. The average diameter of the vortex is less than the 14% of the size of diameter of the sphere. The error in the Strouhal number is about the 1% and it is in the same range according to the paper of Sakamoto 4.60.

Measurement	Test 1	Test 2	Test 3	Average value
Vortex size close to the sphere (SV)	0.12	0.11	0.10	0.11
Vortex size close to the sphere (TV)	0.10	0.11	0.10	0.10
Vortex size far to the sphere (SV)	0.16	0.14	0.13	0.14
Vortex size far to the sphere (TV)	0.13	0.12	0.14	0.12
Distance between two vortices (SV)	0.46	0.61	0.65	0.58
Distance between two vortices (TV)	0.45	0.52	0.58	0.52
Frequency (Hz)	0.15	0.18	0.18	0.17
Strouhal number	0.78	0.93	0.95	0.89

Table 4.7: Average value all the test at $Re = 2000$.

Measurement	Average Value	”four holes” Test	Error
Vortex size close to the sphere (SV)	0.11	0.08	12%
Vortex size close to the sphere (TV)	0.10	0.07	29%
Vortex size far to the sphere(SV)	0.14	0,17	19%
Vortex size far to the sphere (TV)	0.12	0.14	22%
Distance between two vortices (SV)	0.58	0.51	33%
Distance between two vortices (TV)	0.52	0.63	13%
Frequency	0.17	0.17	
Strouhal number	0.89	0.88	1%

Table 4.8: Comparison between Average value and ”four holes” Test, at $Re = 2000$.

4.1.7 Sphere test using different sections $\theta = 90°$ e $\theta = 145°$

It has been decided to investigate the difference of behavior using different sections. It seems that the case is the same as compared to the holes section of $\theta = 45°$. In all the case the flow is separated and it behaves as in the other test.

Sphere test $Re = 6000$ $\theta = 90°$

It is possible to see that the flow is separated and there is the same vortex shedding that there is in the other test. There is the formation of a strong vortex region.

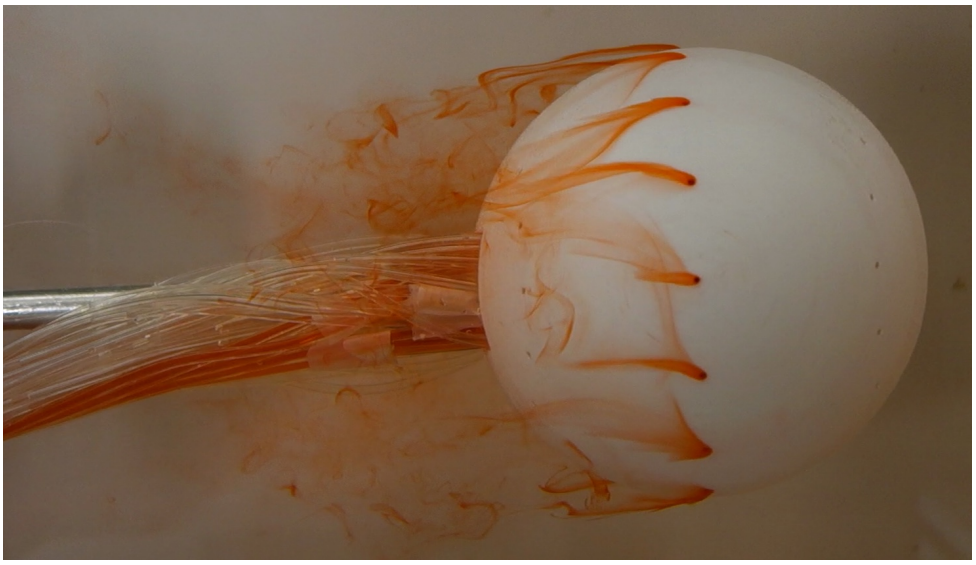

(a) Top View 1.

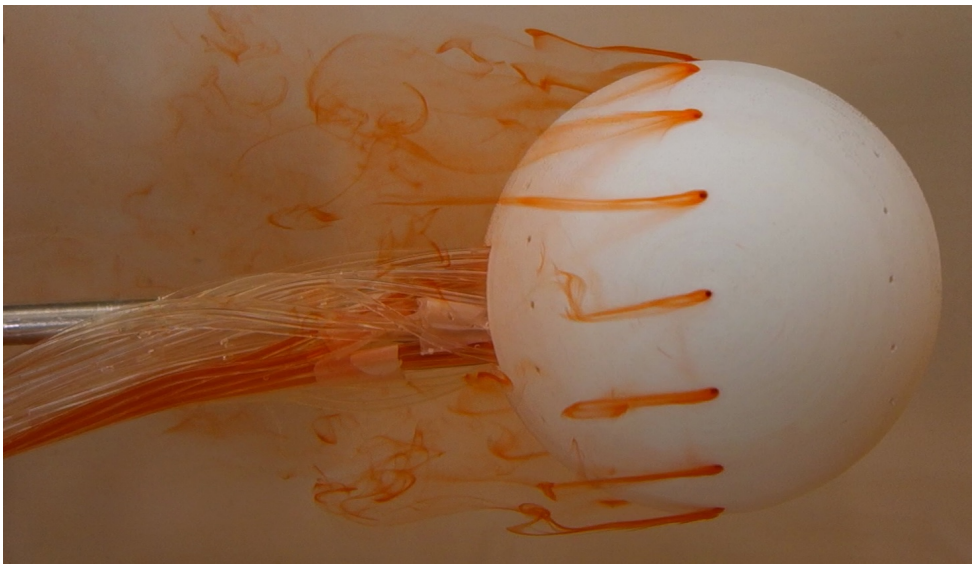

(b) Top View 2.

Figure 4.40: Sphere flow visualisation at $Re = 6000$ and $\theta = 90$.

Sphere test $Re = 2000$ $\theta = 90°$

Also in this case the flow is separated, but compared to the Test $Re = 6000$ $\theta = 90°$ the ink stays in the back in the sphere and it is concentrated in a certain area between $\theta = 90°$ and $\theta = 120°$

(a) Top View 1.

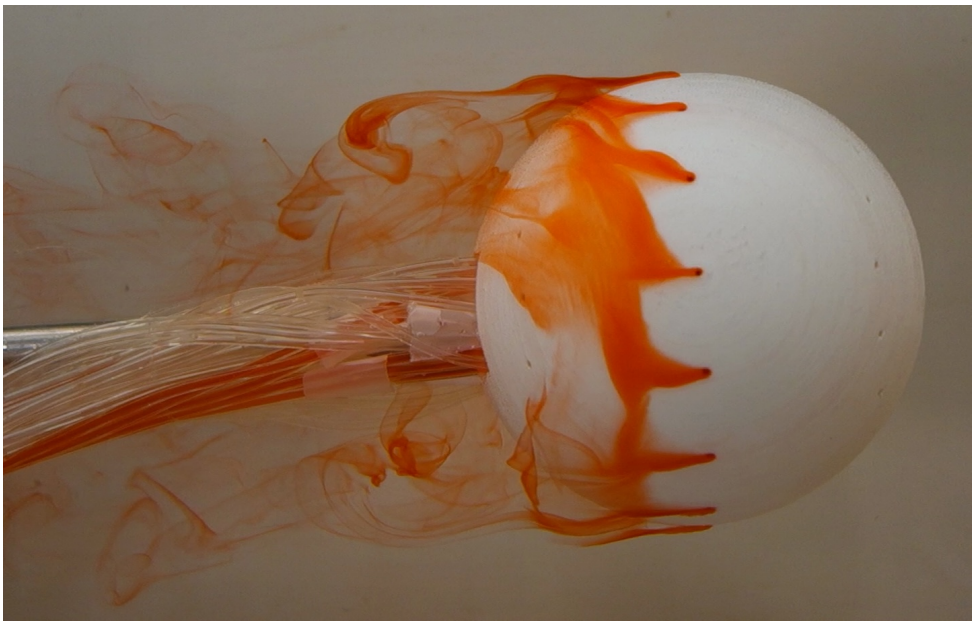

(b) Top View 2.

Figure 4.41: Sphere flow visualisation at $Re = 6000$ and $\theta = 90$.

Sphere test $Re = 6000$ $\theta = 135°$

In this test the ink is injected in the back of the sphere, it is completely separated. It is possible to see that the ink moves also in the direction opposite of the flow defining the wake of the sphere.

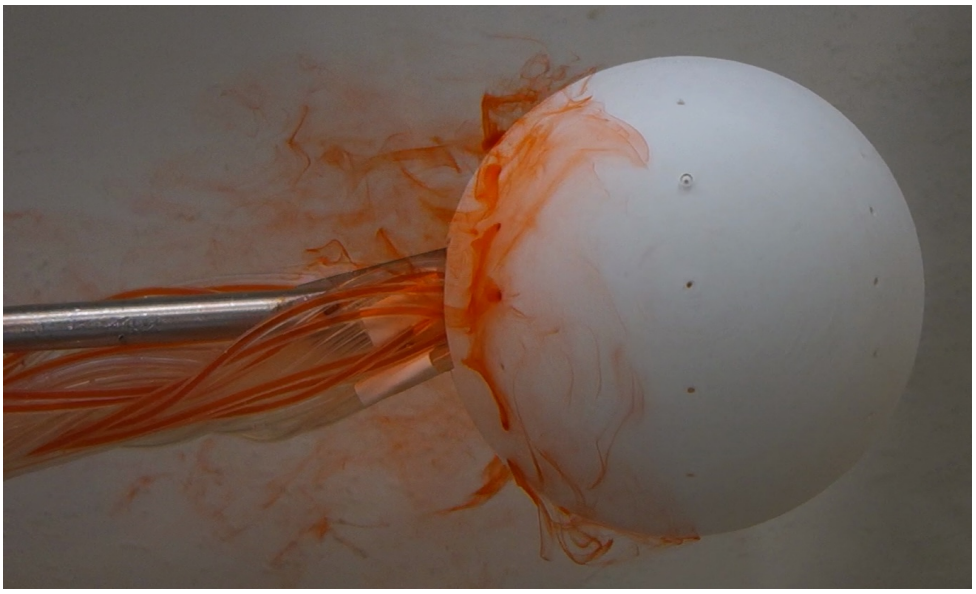

(a) Top View 1.

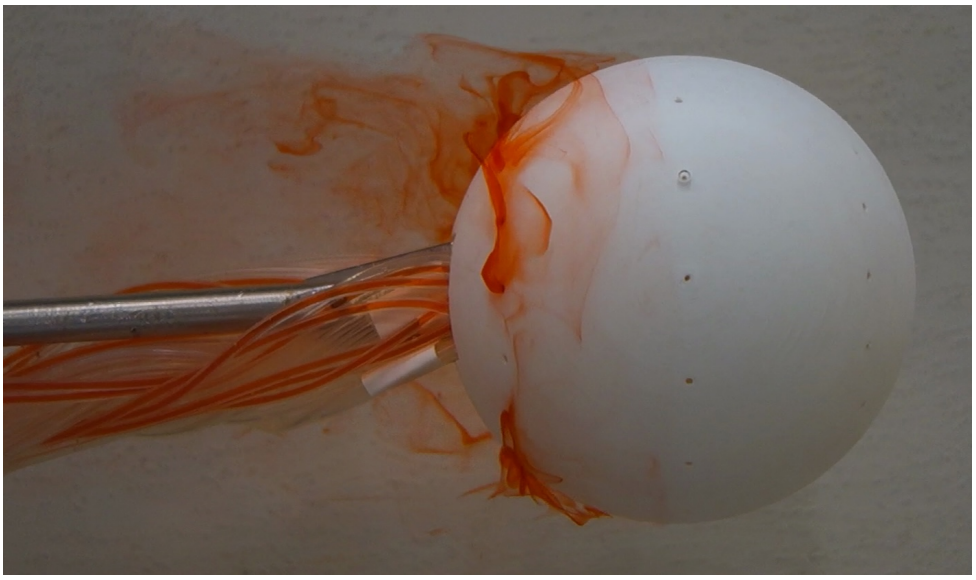

(b) Top View 2.

Figure 4.42: Sphere flow visualisation at $Re = 6000$ and $\theta = 135$.

Sphere Test $Re = 2000$ **e** $\theta = 135°$

Same behavior as the previous test with the flow separated and it can move in the opposite direction of the movement of the prototype.

(a) Top View 1.

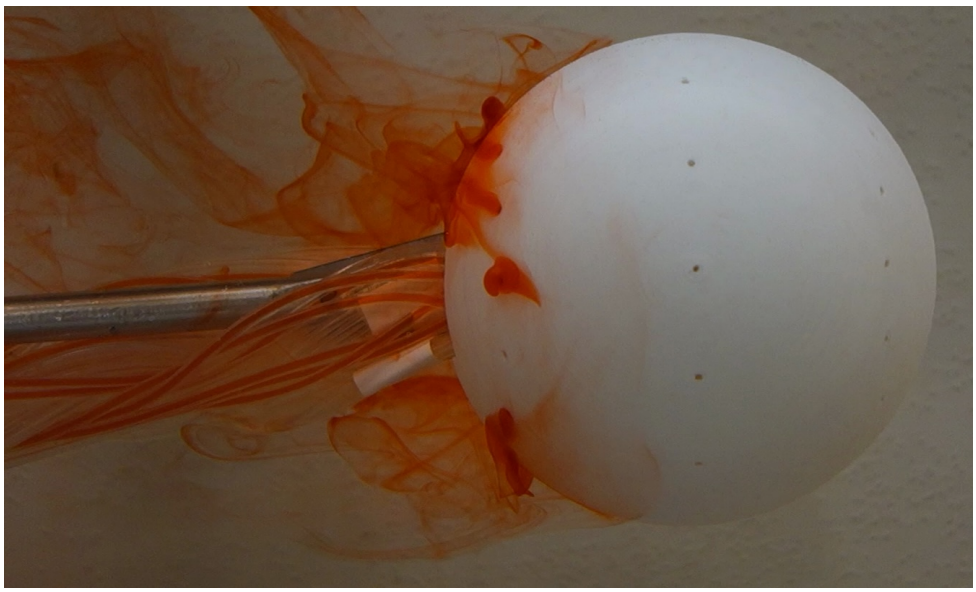

(b) Top View 2.

Figure 4.43: Sphere flow visualisation at $Re = 2000$ and $\theta = 135°$.

4.2 Icosahedron results

The icosahedron is the regular polygon closest to the sphere, it has tewnty faces. For each side of the icosahedron, there is a hole from which the ink will come out. Through the edges, the flow separates, so it is interesting to observe the behavior of this phenomenon. It was decided to place one of the faces of the icosahedron perpendicular to the flow. The wake generated by the icosahedron is divergent. It can be observed that there is a vortex zone after the icosahedron.

It is noticeable that there are two faces where there is a strong separation and stagnation of the flow.

4.2.1 Icosahedron test $Re = 6000$

There is the presence of a vortex region after the icosahedron. In this test, vortex production is irregular; it is not easy to recognize the vortices in detail as in the sphere test at the same Reynolds number. Even the distance between two vortices is not easy to discern. There is not enough instability; the only one that is visible is the one in the frontal face. The average values of the various measurements taken in table 4.9 are collected. There is not enough instability, the only one that it is visible is the one in the frontal face. Using just two holes makes more difficult the calculation of the size because it has been seen less vortex. There is not enough instability, the only one that it is visible is the one in the frontal face. The average size of a vortex is about 14% of the length of the icosahedron, instead the distance between two vortexes is about the 70%. However, the Strouhal number appears to be like that calculated in the same sphere case 4.60. The average values of the various measurements taken are collected in table 4.9 .

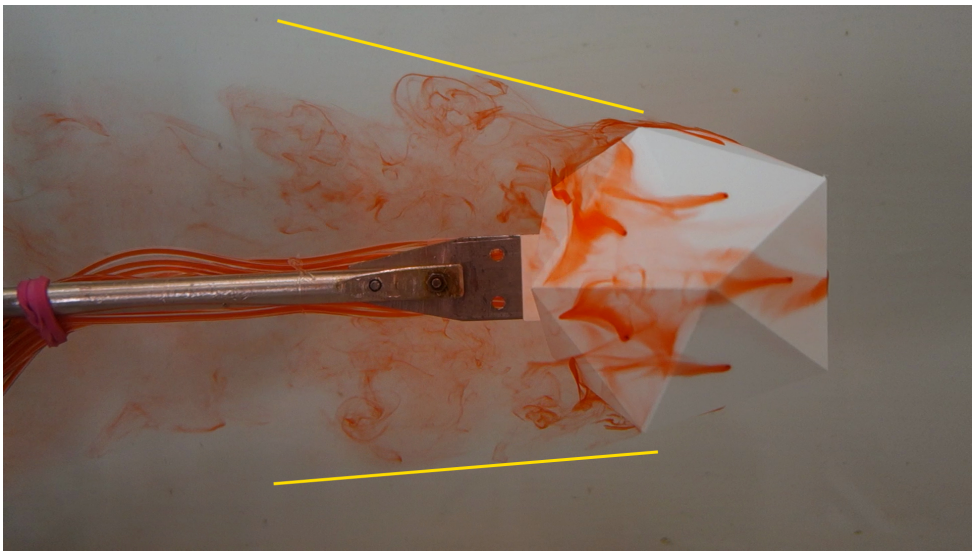

(a) Top view 1.

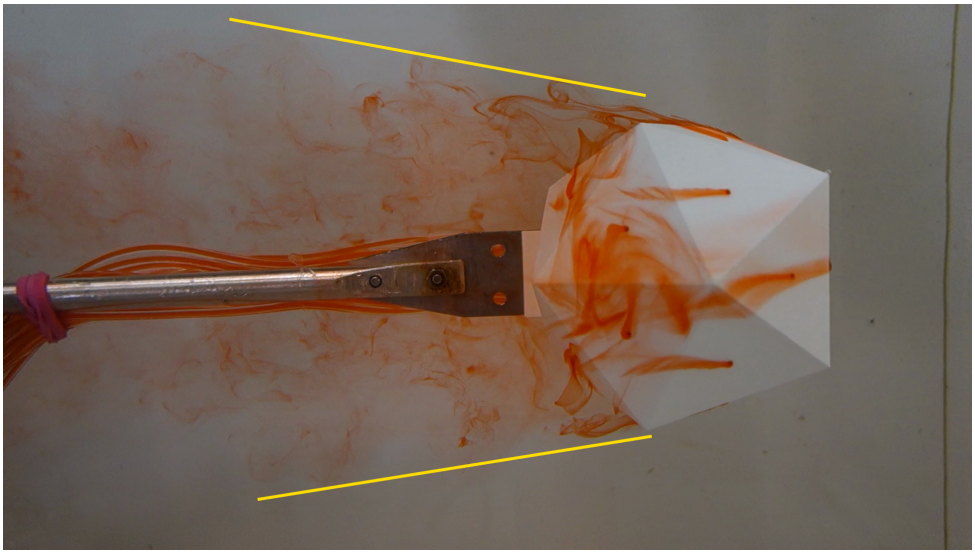

(b) Top view 2

Figure 4.44: icosahedron wake evolution at $Re = 6000$, Top view.

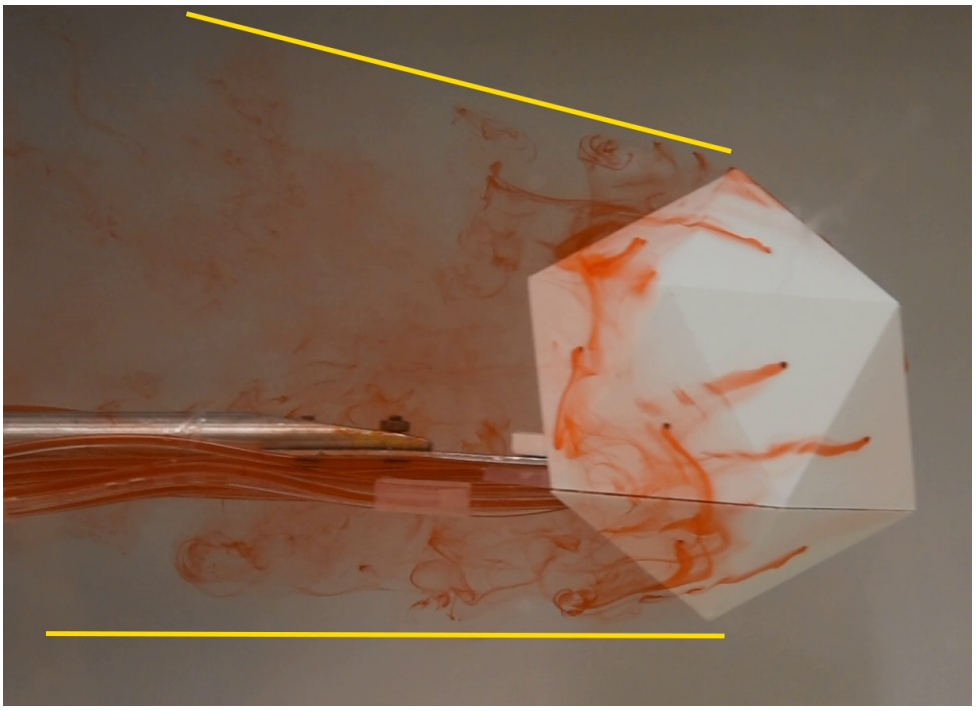

(a) Side view 1.

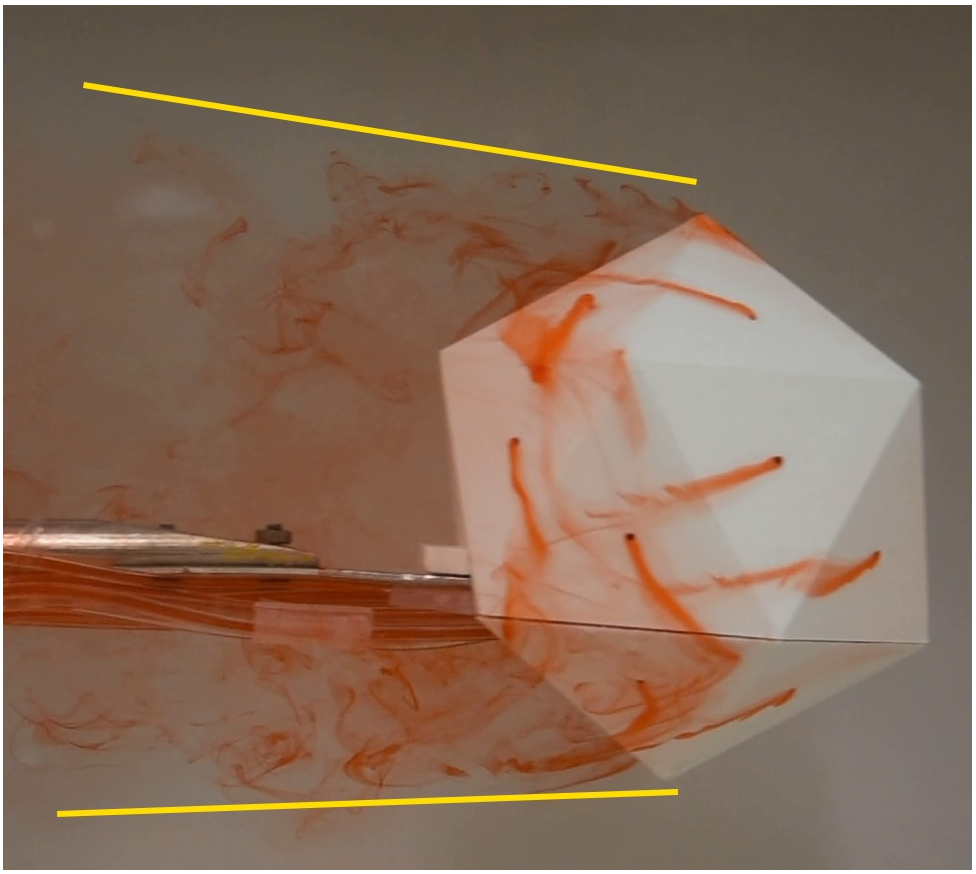

(b) Side view 2.

Figure 4.45: icosahedron wake evolution at $Re = 6000$, Side view.

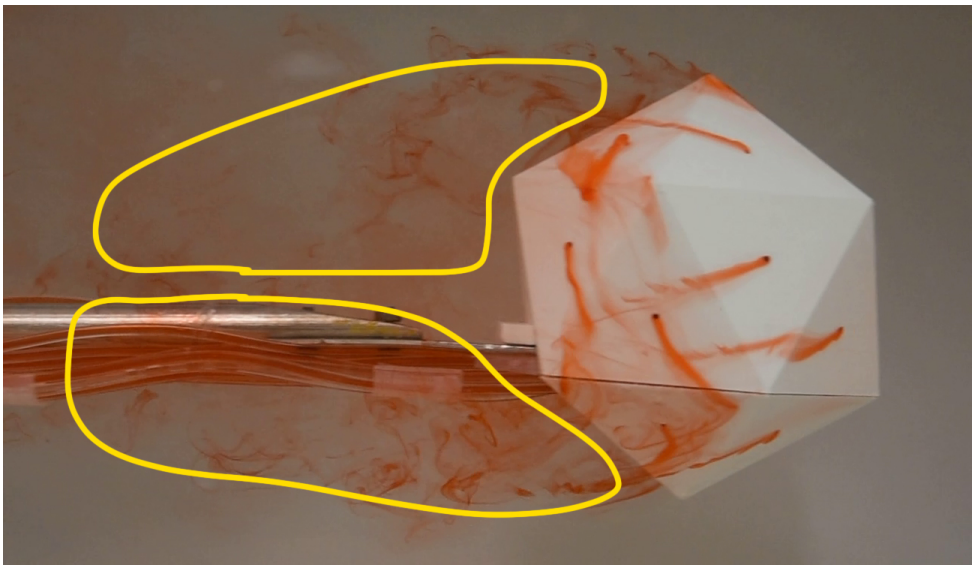

(a) Side View.

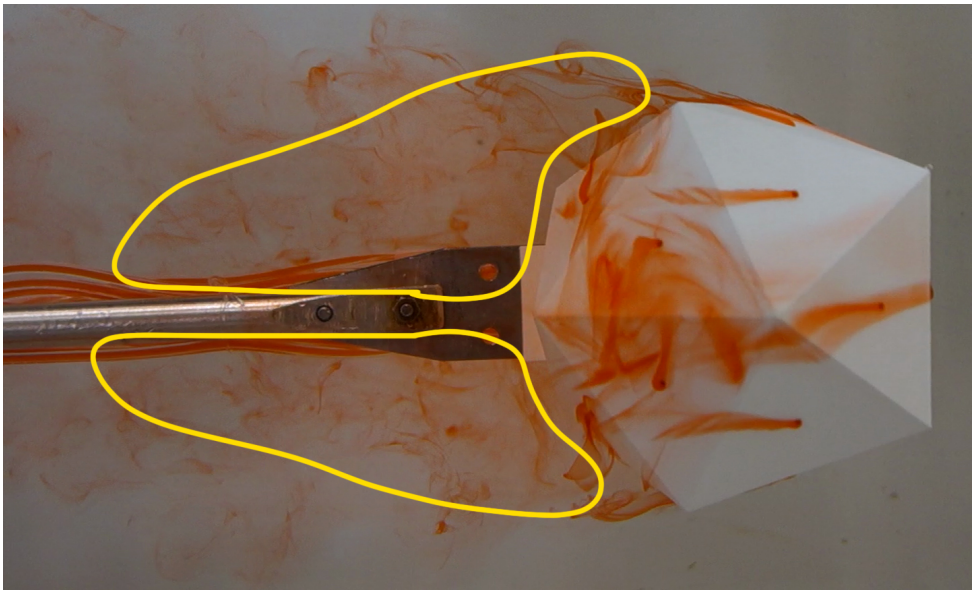

(b) Top view.

Figure 4.46: icosahedron wake shape at $Re = 6000$.

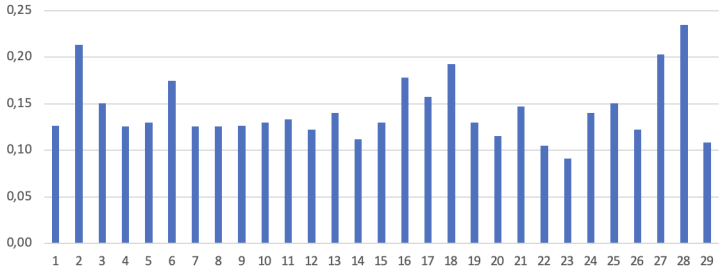

(a) Vortex size for side view.

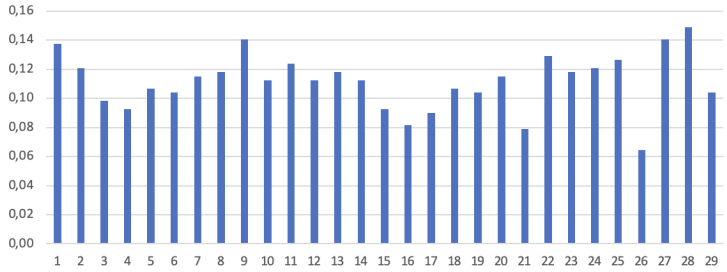

(b) Vortex size for top view.

Figure 4.47: Size of the vortices close to the shape of the icosahedron, scaled to the diameter of the icosahedron.

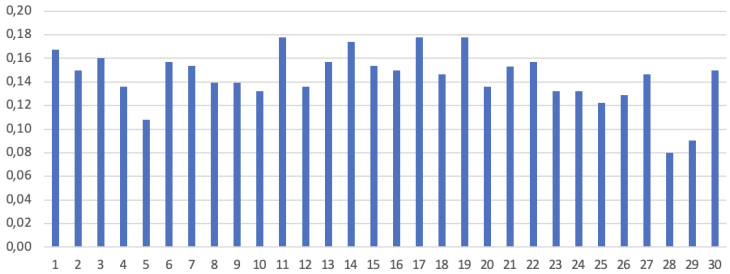

(a) Vortex size for side view.

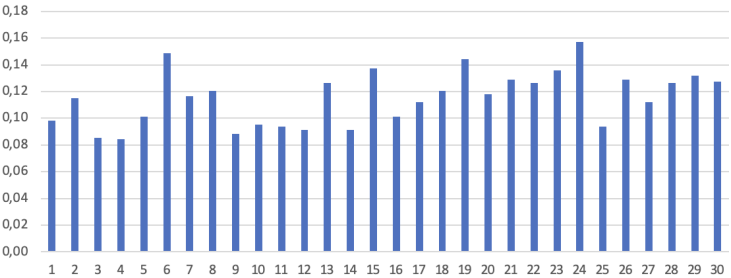

(b) Vortex size for top view.

Figure 4.48: Size of the vortices far to the shape of the icosahedron, scaled to the diameter of the icosahedron.

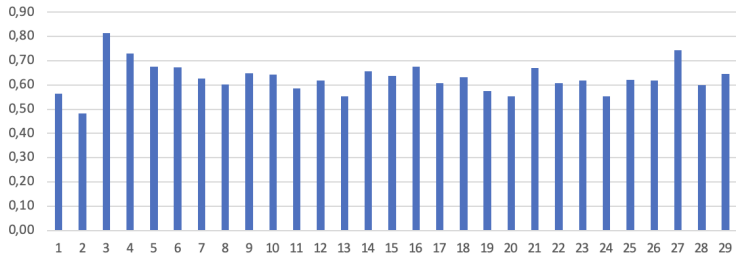

(a) Measurement from side view.

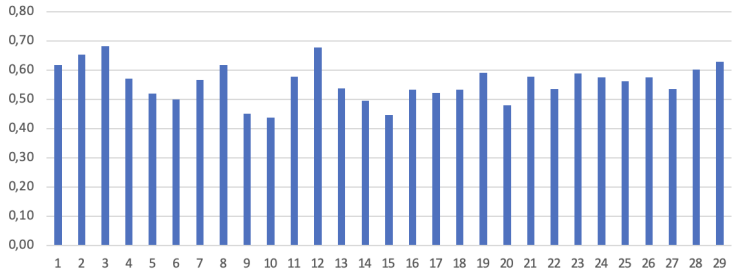

(b) Measurement from top view.

Figure 4.49: Size of the distance between two vortices, scaled to the diameter of the icosahedron.

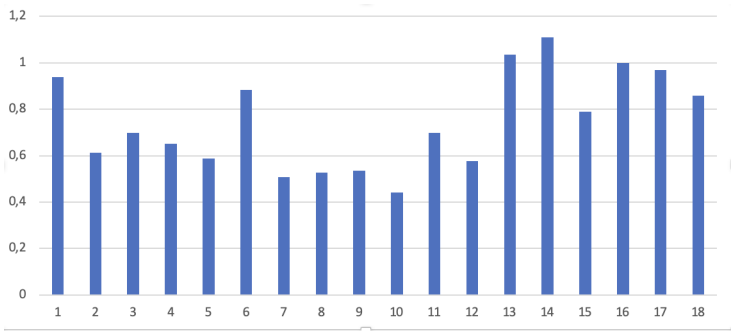

Figure 4.50: icosahedron vortex frequency, at $Re = 6000$.

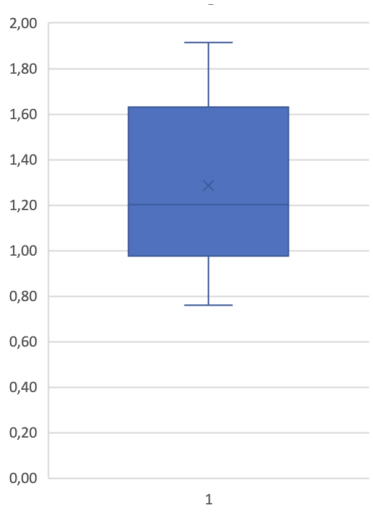

Figure 4.51: Strouhal number of an icosahedron at $Re = 6000$.

Measurement	Average value
Vortex size close to the sphere (SV)	0.14
Vortex size close to the sphere (TV)	0.12
Vortex size far to the sphere (SV)	0.14
Vortex size far to the sphere (TV)	0.12
Distance between two vortices (SV)	0.68
Distance between two vortices (TV)	0.6
Frequency	0.74
Strouhal number	1.29

Table 4.9: Average value of the analysis, icosahedron at $Re = 6000$.

4.2.2 Icosahedron test $Re = 2000$

In this test at $Re = 2000$, the behavior is very similar to that seen at $Re = 6000$. We are dealing with a divergent wake, and there is the presence of a strong vortex zone. In this case, the flow appears less irregular, but it is only due to the lower velocity. The irregularity in vortex sizes and the distance between two vortices is confirmed. The average size of a vortex is about 20% of the length of the icosahedron, Instead the distance between two vortexes is about the 70%. Similarly, in this case, the Strouhal number is similar to the corresponding value for the sphere 4.60. The average values of the various measurements taken are collected in table 4.10 .

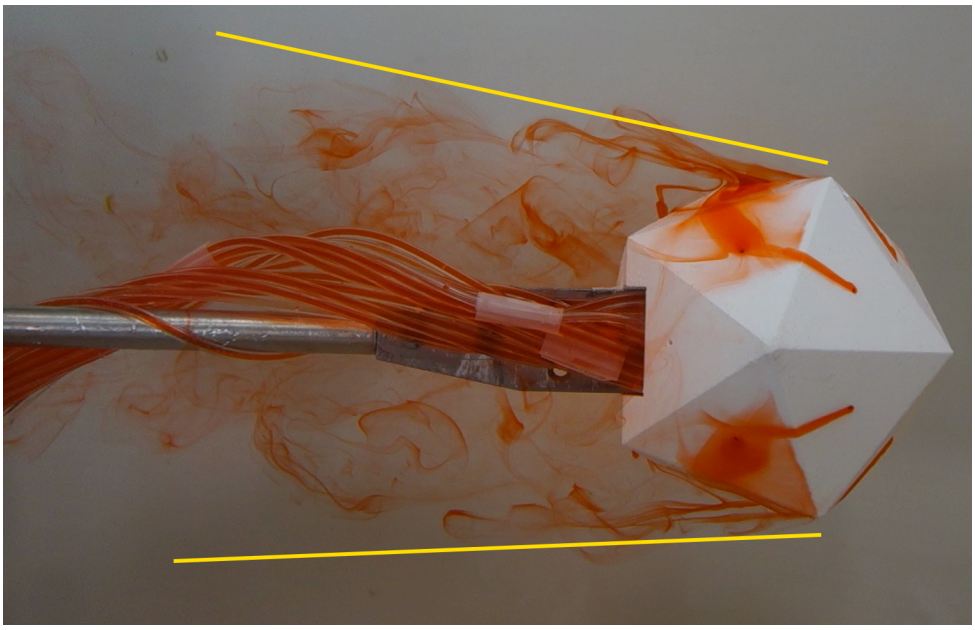

(a) Top view 1.

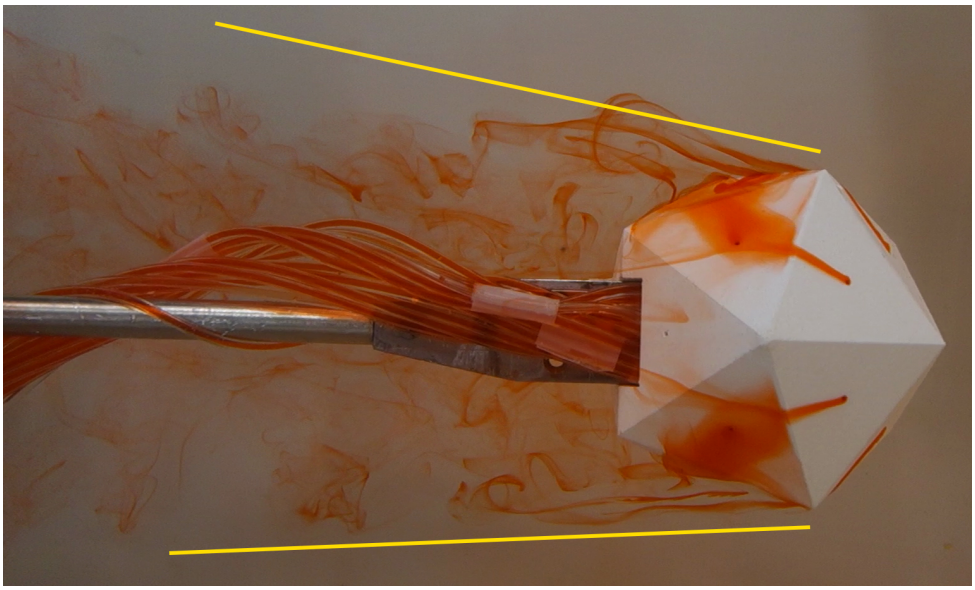

(b) Top view 2.

Figure 4.52: icosahedron wake evolution at $Re = 2000$, Top view.

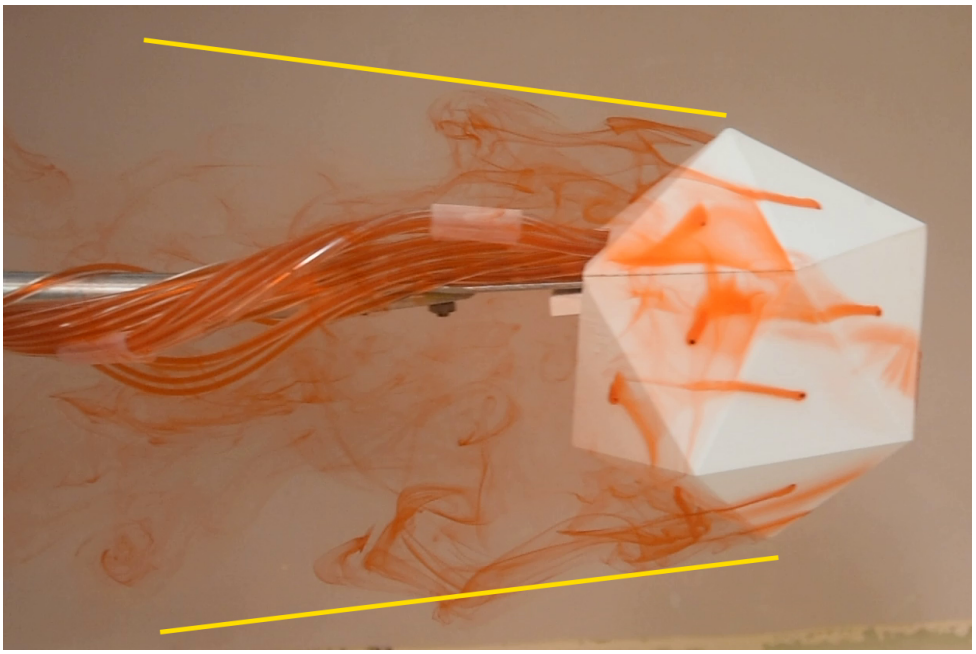

(a) Side view 1.

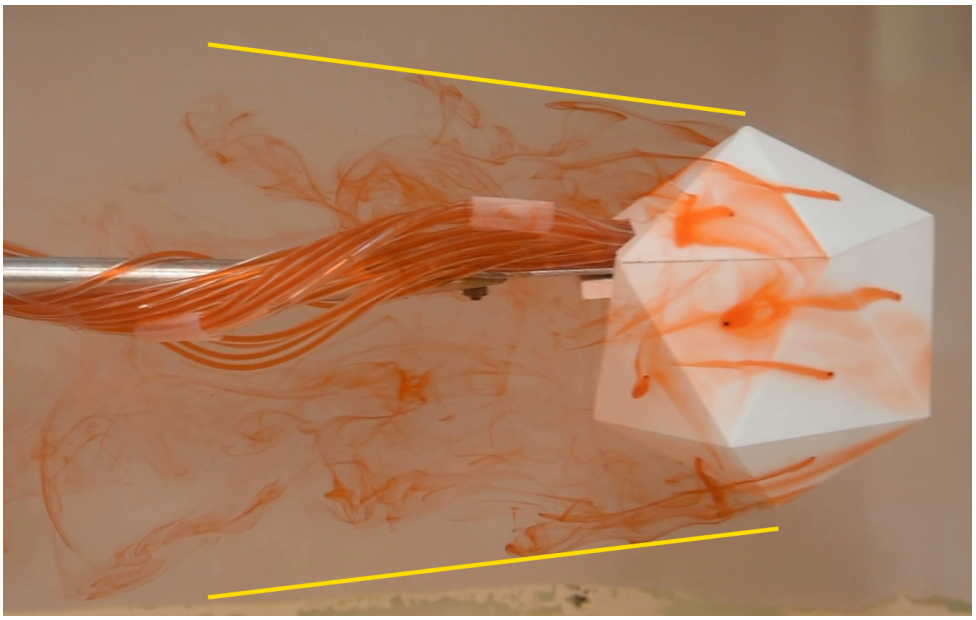

(b) Side view 2.

Figure 4.53: icosahedron wake evolution of a icosahedron at $Re = 2000$, Side view.

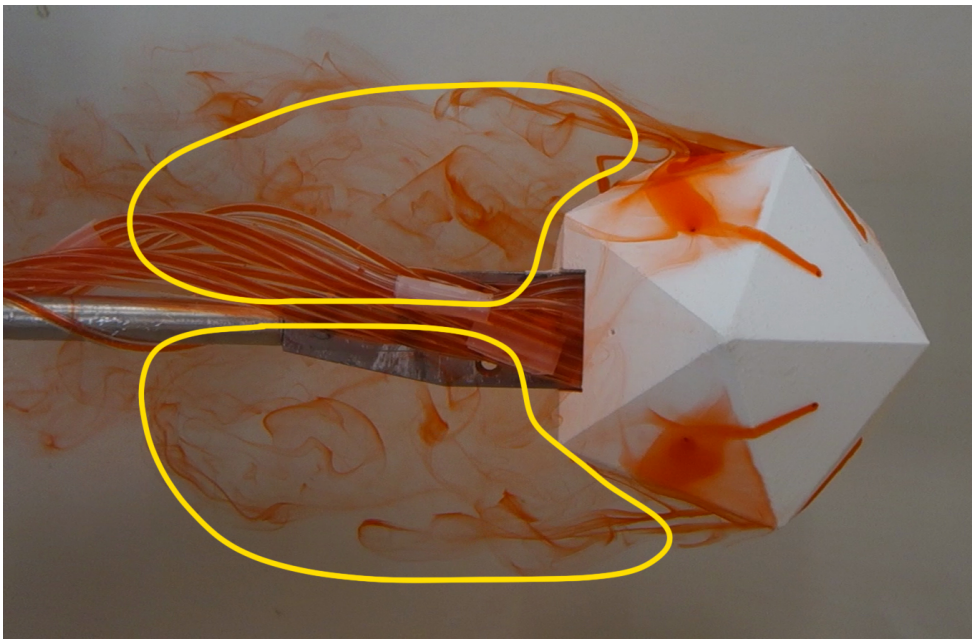

(a) Side View.

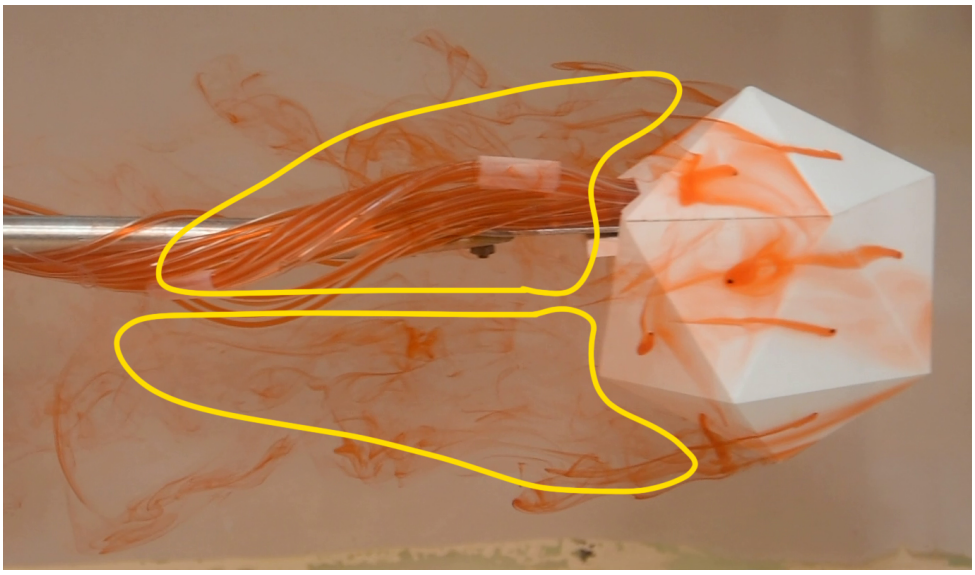

(b) Top view.

Figure 4.54: icosahedron wake shape at $Re = 2000$.

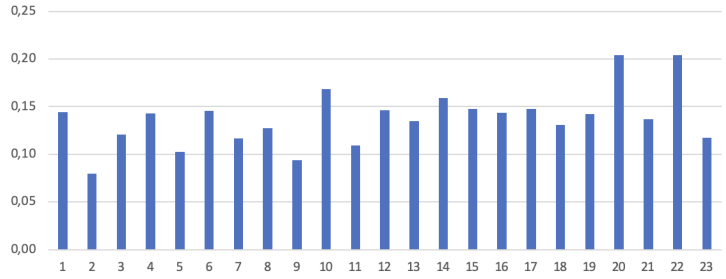

(a) Vortex size for side view.

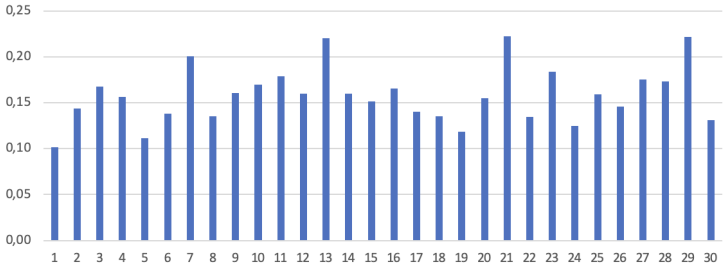

(b) Vortex size for top view.

Figure 4.55: Size of the vortices close to the shape of the icosahedron, scaled to the length of the icosahedron.

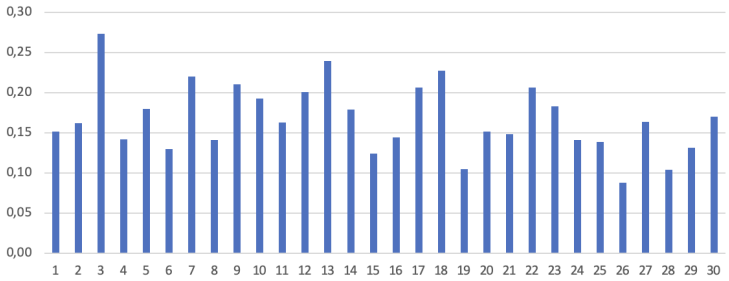

(a) Vortex size for side view.

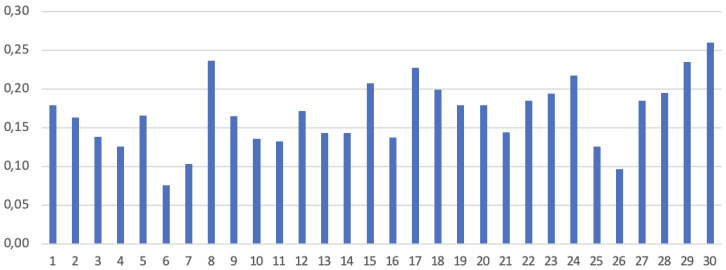

(b) Vortex size for top view.

Figure 4.56: Size of the vortices far to the shape of the icosahedron, scaled to the length of the icosahedron.

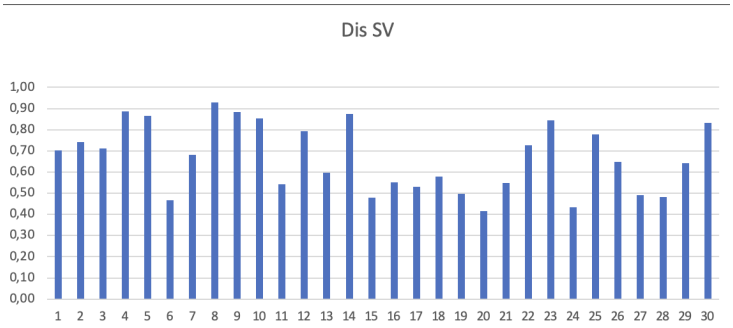

(a) Measurement from side view.

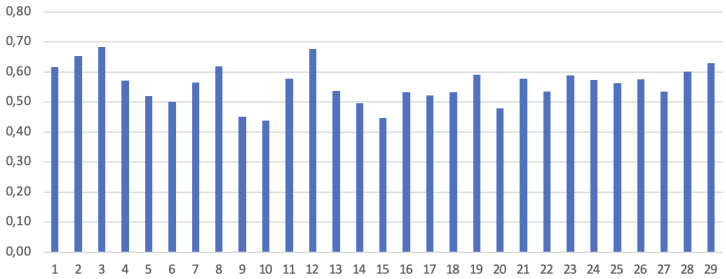

(b) Measurement from top view.

Figure 4.57: Size of the distance between two vortices, scaled to the length of the icosahedron.

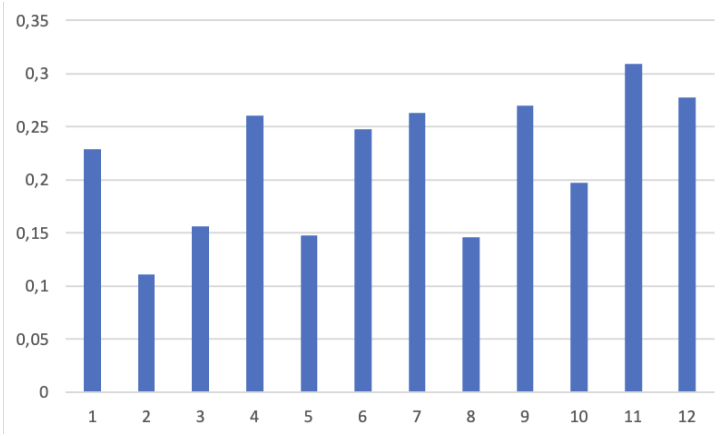

Figure 4.58: icosahedron vortex frequency, at $Re = 2000$.

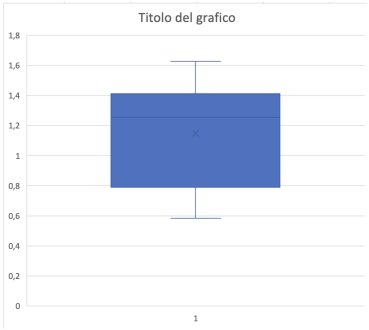

Figure 4.59: Strouhal number of an icosahedron at $Re = 2000$.

Measurement	Average value
Vortex size close to the sphere (SV)	0.14
Vortex size close to the sphere (TV)	0.16
Vortex size far to the sphere (SV)	0.17
Vortex size far to the sphere (TV)	0.19
Distance between two vortices (SV)	0.68
Distance between two vortices (TV)	0.63
Frequency	0.21
Strouhal number	1.15

Table 4.10: Average value of the analysis, icosahedron at $Re = 2000$.

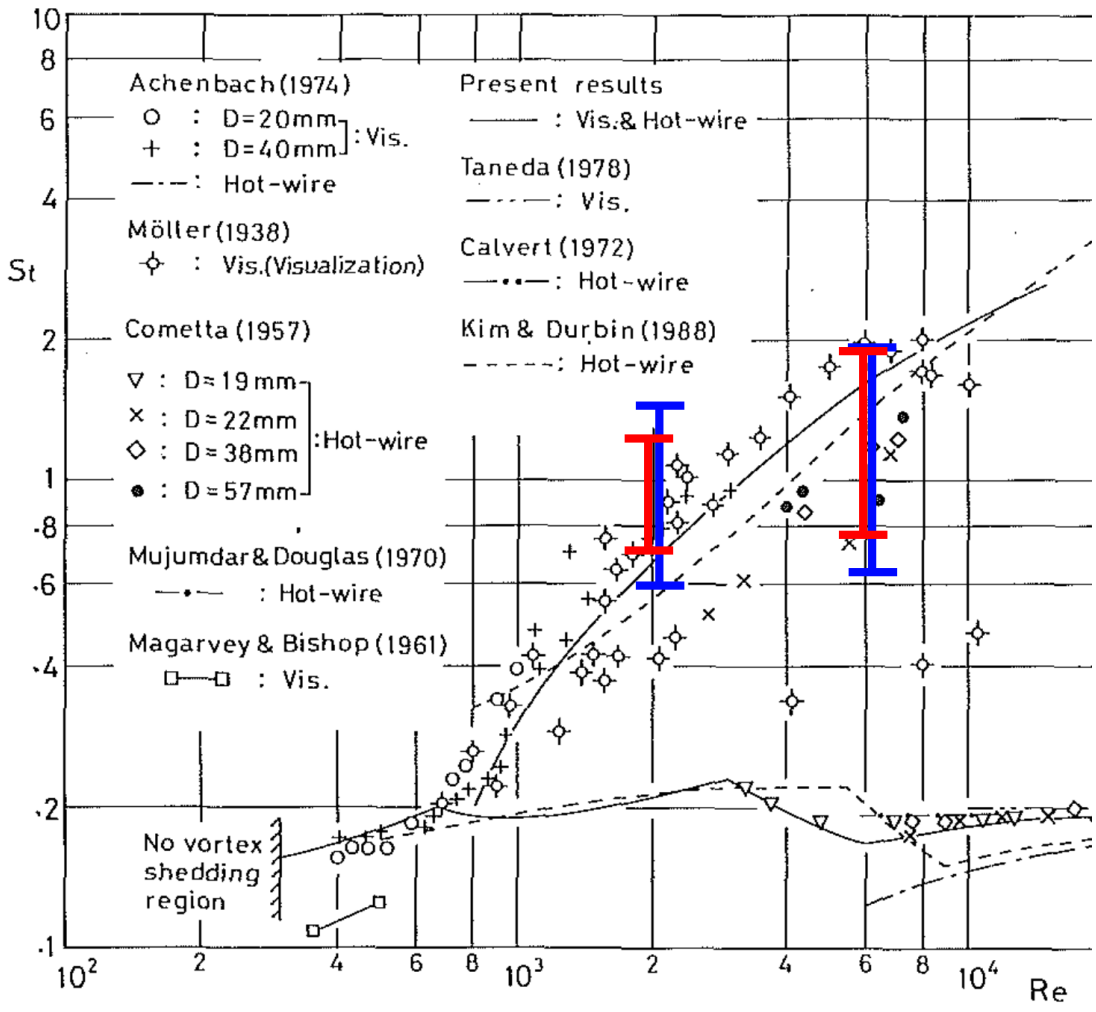

Figure 4.60: Strouhal number (Sakamoto 1990.) Sphere results: Blue, icosahedron results: Red.

Chapter 5

Conclusion

The development of this work has allowed us to answer the questions posed in section 1.2.

The low Reynolds numbers sphere exhibits similarities such as the presence of a strong vortex region behind the sphere, instability of flow lines, irregularity in vortex frequency, and size. The substantial difference is that at $Re = 6000$, regular vortex shedding occurs, whereas it is not present at $Re = 2000$. Additionally, the Allen vortex is only visible at $Re = 6000$; in the other cases, this phenomenon is absent.

The sphere exhibits instabilities proportional to the fluid velocity, both in frequency and intensity. Their nature is chaotic and non-periodic, and no similarities in instability were found among the different tests.

The flow behavior disturbed by an icosahedron tends to generate a strong vortex zone. It is confirmed that flow separation is forced by the edges, which is clearly visible. There are also two zones where the ink stagnates, coinciding with two faces preceded by an edge.

The main differences between the two lie firstly in design; the icosahedron is much simpler to draw, handle, and print, also in terms of time. Then, the icosahedron appears to generate a more chaotic wake, while in the sphere, the vortices can be recognized more easily. Observing flow lines in the case of the icosahedron, it appears to be less instability, but this could also be due to the fact that in the sphere, the flow line covers more space before separating, making it easier to visualize with this visualization technique. The direction of the icosahedron wake is divergent, while it remains constant in the sphere.

They have similar Strouhal number values, in accordance with the literature, and an important vortex region forms just after their shape.

Using fewer tubes, it was possible to optimally visualize the shape and size of the vortices. It would be interesting to conduct a detailed study on the blockage ratio and see if using smaller or larger spheres yields would have similar sphere behaviors. Furthermore, the study the on the toroidal vortex warrants further investigation, as it occurs only at certain Reynolds numbers.

One of the ideas of this work was to integrate a force sensor into the water tunnel to study instability, but it was abandoned due to time constraints. It would be interesting to proceed in this direction and verify the presence of instability. Furthermore, it would be interesting to make improvements to the water tunnel, such as using a longer support between the arm and prototype. Additionally, studying higher Reynolds numbers and, if possible, using a longer tunnel to eliminate the possibility of transitory periods would be beneficial. The last improvement would be to consider designing the arm to occupy a smaller surface area.

Bibliography

[1] R. Manzanares-Bercial, O. Gómez-Ortega, F. Meseguer-Garrido, M. Ogueta-Gutiérrez, and S. Franchini, "Unsteady aerodynamic lateral force on a sphere under a uniform incoming flow," *Journal of Wind Engineering and Industrial Aerodynamics*, vol. 231, p. 105 205, 2022.

[2] O. Gómez-Ortega, M. Landeira, M. Ogueta-Gutiérrez, *et al.*, "Transverse aeroelastic instability of guard cables with beacons excited by a longitudinal wind," *Journal of Fluids and Structures*, vol. 84, pp. 122–139, 2019.

[3] O. Gómez Ortega, "Inestabilidad aeroelástica en catenarias con balizas esféricas," Ph.D. dissertation, Espacio, 2021.

[4] E. Achenbach, "The effects of surface roughness and tunnel blockage on the flow past spheres," *Journal of fluid mechanics*, vol. 65, no. 1, pp. 113–125, 1974.

[5] S. Taneda, "Visualization of separating stokes flows," *Journal of the Physical Society of Japan*, vol. 46, no. 6, pp. 1935–1942, 1979.

[6] Á. A. Rodríguez-Sevillano, M. J. Casati-Calzada, R. Bardera-Mora, *et al.*, "Exploring the effectiveness of visualization techniques for naca symmetric airfoils at extremely low reynolds numbers," *Fluids*, vol. 8, no. 7, p. 207, 2023.

[7] H. Sakamoto and H Haniu, "A study on vortex shedding from spheres in a uniform flow," 1990.

[8] M. Ozgoren, E. Pinar, B. Sahin, and H. Akilli, "Comparison of flow structures in the downstream region of a cylinder and sphere," *International Journal of Heat and Fluid Flow*, vol. 32, no. 6, pp. 1138–1146, 2011.

[9] S. Taneda, "Experimental investigation of the wake behind a sphere at low reynolds numbers," *Journal of the physical society of Japan*, vol. 11, no. 10, pp. 1104–1108, 1956.

[10] Y. I. Jang and S. J. Lee, "Piv analysis of near-wake behind a sphere at a subcritical reynolds number," *Experiments in Fluids*, vol. 44, pp. 905–914, 2008.

[11] W Moller, "Experimentelle untersuchung zur hydromechanick der hugel, phys," *Z*, vol. 35, pp. 57–80, 1938.

[12] S. Taneda, “Visual study of unsteady separated flows around bodies,” *Progress in Aerospace Sciences*, vol. 17, no. 4, pp. 287–348, 1977.